Topics in Low Energy Quantum Scattering Theory

A thesis presented

by

Jay Y. Vaishnav

to

The Department of Physics

in partial fulfillment of the requirements

for the degree of

Doctor of Philosophy

in the subject of

Physics

Harvard University

Cambridge, Massachusetts

September 2006

Thesis advisor

Eric J. Heller

Author

Jay Y. Vaishnav

Topics in Low Energy Quantum Scattering Theory

Abstract

This thesis treats a number of topics in low energy quantum scattering. Recurrent themes include resonance and interference phenomena arising from quantum multiple scattering. In Chapter 2, we discuss the effect of confining a point scatterer in a two dimensional strip waveguide; we show that the system's transport properties can be described by a single renormalized wavefunction. Chapter 3 discusses scattering from gratings of point scatterers, with the objective of examining whether a row of atoms could potentially be used to guide matter waves. In Chapter 4, we develop formalisms to deal with a number of systems in which multiple scattering coexists with periodicity. In Chapter 5, which departs from the multiple scattering methods of the previous chapters, we discuss the role of degeneracy in two simple models of atomic systems.

Citations to Previously Published Work

Portions of this thesis have appeared as

"Hall of Mirrors Scattering from an Impurity in a Quantum Wire," J. Y. Vaishnav, A. Itsara, E. J. Heller. *Physical Review B* **73**, 115331 (2006).

"Matter Wave Scattering and Guiding by Atomic Arrays," J. Y. Vaishnav, J. D. Walls, M. Apratim, E. J. Heller. Submitted for publication; preprint available at `cond-mat/0703171`.

Contents

To my parents

Acknowledgments

I thank Dr. Mike Stopa, Prof. Maxim Olshanii, and Prof. Antonia Ruiz for their generosity with their time and knowledge. This thesis has benefited greatly from my lively discussions with Dr. Jamie Walls, as well as many other members of the Heller Group, past and present. Ms. Judy Morrison and Ms. Sheila Ferguson have provided efficient and caring administrative support, for which I am extremely grateful.

Drs. Areez Mody, Verónica Sanz, and Wesley Wong have helped me over many a bump in the road; I thank each of them, and many others, for their friendship. I am grateful to my parents for the love and patience with which they have always encouraged me to pursue my dreams.

Over the years, I have appreciated Prof. Heller's guidance, and enjoyed his company. Rick is a spirited sailor of ocean waves and quantum ones; I wish him favorable winds, always.

Chapter 1

Introduction and Outline of Thesis

The work in this thesis examines scattering in a number of few-body, low-energy, quantum systems: This thesis is, in essence, an exploration of interference, of resonance, and of waves. Several of the systems I study seem deceptively simple at first glance. Yet, if this thesis has a theme, it is that waves are subtle. Even small quantum systems, when studied in detail, unfold to reveal a rich multitude of complicated interference phenomena that defy intuition: A scatterer in a wire can be transparent; a wall of atoms can guide waves focused on one end.

Our study of scattering phenomena begins in Chapter 2, where I examine the problem of scattering from an impurity confined in a quantum wire. Although this problem is a single scattering problem with boundary conditions, it is also a problem of multiple scattering: Amplitude confined to a waveguide can scatter from an impurity, reflect from the waveguide walls, and scatter again. Once we have accounted for the reflections from the walls, direct analogs of free space partial waves and cross sections, as well as the optical theorem, turn out to exist in a confined geometry. Our principal result in this chapter is to express the transport through the wire in terms of a single wavefunction which contains all the reflection and interference effects.

In Chapter 3, we investigate the scattering of scalar waves from quasi-1D periodic and near-periodic gratings constructed from point scatterers, and embedded in 2D. Such gratings can be built from individual atoms, for example via the same techniques used to build "quantum corrals." Multiple scattering theory has been tremendously successful at modeling the transport properties of

quantum corrals; we apply similar methods here to understand scattering from, as well as conduction by, gratings constructed from point scatterers. We discuss conditions under which arrays of atoms can guide a beam focused at one end of the array, raising the possibility of using a finite grating of atoms as a guide for matter waves.

Chapter 4 applies variants of the solutions in the previous chapters to solve for the scattered wavefunction in a number of other few body systems. In this chapter, we examine the following problems: Scattering of two atoms confined on a tube; scattering in a circular corral; scattering from a confined two-level atom; scattering from double walls; and scattering in a wire, including higher partial waves. This chapter is mostly methodological; we show how each of these systems can be solved by a variant of the renormalized t matrix methods presented in [1], and in each case our final result is an analytic expression for the scattered wavefunction.

Chapters 2, 3, and 4 of this thesis are based on 2D multiple scattering theory. I encourage the reader to begin directly with Chapters 2 and 3, which constitute the bulk of this thesis, and which are entirely self contained. These chapters utilize the concept of a t matrix extensively, and for those who are interested, I have presented in Appendix A an abbreviated discussion of how to use a t matrix to simulate the s wave scattering of any potential, as well as pointers to a number of references.

Chapter 5 departs from the previous time-independent scattering problems: In Chapter 5 we examine the role of degeneracy in two simple quantum mechanical systems. In Section 5.1, we begin by considering resonant energy transfer between two atoms, when one atom is in a trapped state and the other is in an antitrapped state. We frame the problem in terms of adiabatic vs. diabatic dynamics, and examine collisions via time dependent wavepacket methods. In Section 5.2 we look at the presence of degeneracy in a toy model of four atoms interacting on a plane. In a system where the energy depends on N degrees of freedom, it is a general rule that the space of degeneracies has codimension two; for example, a triatomic molecule has two nontrivial degrees of freedom, and the degeneracies occur at a point. In a system with many degrees of freedom, the degeneracies form complicated hypersurfaces. Each time the system makes a circuit of one of these surfaces, it acquires a Berry phase. We use numerical methods to visualize the surfaces of degeneracies, and find that even in this toy model, they have an intricate structure.

Throughout this thesis, unless otherwise noted, we use units $\hbar = m = c = 1$.

Chapter 2

Scattering from Impurities in Quantum Wires

This chapter develops a scattering theory to examine how point impurities affect transport through quantum wires. While some of our new results apply specifically to hard-walled wires, others–for example, an effective optical theorem for two-dimensional waveguides–are more general. We apply the method of images to the hard-walled guide, explicitly showing how scattering from an impurity affects the wire's conductance. We express the effective cross section of a confined scatterer entirely in terms of the empty waveguide's Green's function, suggesting a way in which to use semiclassical methods to understand transport properties of smooth wires. In addition to predicting some new phenomena, our approach provides a simple physical picture for previously observed effects such as conductance dips and confinement induced resonances.

2.1 Introduction

Elastic scattering from a point defect in a hard-walled, multimode quantum waveguide is a problem which has been the subject of experimental [2, 3] and theoretical [4–9] inquiry in both condensed matter and atomic physics. In this chapter, we revisit the problem from an unconventional point of view, reducing it to the scattering of a single effective wavefunction off an array of images. Our approach enables us to easily understand complex transport phenomena which have already been observed (such as conductance dips), as well as predict other new ones.

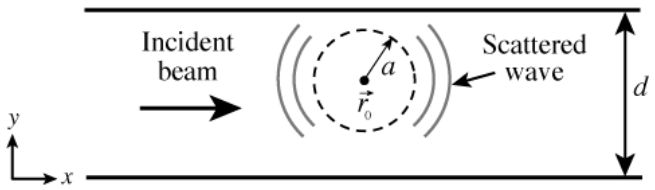

Figure 2.1: Schematic of the quantum wire, with a point impurity of scattering length a at $\vec{r}_0 = (x_0, y_0)$. We assume infinite leads, and hard walls at $y = 0$ and $y = d$.

The problem of scattering from pointlike impurities in waveguides is a general one, and thus has physical applications in several fields. Impurity scattering in quantum wires, and the resulting disorder effects on electron transport, have long been of interest in mesoscopic physics. Specifically, the problem arises in the context of two-dimensional electron gases (2DEGs) confined by quantum wire potentials; the impurity can represent a defect in the wire. Such quantum waveguides can be fabricated at low-temperature $Ga_{1-x}Al_xAs$ interfaces, and are of interest due to their potential role in high-frequency and quantum devices. As carbon nanotubes can behave as few-mode quantum waveguides [10], our results are relevant to transport in nanotubes with adsorbed impurities–of interest in the study of biosensors. The problem of scattering in confined geometries arises in atom waveguides as well, with potential implications for quantum computing and atom interferometry. In both cases, atoms must maintain coherence as they pass through the waveguide, and the goal is thus to minimize phenomena such as collisional phase shifts [11]. Finally, the wave phenomena arising in quantum waveguides are in direct mathematical correspondence with a number of wave phenomena in other systems: Water waves resonantly trapped between an array of cylinders [12], large antenna arrays [13], and sound waves directed by "Bessel" line arrays in acoustics [14].

Motivated by the above applications, we examine low-energy scattering of noninteracting particles from impurities in an infinite two-dimensional quantum wire, with hard walls at $y = 0$ and $y = d$. The wire (Fig. 4.6) contains a point impurity, which we model as an s wave scatterer of effective radius a.

Our method differs from previous treatments, such as the renormalized t matrix method [11, 15, 16], in that we use an unconventional approach which combines the following three ideas:

1. The method of images.

2. The realization that a confined scatterer, like a free space scatterer, is a

rank-one target. We can, therefore, combine the N degenerate transverse modes into a basis in which only a single wavefunction scatters.

3. That the effect of scattering from the waveguide walls is to renormalize this single scattering wavefunction, so that it takes on a new effective value at the scatterer location.

Using the method of images allows us to explicitly understand how each reflection from the waveguide walls affects the conductance. The fact that the confined scatterer is a rank one target enables us to express the transport properties of the wire entirely in terms of the single scattering wavefunction. Finally, the idea of renormalization allows us to fully explain the transport properties of the wire in terms of reflections of this single wavefunction from the waveguide walls.

In Section 2.2, we review free space multiple scattering, anticipating phenomena which will appear in the wire. Section 2.3 lays out a similar formalism for scattering in the waveguide. In Section 2.4, we present physical phenomena which we observed in our model, which we interpret in Section 2.5 in terms of interference effects. We relegate mathematical details to Appendices B-C.

2.2 Preliminaries: Review of Free Space Scattering

In Section 2.3, we show that the Lippmann-Schwinger equation for scattering from a confined impurity resembles the free space Lippmann-Schwinger equation, with the exception that in the wire, a renormalized incoming wavefunction replaces the true one. Surprisingly, even for a single confined scatterer, this renormalized wavefunction includes free space *multiple* scattering effects. We thus begin by briefly reviewing free space scattering, emphasizing the three phenomena which will reappear in the Lippmann-Schwinger equation for a single scatterer in the waveguide.

Consider N pointlike impurities in two-dimensional free space, located at $\{\vec{r}_1, \ldots, \vec{r}_N\}$. Let $V(|\vec{r} - \vec{r}_i|)$ be the potential at $\vec{r}$ due to the i^{th} scatterer. We seek scattering solutions $\psi(\vec{r})$ to the time-independent Schrodinger equation

$$\left[-\frac{\hbar^2}{2m} \vec{\nabla}^2 + \sum_{i=1}^{N} V(|\vec{r} - \vec{r}_i|) - E \right] \psi(\vec{r}) = 0, \tag{2.1}$$

under the assumption of low-energy, s-wave scattering. Except as noted, we

henceforth use atomic units, where $\hbar = m = c = 1$. Applying the t matrix formalism, [17] we characterize a single scatterer at $\vec{r}_i$ by its t matrix,

$$t = s(k)\,|\vec{r}_i\rangle\langle\vec{r}_i| \tag{2.2}$$

where $s(k)$ is a function of the wavenumber, $k = \sqrt{2mE}/\hbar$. We choose the functional form of $s(k)$ to simulate the scatterer of interest, under the constraint that $s(k)$ must satisfy the optical theorem

$$\text{-2Im}s(k) = |s(k)|^2\,. \tag{2.3}$$

In this chapter, we choose

$$s(k) = -2i\frac{\hbar^2}{m}\frac{J_0(ka)}{H_0^{(1)}(ka)}, \tag{2.4}$$

which represents a hard disk of scattering length a.

2.2.1 Single Scatterer

Consider a single scatterer at $\vec{r} = \vec{r}_0$. In our t matrix representation, an incident wave $\phi(\vec{r})$ scatters into a wavefunction $\psi(\vec{r})$ according to the Lippmann-Schwinger equation

$$\psi(\vec{r}) = \phi(\vec{r}) + s(k)\phi(\vec{r}_0)G_0(\vec{r},\vec{r}_0;k) \tag{2.5}$$

where

$$G_0(\vec{r},\vec{r}_0;k) = \frac{2m}{\hbar^2}\left[-\frac{i}{4}H_0^{(1)}(k|\vec{r}-\vec{r}_0|)\right] \tag{2.6}$$

is the 2D free space advanced Green's function satisfying

$$\left(\vec{\nabla}^2 + k^2\right)G_0(\vec{r},\vec{r}_0;k) = \frac{2m}{\hbar^2}\delta^{(2)}(\vec{r}-\vec{r}_0). \tag{2.7}$$

We shall henceforth assume we are using the advanced Green's function and omit the superscript on the Hankel function; we shall also omit the implicit k dependence in the Green's function.

2.2.1.1 Single Scattering Wavefunction

Any incoming wave $\phi(\vec{r})$ must be a solution to the free space Schrodinger equation. We can therefore express $\phi(\vec{r})$ in the basis of "cylinder harmonics,"

$$\phi(\vec{r}) = \sum_{m=0}^{\infty} c_m J_m(k|\vec{r} - \vec{r}_0|) \times \frac{e^{im(\phi-\phi_0)}}{\sqrt{2\pi}} \tag{2.8}$$

where $m = 0, 1, 2, \ldots$ correspond to s,p,d,$\ldots$ waves. An s wave scatterer in free space is a rank one perturbation: Of all the terms in (2.8), only the $m = 0$ term is nonzero at the scatterer. From (2.5), then, only the s wave scatters, acquiring a phase shift; remaining higher partial waves pass through the scatterer unperturbed. While trivial in free space, these facts will reappear more subtly in the wire.

2.2.2 Multiple Scatterers

The Lippmann-Schwinger equation describing scattering from a collection of N identical point scatterers at $\{\vec{r}_1, \ldots, \vec{r}_N\}$ is

$$\psi(\vec{r}) = \phi(\vec{r}) + s(k) \sum_{i=1}^{N} \psi_i(\vec{r}_i) G_0(\vec{r}, \vec{r}_i) \tag{2.9}$$

in which we express the $\psi_i(\vec{r}_i)$ recursively as

$$\psi_i(\vec{r}_i) = \phi(\vec{r}_i) + s(k) \sum_{\substack{j=1 \\ j \neq i}}^{N} \psi_j(\vec{r}_j) G_0(\vec{r}_i, \vec{r}_j). \tag{2.10}$$

where we have followed Foldy's method. [18] Comparing (3.2-2.10) with the single-scatterer version (2.5), the $\psi_i(\vec{r}_i)$ are the $effective$ incoming wavefunctions at each scatterer: $\psi_i(\vec{r}_i)$ is the amplitude incident on the i^{th} scatterer after scattering from each of the other scatterers. A crucial point is that $\psi_i(\vec{r}_i)$ excludes the singular self-interaction of the i^{th} scatterer.

Defining $\vec{\phi}_i \equiv \phi(\vec{r}_i)$, $\vec{\psi}_i \equiv \psi(\vec{r}_i)$, inverting (3.2-2.10) yields

$$\vec{\psi} = (\mathbf{1} - s\mathbf{G})^{-1} \vec{\phi} \tag{2.11}$$

where

$$G_{ij} \equiv \begin{cases} G_0(\vec{r}_i, \vec{r}_j) & i \neq j \\ 0 & i = j \end{cases} \tag{2.12}$$

excludes the singular term. An alternate expression of (2.11) is as the Born series

$$\vec{\psi} = \left[\mathbf{1} + s\mathbf{G} + (s\mathbf{G})^2 + (s\mathbf{G})^3 + \dots\right] \vec{\phi}. \tag{2.13}$$

The effective wavefunctions thus have a simple interpretation in terms of interfering paths: The terms in square brackets describe amplitude incident at $\vec{r}_i$ after interactions with zero, one, two, or three other scatterers respectively. The series continues infinitely.

Anticipating phenomena that will reappear in the wire, we highlight the following points of this section:

1. The effect of multiple scattering is to create a new effective incoming wavefunction at each scatterer.

2. The effective wavefunction at a particular scatterer is a sum of waves scattered from all the *other* scatterers, and excludes the (singular) self-interaction of the scatterer.

3. An s wave scatterer in free space is a rank one target.

2.3 Scatterer in a Wire

In this section, we examine how confinement in a wire affects the transport properties of a scatterer. Applying the method of images, we derive a form of the empty wire Green's function. Using this form of the Green's function, we show that the sole effect of confinement is to renormalize the incoming wavefunction. The image representation allows us to very simply calculate the renormalization coefficient. We define an effective cross section for a confined scatterer, and relate it to the conductance of the wire-impurity system. We derive an effective optical theorem in the wire. Finally, applying this formalism, we investigate the behavior of the cross section and conductance as functions of various parameters.

2.3.1 Green's Function via the Method of Images

In order to write down the Lippmann-Schwinger equation for an impurity in the wire, we require the Green's function $G_w(\vec{r}, \vec{r}_0)$ of the empty wire. The usual spectral form of the empty wire Green's function is

$$G_w(\vec{r}, \vec{r}_0) = -i \sum_{m=1}^{\infty} \frac{1}{k_x^{(m)}} \chi_m(y) \chi_m(y_0) e^{ik_x^{(m)}|x - x_0|} \tag{2.14}$$

where the $\chi_m(y)$ are the transverse modes for the particular waveguide (see e.g. Datta [19]). In our hard wire, the modes have the form

$$\chi_m(y) = \begin{cases} \sqrt{\frac{2}{d}} \sin\left(\frac{m\pi y}{d}\right) & 0 < y < d \\ 0 & y < 0,\ y > d. \end{cases} \tag{2.15}$$

We note that the spectral Green's function (2.14) is a sum over evanescent modes as well as propagating ones.

Although we could, in principle, proceed using the spectral form (2.14) of the Green's function, the spectral Green's function provides little physical insight into the precise mechanism of the scattering. We therefore take an alternative approach, and use the method of images to derive an alternate, equivalent form of (2.14) for the hard wire.

Although the problem of an impurity in a hard wire has been the subject of numerous theoretical studies, [4–9] the authors are aware of only one work [20] which applies the method of images: [20] treats the related problem of a point scatterer in a 3D waveguide of rectangular cross section, which the authors reduce to the problem of scattering from an impurity in a finite, 2D box. The method of images has the significant advantage of making multiple scattering effects explicit. We shall thus use the approach of [20], rather than the more common spectral methods. Because our problem of an infinite waveguide is somewhat simpler than the finite box treated in [20], the role of multiple scattering is more transparent. We are therefore able to explore in detail the considerable effect of multiple scattering on the physical properties of the wire, which, although briefly mentioned, is not examined in [20].

The empty wire Green's function $G_w(\vec{r}, \vec{r}_0)$ satisfies Green's equation inside the wire, and is zero on the wire walls:

$$(\vec{\nabla}^2 + k^2) G_w(\vec{r}, \vec{r}_0) = 2\delta(\vec{r} - \vec{r}_0) \tag{2.16}$$

$$G_w(x, 0) = G_w(x, d) = 0 \tag{2.17}$$

The confined Green's function differs from the free space version due to the necessity of including reflections off the walls when describing the response to a point excitation. Note the factor of two in (2.16), obtained by casting (2.7) in atomic units.

As in electrostatics, we can linearly combine free space Green's functions (2.6) with point sources in different places, so that the linear combination satis-

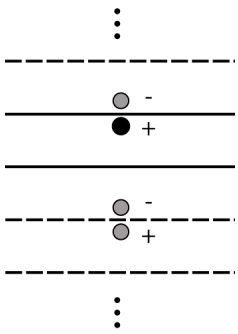

Figure 2.2: The method of images allows us to reduce the problem of a single scatterer in a wire to that of a periodic array of scatterers in free space. The solid lines and black scatterer are the actual wire and point source. The gray point sources, and the dashed lines, are images. The pluses and minuses refer to the sign of the free-space Green's function term that the particular point source contributes. The alternating signs of these contributions are due to the Dirichlet boundary conditions; the wavefunction must cancel on the wire walls.

fies (2.17). As long as only one of the point sources is inside the wire ($0 < y < d$), our sum will satisfy (2.16) inside the wire. Outside the wire, we discard the solution. If the point source is located at $\vec{r} = (x_0, y_0)$, we use the configuration of image point sources in Fig. 2.2. We reflect the scatterer, creating a series of images such that the position of the n^{th} image is $\vec{r}_n = x_0\hat{x} + [(-1)^n y_0 + 2nd]\hat{y}$.

This image configuration yields an empty wire Green's function of the form

$$G_w(\vec{r}, \vec{r}_0) = \sum_{n=-\infty}^{\infty} (-1)^n G_0(\vec{r},\vec{r}_n) \tag{2.18}$$

The Green's function (2.18) satisfies (2.16) inside the wire, and (2.17) on the wire boundaries. Outside the wire we implicitly set the Green's function to zero. The Green's function satisfies the Dirichlet boundary conditions because, as we take infinitely many images, the alternating sum of Hankel functions converges to zero on the walls. This series converges extremely slowly, precluding its use for numerical purposes (see the discussion in [21]).

2.3.2 Renormalizing the Incoming Wavefunction

The Lippmann-Schwinger equation requires knowledge of both the Green's function and the incoming wavefunction. In Section 2.2.1, we calculated the Green's function for the wire. In this section, we discuss the incident wavefunction.

We show that the effects of confinement resemble free space multiple scattering: Confinement renormalizes the effective wavefunction at the scatterer from its true value. In the image formalism, the multiple scattering arises due to scattering off images.

Applying the free space multiple scattering formalism (3.2,2.10) to the array of images in Fig. 2.2, we find that the Lippmann-Schwinger equation for the wire is

$$\psi(\vec{r}) \quad = \quad \phi(\vec{r}) + s \sum_{i=-\infty}^{\infty} G_0(\vec{r}, \vec{r}_i)\psi_i(\vec{r}_i) \tag{2.19}$$

where

$$\psi_i(\vec{r}_i) = \phi(\vec{r}_i) + s \sum_{\substack{j=-\infty \\ j\neq i}}^{\infty} G_0(\vec{r}_i, \vec{r}_j)\psi_j(\vec{r}_j). \tag{2.20}$$

Recall from our discussion of free space multiple scattering the physical meaning of this recursive Lippmann-Schwinger equation: The $\psi_i(\vec{r}_i)$ defined in (2.20) are the effective incoming wavefunctions at the i^{th} scatterer in the array. In a general multiple scattering problem, we would have to stop here and solve numerically. The image array is, however, a special case: Not only is it periodic, but the boundary conditions at the wall impose the antisymmetry

$$\begin{aligned} \phi(\vec{r}_i) &= (-1)^i \phi(\vec{r}_0) \\ \psi_i(\vec{r}_i) &= (-1)^i \psi_0(\vec{r}_0). \end{aligned} \tag{2.21}$$

Any wavefunction, incident or scatterered, must be zero on the walls. Thus, inside the wire, in the y direction, the wavefunction is a superposition of modes (2.15). Replacing the wire with an image array requires that we extend these modes outside the wire, into the region $y < 0, y > d$. Keeping the $\chi_m(y)$ continuous at the walls, we can extend them so that the wavefunction is either symmetric or antisymmetric across the wire walls; either set forms a basis. However, we know that in the absence of a wall $\chi'_m(y)$ must be continuous also, as we have eliminated the hard walls. The symmetric extension does not satisfy this condition. We therefore discard the symmetric extension, leaving (2.21) as the proper boundary condition.

Combining (2.20) and (2.21), the equation for the wavelets thus becomes

$$\psi_i(\vec{r}_i) \quad = \quad (-1)^i \left[\phi(\vec{r}_0) + s\psi_0(\vec{r}_0)G_r\right] \tag{2.22}$$

where we have defined the renormalization sum

$$G_r \equiv \sum_{\substack{i=-\infty \\ i\neq 0}}^{\infty} (-1)^i G_0(\vec{r_i}, \vec{r}_0) \tag{2.23}$$

noting that

$$G_r = (-1)^j \sum_{\substack{i=-\infty \\ i\neq j}}^{\infty} (-1)^i G_0(\vec{r_i}, \vec{r}_j). \tag{2.24}$$

Taking $i = 0$ in (2.22), we find

$$\psi_0(\vec{r}_0) = \frac{\phi(\vec{r}_0)}{1 - sG_r} \tag{2.25}$$

Substituting (2.21,2.25) into (2.19) yields the Lippmann-Schwinger equation for scattering from an impurity in a wire:

$$\psi(\vec{r}) = \phi(\vec{r}) + s\left[\frac{\phi(\vec{r}_0)}{1 - sG_r}\right] \sum_{i=-\infty}^{\infty} (-1)^i G_0(\vec{r}, \vec{r}_i) \tag{2.26}$$

$$= \phi(\vec{r}) + s\left[\frac{\phi(\vec{r}_0)}{1 - sG_r}\right] G_w(\vec{r}, \vec{r}_0). \tag{2.27}$$

Comparing (2.27) to the free space Lippmann-Schwinger equation (2.5) for a single scatterer, we see that the wire simply renormalizes the incoming wavefunction at the scatterer to have a new effective value

$$\tilde{\phi}(\vec{r}_0) = \frac{\phi(\vec{r}_0)}{1 - sG_r} \tag{2.28}$$

and so our final Lippmann-Schwinger equation is

$$\psi(\vec{r}) = \phi(\vec{r}) + s\tilde{\phi}(\vec{r}_0) G_w(\vec{r}, \vec{r}_0). \tag{2.29}$$

For convenience, we define a renormalization factor

$$\mathcal{R} \equiv \frac{\phi(\vec{r}_0)}{\tilde{\phi}(\vec{r}_0)} \tag{2.30}$$

which is the ratio between the original and renormalized incoming wavefunctions at the scatterer.

In order to cast the renormalized incoming wavefunction in terms of interfering paths, we expand perturbatively, as we did in (2.13) for free space. For

shorthand, define

$$G_{i\to j} \equiv (-1)^{i+j} G(\vec{r}_i, \vec{r}_j). \tag{2.31}$$

We find

$$\begin{aligned}
\tilde{\phi}(\vec{r}_0) &= (1 + sG_r + s^2 G_r^2 + \dots)\phi(\vec{r}_0) \\
&= \left[1 + \sum_{\substack{i=-\infty \\ i\neq 0}}^{\infty} sG_{i\to 0} \right. \\
&\quad \left. + \sum_{\substack{i=-\infty \\ i\neq 0}}^{\infty} \sum_{\substack{j=-\infty \\ j\neq 0}}^{\infty} sG_{i\to 0} \times sG_{j\to 0} + \dots \right] \phi(\vec{r}_0) \\
&= \left[1 + \sum_{\substack{i=-\infty \\ i\neq 0}}^{\infty} sG_{i\to 0} \right. \\
&\quad \left. + \sum_{\substack{i=-\infty \\ i\neq j}}^{\infty} \sum_{\substack{j=-\infty \\ j\neq 0}}^{\infty} sG_{i\to j} \times sG_{j\to 0} \right] \phi(\vec{r}_0)
\end{aligned} \tag{2.32}$$

where we have used (2.24). The n^{th} term of the sum (2.32) describes propagation to $\vec{r}_0$ after scattering from any $n-1$ images, beginning with the first term, which describes free propagation to $\vec{r}_0$. Alternately, the n^{th} term corresponds to n scattering events combined with any number of reflections off the wall, each of which introduces an additional phase of -1. Fig. 2.3 illustrates the correspondence between scattering from an image and reflecting from the wall.

Renormalization of the effective wavefunction is simply the manifestation of the identical phenomenon in free space (see item 1 in the list of Section 2.2.2). From a semiclassical point of view, the incoming wave, given infinite time to spread, reflects from each possible combination of scatterers before returning to the source. Note that G_r is simply the wire's Green's function evaluated at the scatterer, with the singular self-interaction of the source removed,

$$G_r = \lim_{\vec{r}\to\vec{r}_0} \left[G_w(\vec{r}, \vec{r}_0) - G_0(\vec{r}, \vec{r}_0) \right]. \tag{2.33}$$

This idea, as expressed in (2.33), is the essence of "renormalized t matrix theory"

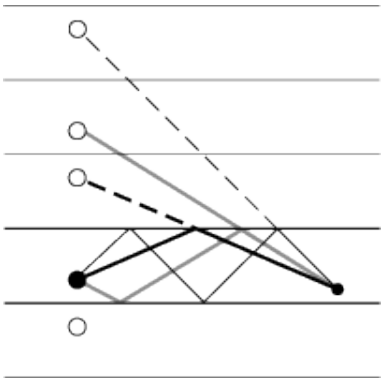

Figure 2.3: Amplitude scattering from the n^{th} image corresponds to amplitude reaching a point after n bounces from the wall, each of which reverses the sign of the wavefunction (phrased semiclassically, reflections introduce a Maslov index of -1). Resonances occur when the interference of all paths is maximally constructive at the scatterer itself.

[1, 11, 16]. The theory, as applied to our case, is equivalent to the idea that in free space multiple scattering, the effective wavefunction at a scatterer excludes the singular self-interaction (see item 2 of Section 2.2.2). We note that although we have derived (2.33) via images only for the special case of a hard walled guide, the result (usually derived perturbatively) is in fact true for an arbitrary guide or confining potential [1].

2.3.3 Method of Images vs. Spectral Formulation

We have presented both the image series (2.18) and the spectral series (2.14) for the Green's function. Because the Green's function of a system is unique, these two forms must be equivalent. However, the physical relationship between the method of images and the spectral form is far from obvious. The two forms of the Green's function highlight different physical phenomena. For example, reflections from the walls, which appear immediately in (2.18), are far less obvious in the spectral form (2.14). Contrastingly, the role of evanescent channels in the scattering, while straightforward in the spectral Green's function (2.14), is less transparent in the image expansion (2.18) of the same Green's function (although even the image expansion suggests that evanescent channels will be present in some form, because Hankel functions are singular). In order to understand the connection between the image and spectral forms of the Green's function, we show their equivalence mathematically in Appendix B.

In Appendix A, we use an integral form of the Hankel function to show the

equivalence of (2.18) and (2.14). The physical connection between the image and spectral formalisms is diffraction. The images in Fig. 2.2 form a periodic array, which is effectively a diffraction grating. We note one small difference from a typical diffraction situation: Due to the wire boundary conditions, the incident modes are superpositions of two plane waves each, rather than a single incident plane wave. This difference is trivial, due to the linearity of Schrodinger's equation. When such modes are incident on the effective lattice of images, they diffract: Plane waves (or superpositions of plane waves) striking the grating scatter, at large distances, into sums of plane waves at the Bragg angles. The diffracted spectral orders are evident as the quantized wavenumbers appearing in the spectral form of the Green's function. As the Green's function for each image scatterer is singular, evanescent waves appear in the Fresnel regime, near the lattice. We examine these statements rigorously in Appendix B.

Numerics

While the method of images led quickly to the central results (2.27,2.33), these results expressed in terms of image sums converge so slowly as to be impractical for numerics. Although the spectral form (2.14) converges more rapidly than the image series (2.18), its convergence is still not uniform, as the evanescent modes include a logarithmic singularity.

In Appendix C, we use Kummer's method to accelerate the convergence of the Green's function, casting it in the form (C.0.2) suitable for numerical work. A side benefit of applying Kummer's method is that we obtain a more rapidly converging expression for G_r: In Appendix C, we show that the series (2.23) for G_r (which is a Schlömilch series) resums to

$$\begin{aligned} G_r &= \sum_{m=1}^{\infty} \left(\frac{1}{ik_x^{(m)}} + \frac{d}{m\pi} \right) \chi_m^2(y_0) \\ &\quad -\frac{1}{\pi} \ln \left[\frac{kd}{\pi} \sin\left(\frac{\pi y_0}{d} \right) \right] + \frac{i}{2} - \frac{\gamma}{\pi} \end{aligned} \tag{2.34}$$

where γ is the Euler-Mascheroni constant. We note that this expression is considerably more complex than the expression (2.23) derived via the method of images. In the image formalism, the expression for the renormalization constant G_r has the intuitive form (2.23), because removing the contribution of the source simply involves excluding the scatterer itself, while retaining the images. In the spectral formalism, because the singularity is not explicit, its removal is considerably less transparent.

2.3.4 Scattering Phenomena in Quantum Wires

In this subsection we define an effective cross section and optical theorem for the confined impurity. As we have shifted from the image formalism (which applies only to the hard wire) to the spectral one, where (2.14) applies generally, the results presented in Section 2.3.4 apply to arbitrary waveguides, not only hard wires.

2.3.4.1 The S Matrix

Since the wire is infinite, for calculating transmission/reflection at infinity, we need consider only the open channels. Without loss of generality (due to translational invariance of the wire in the x direction), suppose the scatterer is at $x_0 = 0$. With incident mode n, normalized to unit flux, the wavefunction at large distances from the scatterer is

$$\begin{aligned}\psi(x,y;0,y_0) &= \frac{e^{\pm ik_x^{(n)}x}}{\sqrt{k_x^{(n)}}}\chi_n(y) - \sum_{m=1}^{\infty}\left[\frac{i\mathcal{R}s}{\sqrt{k_x^{(n)}k_x^{(m)}}}\right. \\ &\quad \left.\times\chi_n(y_0)\chi_m(y_0)\frac{e^{ik_x^{(m)}|x|}}{\sqrt{k_x^{(m)}}}\chi_m(y)\right] \end{aligned} \tag{2.35}$$

from which we can read off a scattering matrix

$$\mathbf{S} = \begin{pmatrix} \mathbf{R} & \mathbf{T}' \\ \mathbf{T} & \mathbf{R}' \end{pmatrix} = \begin{pmatrix} \mathbf{R} & \mathbf{I}-\mathbf{R} \\ \mathbf{I}-\mathbf{R} & \mathbf{R} \end{pmatrix} \tag{2.36}$$

where the reflection and transmission coefficients are

$$R_{mn} = R'_{mn} = -\frac{i\mathcal{R}s}{\sqrt{k_x^{(n)}k_x^{(m)}}}\chi_n(y_0)\chi_m(y_0) \tag{2.37}$$

$$T_{mn} = T'_{mn} = \delta_{mn} + R_{mn} \tag{2.38}$$

One can show algebraically (or verify numerically) that

$$\operatorname{rank}\mathbf{R} = \operatorname{rank}(\mathbf{T}-\mathbf{I}) = 1.$$

2.3.4.2 Defining a Cross Section in the Wire

In this section, we define an effective scattering cross section for the wire. The usual three-dimensional free space differential scattering cross section is

$$\frac{d\sigma}{d\Omega} = \frac{dN(\Omega)}{N_{in} d\Omega} \tag{2.39}$$

where $dN(\Omega)$ is the number of particles per area scattered into the solid angle $d\Omega$, and N_{in} is the number of incident particles per unit area. Expressed in terms of probability currents, the above relation becomes

$$\frac{d\sigma}{d\Omega} = \frac{\int j_r r^2 d\Omega}{j_{in}} \tag{2.40}$$

where $\vec{j} = \mathrm{Im}(\Psi^* \nabla \Psi)$ is the probability current, j_{in} is the incoming probability current, and j_r is the radial probability current. Integrating over solid angles, we find that

$$\sigma = \int \frac{\int j_r r^2 d\Omega}{j_{in}} d\Omega \tag{2.41}$$

The optical theorem in free space relates the forward scattering amplitude to the cross section.

Here, we modify the above free space relations, in order to define a cross section for our confined geometry. With incident mode $\phi_n(x, y)$, the scattering wavefunction is

$$\begin{aligned} \psi_n(x,y) - \phi_n(x,y) &= -\frac{i}{\sqrt{k_x^{(n)}}} \sum_m \frac{\mathcal{R}s}{\sqrt{k_x^{(m)}}} \chi_n(y_0)\chi_m(y_0) \\ &\quad \times \frac{e^{ik_x^{(m)}|x|}}{\sqrt{k_x^{(m)}}} \chi_m(y) \end{aligned} \tag{2.42}$$

which yields a probability current in the x direction

$$\begin{aligned} j_x &= \frac{|\chi_n(y')|^2}{k_x^{(n)}} \sum_{m,p} |\mathcal{R}s|^2 \frac{1}{\sqrt{k_x^{(n)} k_x^{(p)}}} \chi_m(y_0)\chi_p(y_0) \\ &\quad \times e^{i(k_x^{(m)} - k_x^{(p)})|x|} \chi_m(y)\chi_p(y). \end{aligned} \tag{2.43}$$

Integrated over y, the cross terms cancel, and this current yields a scattered flux

$$\int_0^d j_x dy = \frac{\chi_n^2(y_0)}{k_x^{(n)}} \sum_m |\mathcal{R}s|^2 \frac{\chi_m^2(y_0)}{k_x^{(m)}} \tag{2.44}$$

going in each direction. As our basis is normalized to unit flux, in our case, the incident flux is simply 1. We define a differential cross section for the n^{th} incoming mode, similar to the free space differential cross section (2.41):

$$\begin{aligned} \sigma_n &= \int dy \frac{d\sigma_n}{dy} && (2.45) \\ &= \int dy \frac{\int j_x dy}{j_{in}} && (2.46) \\ &= |\mathcal{R}s|^2 d \frac{\chi_n^2(y_0)}{k_x^{(n)}} \sum_m \frac{\chi_m^2(y_0)}{k_x^{(m)}} && (2.47) \end{aligned}$$

where we note the exact analogy between plane waves in our waveguide and partial waves in free space. Note also that σ_n has the correct dimensions of length.

In free space, the cross section of a spherically symmetric scatterer is independent of the direction of the incident plane wave. In the waveguide, however, the cross section depends on the incoming mode, because the waveguide breaks spherical symmetry. We can define a total cross section as the average over incoming directions,

$$\bar{\sigma} = \frac{1}{2N} \sum_{n=-N}^{N} \sigma_n \qquad (2.48)$$

We note that $\bar{\sigma}$ represents a sort of fraction of the incoming wavefunctions which scatter. Flux conservation imposes the bound

$$0 \leq \sum_{n=-N}^{N} \sigma_n \leq d. \qquad (2.49)$$

The maximal value of $\bar{\sigma}$ will, therefore, be $1/2N$, and its minimal value will be 0.

We had previously mentioned that $\text{rank}(\mathbf{T} - \mathbf{I}) = \text{rank}\,\mathbf{R} = 1$. This reduced rank indicates that, as in free space, a basis exists in which a single wavefunction scatters, while the remaining $2N-1$ do not. The quantity $2N\bar{\sigma}$ thus tells us the fraction of the flux of this scattering wavefunction, and should be between 0 and 1. Henceforth we will speak of $\sigma \equiv 2N\bar{\sigma}/d$ as the cross section (as a fraction of

the wire width). Our final cross section is thus

$$\sigma = |\mathcal{R}s|^2 \left(\sum_{n=-N}^{N} \frac{\chi_n^2(y_0)}{k_x^{(n)}} \right)^2 \tag{2.50}$$

and satisfies

$$0 < \sigma < 1. \tag{2.51}$$

We note that for m impurities in the wire, assuming there are $N > m$ modes available, $\text{rank}(\mathbf{T} - \mathbf{I}) = \text{rank}\,\mathbf{R} = m$. By arguments analogous to the single scatterer case, with m scatterers present, we could choose a basis where only m wavefunctions would scatter, while the remaining $N - m$ would be transmitted without any perturbation.

2.3.4.3 Modified Optical Theorem in the Waveguide

The usual free space optical theorem involves the imaginary part of the forward scattering amplitude. One can show that the free space optical theorem constrains s via

$$(\text{Im}s)^2 = -\frac{1}{2}|s|^2. \tag{2.52}$$

A similar relation holds in the wire, and as it turns out, flux conservation implies that not every value of $\mathcal{R}s$ is physically permissible. Unitarity of $\mathbf{S}$ implies that

$$\sum_m |R_{mn}|^2 + |T_{mn}|^2 = 1. \tag{2.53}$$

Using (2.37-2.38) in (2.53), after some algebra, we find

$$\textstyle\sum_m |R_{mn}|^2 + \delta_{mn}(1 + 2\ \text{Re}\ R_{mn}) = 1, \quad \text{any } n \tag{2.54}$$

which requires that $\mathcal{R}s$ satisfy the constraint

$$|\mathcal{R}s|^2 \sum_m \frac{\chi_m^2(y_0)}{k_x^{(m)}} = -\text{Im}(\mathcal{R}s). \tag{2.55}$$

We can express (2.55) as an optical theorem, like the one in free space. Define the "forward scattering amplitude" to be the amplitude which scatters in the direction of the incoming wave:

$$f_n \equiv -\frac{i\mathcal{R}s}{k_x^{(n)}}\chi_n(y_0). \tag{2.56}$$

With this definition, our "optical theorem" in the wire becomes

$$\mathrm{Im}(e^{-i\pi/2} f_n) = \chi_n(y_0)\sigma_n \tag{2.57}$$

which is very similar to the 2-D free space optical theorem,

$$\mathrm{Im}\left(f(0)e^{-i\pi/4}\right) = \sqrt{\frac{k}{8\pi}}\sigma \tag{2.58}$$

where $f(0)$ is the forward scattering amplitude. Combining (2.50) and (2.55) allows us to define a cross section,

$$\begin{aligned} \sigma(k,a) &= -\sum_n \frac{\chi_n(y_0)^2}{k_x^{(n)}}\mathrm{Im}(\mathcal{R}s) && (2.59)\\ &= \frac{\mathrm{Im}(\mathcal{R}s)^2}{|\mathcal{R}s|^2}. && (2.60) \end{aligned}$$

2.3.4.4 Relationship between Cross Section and Conductance

We note that our cross section is trivially related to the conductance of the wire, calculated as in the Landauer formalism [22] as $G = \frac{2e^2}{\hbar}\mathrm{Tr}\ \mathbf{T}^\dagger\mathbf{T}$. Noting that $\mathbf{T} = \mathbf{I}\text{-}\mathbf{R}$, and letting N equal the number of open channels,

$$\begin{aligned} G &\propto \mathrm{Tr}\ \mathbf{T}^\dagger\mathbf{T}.\\ &= N + 2\mathrm{Re}\ \mathrm{Tr}\,\mathbf{R} + \sum_m\sum_p |R_{mp}|^2 && (2.61)\\ &= N + 2\mathrm{Im}\,(\mathcal{R}s)\sum_p \frac{\chi_p^2(y_0)}{k_x^{(p)}} && (2.62)\\ &\qquad + \sum_p \frac{1}{k_x^{(p)}}\chi_p^2(y_0)\sum_m \frac{|\tilde{s}|^2}{k_x^{(p)}}\chi_m^2(y_0)\\ &= N - 2\sigma - \mathrm{Im}\,(\mathcal{R}s)\sum_p \frac{\chi_p^2(y_0)}{k_x^{(p)}} && (2.63)\\ &= N - \sigma && (2.64) \end{aligned}$$

where we have used (2.37), (2.55), and (2.59).

In this section, we have laid out the formalism which we shall use to examine scattering in the wire. In Section 2.4, we use our formalism to examine how the cross section and conductance of the confined scatterer vary as the physical parameters of the wire change.

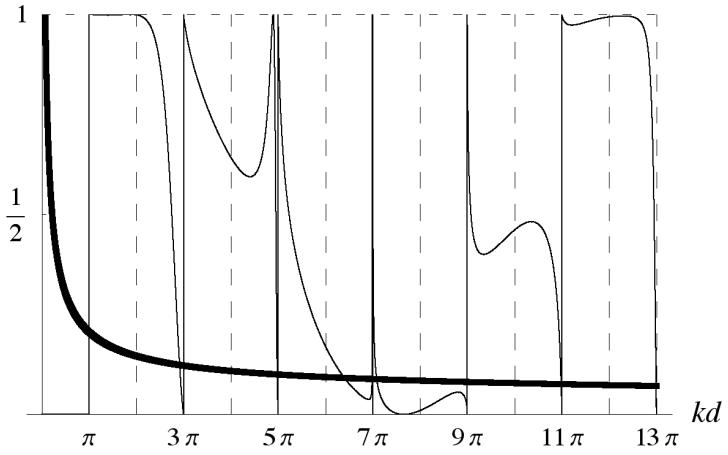

Figure 2.4: Free space cross section (thick line) and cross section for confined scatterer (thin line), vs. kd. The scatterer is in the center of the wire, at $y_0 = 0.5d$. Its scattering length is $a = 0.1d$.

2.4 Results and Discussion: Confinement Induced Scattering Phenomena

Confinement induced effects on transport, in particular "conductance dips" as each new mode opens, have been observed experimentally [2] as well as in other theoretical investigations [4, 6, 7, 20] of impurity scattering in quantum wires. Changes in the transport due to motion of a single defect are studied in relation to universal conductance fluctuations. [3] Theoretically, the observed phenomena are generally explained via mode-mixing effects, [6] or loosely attributed to multiple scattering from the walls. [20] In this section, we discuss some confinement induced phenomena as we specifically observe them in our wire.

The first quantity we wish to examine is how the cross section of the confined scatterer relates to the free space cross section of the identical scatterer, as a function of energy. The cross section of a free space scatterer is

$$\sigma_f = \frac{1}{k} |s|^2 . \tag{2.65}$$

Fig. 2.4 shows that one feature resulting purely from confinement is the appearance of sharp discontinuities in the cross section as new modes become available; the effect is present only if the newly opened mode is nonzero at the scatterer. To the left of each mode opening, the scatterer appears entirely

transparent, whereas to the right of the mode opening its cross section is the full width of the wire. Another point to note is that, while the free space cross section decreases monotonically with k, the cross section of the confined impurity does not, and can be nonzero at arbitrarily high k.

2.4.1 Resonances

We wish to examine some of the features of the confined cross section in Fig. 2.4 in greater detail. In particular, we want to look at the resonances, and understand the effect of varying the scatterer position. Fig. 2.5 shows how the cross section and conductance vary as functions of energy, for three different values of y_0. We observe the general property that resonances in the cross section appear as new transverse modes open ($kd = n\pi$), unless the newly opened mode is zero at the scatterer. We further observe that the resonances have a universal structure: If a resonance exists at $kd = n\pi$, then

$$\lim_{kd \to n\pi^-} \sigma(k) = 0 \tag{2.66}$$

$$\lim_{kd \to n\pi^+} \sigma(k) = 1. \tag{2.67}$$

As the scatterer position changes, the character, shape, and number of resonances change also. In Fig. 2.5a), the scatterer is located at $y_0 = 0.05d$, where each of the modes is nonzero. Each resonance obeys (2.66-2.67). In Fig. 2.5c), the scatterer position is $y_0 = 0.32d$. Because $\chi_3(0.32d) \ll 1$, the resonance at $kd = 3\pi$ is much narrower than the others, and will in fact vanish if we move the scatterer slightly to $y_0 = d/3$. In Fig 2.5e), we observe such missing resonances– with the scatterer in the precise center of the wire, all even modes are zero there, and the resonances at $kd = 2\pi, 4\pi, 6\pi, \ldots$ have vanished.

Figs. 2.5b), 2.5d), and 2.5e) show the conductance for each scatterer position, which is related to the cross section by (2.64). Discontinuities such as (2.66-2.67) in the cross section lead to a continuously varying conductance. The impurity reduces the conductance by at most one stairstep. Comparing the conductance with (heavy line) and without the impurity (thin line), we observe that to the right of each mode opening, the conductance falls, generally to the value of the next-lowest stairstep.

From Fig. 2.5, our observations are as follows: (1) Resonances occur for values of k at which a new mode opens, unless the new mode is zero at the scatterer. (2) The general structure of a resonance is that the scatterer becomes transparent immediately before a mode opens, and that its cross section jumps

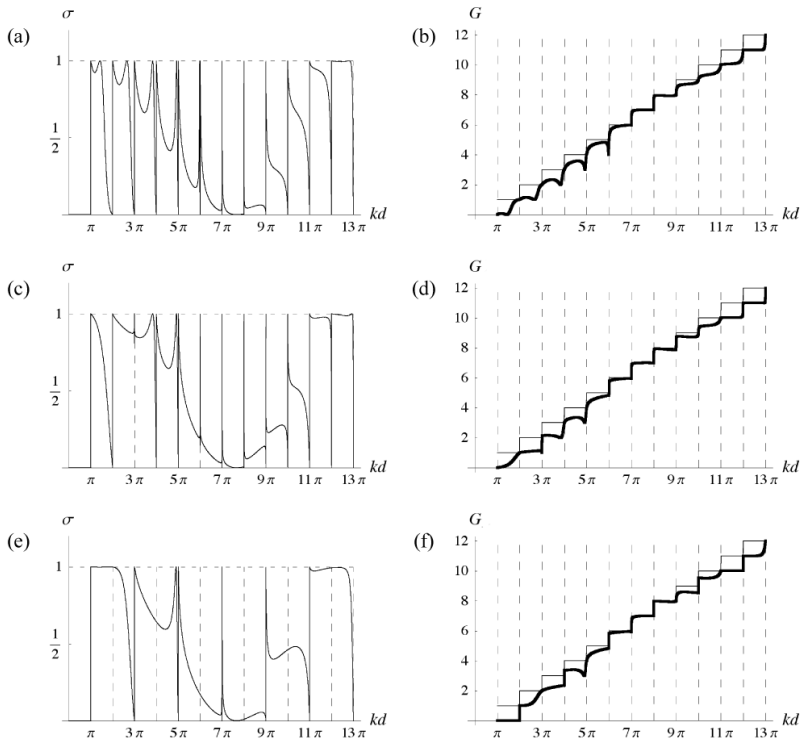

Figure 2.5: Cross sections (a,c,e) and conductances (b,d,f) vs. the wavenumber, k, for the scatterer at three different positions in the wire. The conductance is in units of the conductance quantum, $2e^2/\hbar$. The scatterer positions are $y_0 = 0.05d$ (a, b), $y_0 = 0.32d$ (c, d), and $y_0 = 0.50d$ (e, f). The scattering length is $a = 0.1d$. Resonances in the cross section appear as new transverse modes open ($kd = n\pi$). Discontinuities in the cross section lead to a continuously varying conductance: the two quantities are related by (2.64). The impurity reduces the conductance by at most one channel. Comparing the conductance with (heavy line) and without the impurity (thin line), we observe that to the right of each mode opening, the conductance falls, generally to the value of the next-lowest stairstep. Several references [4,6,7,20] obtain slightly different results for the conductance vs. wavenumber curve, in which $\sigma = 1$ just *below* the mode opening. We attribute the discrepancy to differences in how the point scatterer is modeled.

to one immediately after the mode has opened. (3) The shape and width of the resonances depend on the scatterer position, y_0. In Section 2.5, we shall prove these statements, and explain them in terms of interference effects.

Although we have examined the case of a repulsive scatterer in Fig. 2.5, our analytic and numerical results indicate that even for an attractive impurity ($a < 0$) the conductance is reduced by a single unit immediately after the subband opening $kd = n\pi$, rather than just below it. Similar results about the conductance reduction near the opening of each subband appear in other theoretical investigations of quantum wires; we cite some representative works [4,6,7,20]. One result [20] is for a scatterer in a rectangle, and therefore cannot be exactly compared to ours. However, the remaining references [4, 6, 7] treat the infinite wire, and show a slight difference from ours: In [4,7], which examine only attractive impurities, the reduction in conductance appears slightly *below* the subband opening. Ref. [6] examines both attractive and repulsive scatterers. For repulsive scatterers, Ref. [6] presents results similar to our Fig. 2.5, while for attractive scatterers the results of Ref. [6] resemble those in [4,7]. Because delta functions in more than one dimension do not scatter, many different methods exist of representing a point impurity in two dimensions. We have chosen to use a t matrix representation as in Refs. [11,15,16], and the particular t matrix we have chosen in (2.3) mimics the s wave scattering of a hard disk of radius a. The references whose results differ from ours have used explicit limiting forms of delta potentials. We attribute the slight difference in results to the different forms and representations of the point impurity.

2.4.2 Between Resonances

We have observed that the scatterer position in the wire influences not only the width and shape of the resonances, but can even cause a resonance to disappear. Between resonances, we note the opposite phenomenon: The scatterer position barely affects the cross section at all. As we vary the scattering length a, the cross section behaves very similarly to the free space cross section (see Fig. 2.6).

Our general observations from the numerical results are the following: (1) Scattering resonances occur where nonzero modes open. (2) The cross section jumps from zero to d across a resonance. (3) The width and existence of a resonance is influenced by y_0. (4) Away from resonances, the cross section behaves like the free space cross section.

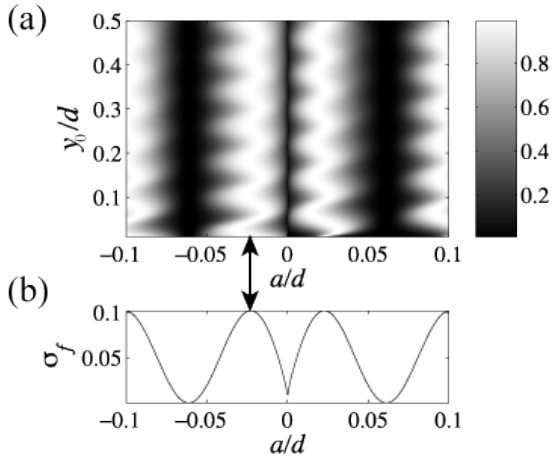

Figure 2.6: (a) Cross section of the confined scatterer for $kd = 12.5\pi$ (halfway between having 12 and 13 modes open). On the horizontal axis, we vary the effective scattering radius a from $-0.1d$ to $0.1d$. The vertical axis is y_0, the vertical position of the scatterer in the waveguide: y_0 varies from the edge of the wire ($y_0 = 0$) to the middle of the wire ($y_0 = 0.5$). In contrast to the case of a resonance, between resonances, the cross section is almost identical to the free space cross section σ_f, shown in (b); the arrow indicates two corresponding maxima. The only effect of varying y_0 is to introduce some small oscillations due to interference effects. The plots continue in a similar manner to the left and right.

2.5 Physical Phenomena Explained in Terms of a Single Scattering Wave Function

We have shown that items 1-2 in our list of Section 2.2.2 are characteristics of free space scattering which have analogs in the wire. We have yet to examine whether item 3 has an analog as well. In this section, we show that in the waveguide, as in free space, a basis exists in which only a single wavefunction scatters. We write this basis explicitly, and show that the scattering of this single wavefunction allows us to explain the confinement induced phenomena shown in Figs. (2.4-2.6) simply, in terms of reflections from the scatterer and its images.

2.5.1 Single Scattering Wavefunction and the Hall of Mirrors

In the basis of plane waves, the scatterer couples the channels so that, in general, an incoming mode scatters into all the modes. However,

$$\text{rank}\left[\mathbf{S} - \begin{pmatrix} \mathbf{0} & \mathbf{I} \\ \mathbf{I} & \mathbf{0} \end{pmatrix}\right] = 1, \tag{2.68}$$

which implies that a particular choice of basis exists in which only *one* of the incoming wavefunctions scatters at all, and is decoupled from the other $N-1$ basis functions. This wavefunction is the analog of the s wave in free space.

Another way of seeing that only one wavefunction scatters is by the following argument: For a given energy, N channels are open. Any incoming wavefunction is a linear combination of the N basis functions

$$\phi^{(n)}(x,y) = \frac{e^{\pm i k_x^{(n)} x}}{\sqrt{k_x^{(n)}}} \chi_n(y), \tag{2.69}$$

(we require only the left- or right-moving set). Any linear combination

$$\sum_{n=1}^{N} c_n \phi^{(n)}(x,y) \tag{2.70}$$

of the N basis functions (2.69) which is nonzero at the scatterer will satisfy

$$\sum_{n=1}^{N} c_n \phi^{(n)}(x_0,y_0) \neq 0. \tag{2.71}$$

Equivalently, define an $1 \times N$ matrix $\mathbf{W}$ such that $W_n = \phi^{(n)}(x_0,y_0)$ and a vector of coefficients $\vec{c} = [c_1, \ldots c_N]$. Then, for any scattering wavefunction, the c_n will satisfy

$$\mathbf{W}\vec{c} \neq \vec{0} \tag{2.72}$$

As $\mathbf{W}$ is a rank 1 matrix, only one solution exists. That solution is simply

$\vec{c} \in \mathrm{Nul}(\mathbf{W})^{\perp} = \mathrm{Row}(\mathbf{W}) = \mathbf{W}^{\dagger}$. That is, the single scattering wavefunction is

$$\phi_s^{\rightleftarrows}(x,y) = \sum_{n=1}^{N} \left(\phi^{(n)}(x_0,y_0)\right)^* \phi^{(n)}(x,y) \tag{2.73}$$

$$= \sum_{n=1}^{N} \frac{1}{k_x^{(n)}} \chi_n(y_0)\chi_n(y) e^{\pm i k_x^{(n)}(x-x_0)} \tag{2.74}$$

where the choice of sign determines whether the incoming wave is right or left-moving. Suppose we take a linear combination of the two so the scattering wavefunction is symmetric in x. The scattering wavefunction becomes

$$\phi_s(x,y) = \sum_{n=1}^{N} \frac{1}{k_x^{(n)}} \chi_n(y)\chi_n(y_0) \cos\left[k_x^{(n)}(x-x_0)\right] \tag{2.75}$$

(the other linear combination doesn't scatter). By comparison with (2.14), we recognize the above form of the scattering wavefunction as

$$\phi_s(x,y) = -\mathrm{Im} G_w(x,y;x_0,y_0;k). \tag{2.76}$$

Note that all the definitions in this section, and in particular (2.76), are independent of the specific form of $\chi_n(y)$, and thus apply to arbitrary guides, not only to the hard wire. As we shall discuss later, (2.76) is particularly important because it shows that for an arbitrary guide, we can obtain the scattering wavefunction entirely from the Green's function, which we can approximate semiclassically.

We now return to the specific case of the hard wire, and try to understand the scattering wavefunction physically. From (2.18), an alternate form of the Green's function is

$$G_w(\vec{r},\vec{r}_0,k) = -\frac{i}{2} \sum_{n=-\infty}^{\infty} (-1)^n H_0(k\,|\vec{r}-\vec{r}_n|) \tag{2.77}$$

where the $\vec{r}_n$ are the image positions. Combining (2.76) and (2.77), we find an alternate expression for the scattering wavefunction:

$$\phi_s(x,y) = \frac{1}{2} \sum_{n=-\infty}^{\infty} (-1)^n J_0(k\,|\vec{r}-\vec{r}_0|). \tag{2.78}$$

Eq. (2.78) shows that the analog of the free space s wave in the hard wire is, as we might have expected, simply the free space s wave, plus an infinite series of images–a "hall of mirrors s wave." We can complete the analogy between

free space and our wire by expressing the $N-1$ unscattered wavefunctions in terms of a "mirrors" basis. We do so by including higher order mirrored waves as in Table 2.1. The mirroring, and the signs assigned to each image, are somewhat subtle: Only those combinations of free space orbitals which satisfy the boundary conditions, but are also zero at the scatterer, will not scatter. We note that the basis in Table 2.1 is *not* an orthogonal one; inner products of an p wave centered on one image and a d wave centered on another image, for example, do not vanish, nor do the various such cross-terms cancel each other. However the important point is that the higher partial waves we have defined are all orthogonal to the mirror s wave: Higher mirrored partial waves do not scatter, whereas the mirror s wave does.

We note that the image sums in Table 2.1 converge slowly and are unsuitable for numerical purposes. However, we have the plane wave expansion (2.75) for the s wave, as well as the analogous expansion

$$\begin{aligned} \phi_s^+(\vec{r}) &= \frac{1}{2}\sum_{n=-\infty}^{\infty} J_0(k\,|\vec{r}-\vec{r}_n|) && (2.79)\\ &= \frac{2}{d}\sum_{n=1}^{N}\frac{1}{k_x^{(n)}}\cos\left(\frac{n\pi y}{d}\right)\cos\left(\frac{n\pi y_0}{d}\right) \\ &\qquad \times\cos\left[k_x^{(n)}(x-x_0)\right] && (2.80)\end{aligned}$$

for the s wave plus *positive* images. We can apply the raising operator

$$\hat{L}_+ \equiv \frac{1}{k}\left(\partial_x + i\partial_y\right) \tag{2.81}$$

to these plane wave expansions to obtain plane wave expansions for the higher partial waves. For example, we can obtain plane wave expansions of the waves in Table 2.1 as

$$\begin{array}{rcl} \phi_{p_x}(\vec{r}) &=& \mathrm{Re}\left[\hat{L}_+\phi_s(\vec{r})\right] \;=\; \frac{1}{k}\partial_x\phi_s(\vec{r}) \\ \phi_{d_{xy}}(\vec{r}) &=& \mathrm{Im}\left[\hat{L}_+^2\phi_s^+(\vec{r})\right] \;=\; \frac{2}{k^2}\partial_{xy}\phi_s^+(\vec{r}) \\ \phi_{f_{x^3-3xy^2}}(\vec{r}) &=& \mathrm{Re}\left[\hat{L}_+^3\phi_s(\vec{r})\right] \;=\; \frac{1}{k^3}\left(\partial_x^3 - 3\partial_x\partial_y^2\right)\phi_s(\vec{r}), \end{array}$$

and we could proceed similarly to obtain higher partial waves.

Mirrored wave	Expression	Wavefunction plotted for $kd = 40$ (twelve modes open)
s	$\frac{1}{2}\sum_{n=-\infty}^{\infty}(-1)^n J_0(k\,\lvert\vec{r}-\vec{r}_n\rvert)$	
p_x	$\frac{1}{2}\sum_{n=-\infty}^{\infty}(-1)^n J_1(k\,\lvert\vec{r}-\vec{r}_n\rvert)\cos\theta$	
d_{xy}	$\sum_{n=-\infty}^{\infty} J_2(k\,\lvert\vec{r}-\vec{r}_n\rvert)\sin 2\theta$	
$\vdots$	$\vdots$	$\cdots$

Table 2.1: Mirrors basis. The first column indicates the symmetry, the second column the expression, and the third column a plot, of each mirrored wave. The arrows in the plots indicate the impurity, located at $y_0 = 0.6d$. The mirror s wave (first row) is nonzero at the impurity position $\vec{r}_0$, and thus scatters. The scatterer is, however, transparent to the higher partial waves shown in the second through fourth rows. These partial waves, expressed as p_x,d_{xy},$f_{x^3-3xy^2}$ waves plus images, do not scatter due to their nodal lines along $x = x_0$ (indicated by the dashed white lines in the plots).

2.5.2 Interference Effects

We might expect that the cross section is related to the fraction of the single scattering wavefunction which actually scatters, and we might thus expect the cross section to be proportional to the amplitude of the mirror wavefunction at the scatterer. However, some numerics reveal that the mirror wavefunction alone is insufficient to fully describe the scattering. From (2.50) and (2.75), we find

$$\sigma = |\mathcal{R}s|^2 \, \phi_s(\vec{r}_0)^2 \tag{2.82}$$

$$= \left| s\tilde{\phi}_s(\vec{r}_0) \right|^2 \tag{2.83}$$

meaning that the relevant quantity is the *renormalized* mirror wavefunction, and that its value at the scatterer alone explains all the scattering phenomena. Eq. (2.83) is again independent of the form of the waveguide.

We have already discussed how renormalization of the scattering wavefunction arises from interference between all possible bounces off images. The implication of (2.83) is that the value of the resulting interference pattern at the location of the scatterer determines the cross section: At configurations (wire widths, incident wavenumbers, etc.) for which this interference is destructive at the scatterer, the scatterer is transparent. If the system is configured so that the bounces interfere constructively at the scatterer, a resonance results.

Semiclassical Approximations for General Wires

We wish to highlight another important point, which is that combining (2.83) with (2.33) and (2.76), we find that

$$\sigma = \lim_{\vec{r}\to\vec{r}_0} \left\{ \left| \frac{s\mathrm{Im}G_w(\vec{r},\vec{r}_0)}{1 - s\left[G_w(\vec{r},\vec{r}_0) - G_0(\vec{r},\vec{r}_0)\right]} \right|^2 \right\}. \tag{2.84}$$

The significance of (2.84), which applies to an arbitrary wire, is that the cross section is fully determined by the Green's function of the empty guide. This relation is important because the Green's function is a quantity which we can approximate semiclassically. Substituting the semiclassical Green's function into (2.84) will give us a semiclassical approximation to the cross section. Semiclassical methods may be of use in determining the transport properties of guiding potentials which are more complicated than the hard wire, and thus not amenable to exact quantum treatment.

2.5.3 Scattering Resonances and Conductance Reduction

In Figs. 2.4-2.5, we observed a reduction in the conductance, which are similar (although not identical) to the conductance dips observed in other theoretical investigations. [4,6,7,20] Using our formalism, we can understand the resonances and conductance dips of Figs. 2.4-2.5 simply, in terms of interference between different paths. Again the results of this section do not depend on the specific form of the transverse modes $\chi_n(y)$, and consequently apply to a general waveguide.

As we showed in (2.32), the renormalized mirror wavefunction contains contributions that have propagated from each of the image scatterers. We are interested in the behavior of a cross section when a mode is about to open. The mirror wavefunction involves only open channels, and is thus discontinuous across a mode opening. Using (2.75), we can examine the behavior of the mirror wavefunction near $kd = N\pi$, where the N^{th} mode opens. Suppose that the newly opened mode is nonzero at the scatterer, $\chi_N(y_0) \neq 0$. On the left of the mode opening,

$$\lim_{\epsilon \to 0} \phi_s \left(\vec{r}_0; k = \frac{N\pi - \epsilon}{d} \right) = \frac{d}{\pi} \sum_{n=1}^{N-1} \frac{\chi_n^2(y_0)}{\sqrt{N^2 - n^2}} \tag{2.85}$$

is finite. Immediately after the mode opening,

$$\lim_{\epsilon \to 0} \phi_s \left(\vec{r}_0; k = \frac{N\pi + \epsilon}{d} \right) = \frac{d}{\pi} \frac{\chi_N^2(y_0)}{\sqrt{2N\epsilon}} \tag{2.86}$$

diverges as $\epsilon^{-1/2}$. That is, the mirror wavefunction is always finite immediately before a nonzero mode opens, and diverges afterwards. The value of $\chi_N^2(y_0)$ determines the width of the resonance (and the lifetime of the corresponding quasibound state).

However, while the limiting behavior of the mirror wavefunction influences the shape of the resonances, it does not fully describe their shape. As we discussed, the general structure of a resonance is that σ drops to zero just before the mode opens; see e.g. Fig. 2.5. Clearly the incoming wavefunction, which includes only modes which are already open, cannot explain this transparency. The renormalization factor due to the wire, however, includes *all* modes, both evanescent and propagating–and unlike the incoming mirror wavefunction, varies continuously across the mode opening. Using the expression

(C.0.4) for G_r, we find that

$$\lim_{\epsilon\to 0} G_r\left(k=\frac{N\pi-\epsilon}{d}\right) = -\frac{d}{\pi}\frac{\chi_N^2(y_0)}{\sqrt{2N\epsilon}} \tag{2.87}$$

$$\lim_{\epsilon\to 0} G_r\left(k=\frac{N\pi+\epsilon}{d}\right) = -\frac{id}{\pi}\frac{\chi_N^2(y_0)}{\sqrt{2N\epsilon}} \tag{2.88}$$

generally. Combining (2.28) with the limits (2.85-2.88), and using (2.83), we can show that

$$\lim_{\epsilon\to 0}\sigma\left(k=\frac{N\pi}{d}-\epsilon\right) = 2N\epsilon\left|\sum_{n=1}^{N-1}\frac{\left[\chi_n(y_0)/\chi_N(y_0)\right]^2}{\sqrt{N^2-n^2}}\right|^2. \tag{2.89}$$

The value of $\chi_N(y_0)$ controls the width and structure of the resonance. Examining the right side of the resonance,

$$\lim_{\epsilon\to 0}\sigma\left(k=\frac{N\pi}{d}+\epsilon\right) = \lim_{\epsilon\to 0}\left|\frac{s}{1-sG_r}\right|^2\phi_s^2(\vec{r}_0) \tag{2.90}$$

$$\approx \frac{\phi_s^2(\vec{r}_0)}{|G_r|^2} \tag{2.91}$$

$$= 1$$

under the assumption that $|sG_r| \gg 1$. An important point to note is that when $|G_r| \to \infty$, as it does at a resonance, the free space properties of the scatterer have little effect on the cross section (see for example (2.90)), and so the structure of resonances is universal.

Phase Shift and Ramsauer-Townsend Effect

We would like to note, in passing, that the transparency of the scatterer at certain energies is reminiscent of the Ramsauer-Townsend effect in free space. In free space, we define the s wave phase shift δ_0 of an s wave scatterer by

$$\psi(\vec{r}) = \phi(\vec{r}_0) + \frac{e^{2i\delta_0}-1}{2}H_0^{(1)}(k\,|\vec{r}-\vec{r}_0|), \tag{2.92}$$

Let us define it in the confined scatterer as the phase shift of *each* s wave generated from the source and the images, when the incident wavefunction is

our mirror s wave:

$$\psi(\vec{r}) = \phi_s(\vec{r}) + \sum_{n=-\infty}^{\infty} \frac{e^{2i\delta_0} - 1}{2} \times(-1)^n H_0^{(1)}(k\,|\vec{r} - \vec{r}_n|) \tag{2.93}$$

Comparing to the form (2.26) of the Lippmann-Schwinger equation, we find that

$$e^{2i\delta_0} = 1 - is\tilde{\phi}_s(\vec{r}_0). \tag{2.94}$$

Applying (2.83), we find that

$$\sigma = \frac{1}{4}\left|1 - e^{2i\delta_0}\right|^2 \tag{2.95}$$

so that $\sigma = 0$ when $\delta_0 = 0, \pi$ and $\sigma = 1$ when $\delta_0 = \frac{\pi}{2}, \frac{3\pi}{2}$. As in the free space Ramsauer Townsend effect, the cross section vanishes when our analog of the s wave phase shift does.

In conclusion, we can make the following general statements about the cross section:

1. If $\chi_N(y_0) \neq 0$, the cross section will be discontinuous at $kd = N\pi$. The limit on the left hand side will be finite, and depend the value of $\chi_N(y_0)$. The limit on the right hand side will be unity.

2. The width and shape of the resonances in item (2) will depend on $\chi_N(y_0)$. Physically this means that one can tune the resonances by sliding the scatterer up and down in the wire, or by changing the nature of the confining potential.

2.5.4 Semiclassical Interpretation of Resonances

Having explored the structure of the resonances, we wish to understand them semiclassically, from an interference point of view. We again turn to the hard wire for insight into the scattering processes. The scattering cross section depends only on a single quantity, the renormalized mirror wavefunction. We have previously expressed this renormalized mirror wavefunction as a sum over the different paths ending on the scatterer (2.32). When the interference between these paths is maximally constructive, the cross section is maximal. When it is maximally destructive, the cross section vanishes.

In order to make this interference clearer, we shall make a simple approximation. Consider the most straightforward case, with the scatterer in the center of the wire (the case we examined in Fig. 2.4). The image positions are $\vec{r}_n = (0, nd)$. In the Green's function (2.18), we replace each Hankel function by its asymptotic form, which is equivalent to making a semiclassical approximation. This yields an approximate Green's function

$$G_w(\vec{r}, \vec{r}_0) = \frac{1}{\sqrt{2\pi}} e^{5\pi i/4} \sum_{n=-\infty}^{\infty} \frac{1}{\sqrt{k\,|\vec{r} - \vec{r}_n|}} \times e^{i(k|\vec{r}-\vec{r}_n| - n\pi)}. \tag{2.96}$$

The contribution from each image carries a phase related to the path length from the image to the observation point, as well as a Maslov index $e^{in\pi}$ describing the sign change after n reflections from the wire walls. In the limit that $\vec{r} \to \vec{r}_0$, we see that the contribution propagating to the scatterer from the n^{th} image has relative phase $e^{i(kd-\pi)n}$. For values of k such that

$$kd = (2p-1)\pi, \ p \text{ integer}, \tag{2.97}$$

all the scattered wavelets thus interfere constructively. Comparing with Fig. 2.4, we see that this constructive interference coincides precisely with the resonances which occur as new modes open.

To fully explain the structure of the resonances, and understand the scatterer's transparency just before modes open, we would have to consider the effects of renormalization in this approximation. We shall not pursue the semiclassical limit further here, as we have already examined the exact case in great detail in Section 2.5.3. However, purely from this simple semiclassical argument, we can see that the resonances induced by the wire are indeed related to interference effects between different reflections.

2.6 Conclusions and Future Directions

Combining the method of images with the idea of a single scattering wavefunction, we have developed a formalism with which to treat scattering from a single impurity confined in a quantum guide. We find many similarities between scattering in the confined geometry and scattering in free space: We have defined meaningful analogs of the free space cross section, optical theorem, partial waves, and Ramsauer-Townsend effect. Although the hard guide is particularly

useful for insight, many of our results apply to other types of waveguides also.

We have examined the transport properties of a confined scatterer, making several general observations about the existence, locations, and and characters of the resonances. Additionally, we have outlined a method for approximating the cross section and conductance semiclassically, for arbitrary guides. We have derived an effective optical theorem for general quantum wire potentials. Using the fact that a confined target is rank one, we have described the transport properties of the wire entirely in terms of a single scattering wavefunction, renormalized by reflections from the confining potential. Our central result is that the cross section of a confined impurity is

$$\sigma = \left| s\tilde{\phi}_s\left(\vec{r}_0\right)\right|^2, \tag{2.98}$$

where $\tilde{\phi}_s\left(\vec{r}\right)$ is the renormalized single scattering wavefunction, which includes interference effects due to reflections from the waveguide walls.

Despite the common use of the hard-walled guide as a theoretical model for 2DEG quantum wires, [4–6, 9] actual confining potentials for both atom waveguides as well as 2DEG quantum wires tend to be soft or even parabolic–whereas in nanotube quantum wires, the relevant boundary conditions are periodic (the periodic boundary case is also exactly solvable via the method of images, although we have not presented the derivation here). While the hard wall itself is not the best model for 2DEGs, it is the ideal system in which to examine how effects like conductance reduction, which are independent of the confining potential and occur in more realistic geometries, arise from simple reflection and interference phenomena. The effects of multiple scattering from the impurity are in fact very similar for general confining potentials (see e.g. the renormalized t matrix formalism) [1].

A second limitation of this work includes the inadequacy of the s wave scatterer model at high energies, and in particular at energies which are sometimes relevant when imaging electron flow. In Section 4.5 we extend our formalism to treat higher partial waves. Another possible extension of this work could be to examine the transport properties of many scatterers in the wire; for example, explicitly explaining the transition from ballistic to diffusive transport in terms of interference between multiple mirror wavefunctions.

Chapter 3

Scattering and Guiding by Atomic Walls

In this chapter, we propose using an array of attractive scatterers to guide matter waves. We begin by developing a multiple scattering formalism to describe the scattering of scalar waves from quasi-1D periodic and near-periodic gratings constructed from point scatterers, and embedded in 2D. Such gratings can be constructed from individual atoms, for example via the same techniques used to build "quantum corrals." We use our analytic results to motivate the use of the array of scatterers as a waveguide. We conclude with a numerical demonstration that a finite array of scatterers can behave like an effective light pipe for scalar waves, guiding a beam focused on one end of the array to the other end.

3.1 Introduction

In this chapter, we examine the possibility of guiding matter waves along a single row of atoms, analogous to a light wave being guided by a fiber optic. Arrays of scatterers frequently behave as waveguides. For example, light can be guided via scattering along arrays of spherical metal particles [23–25]. Guiding by discrete arrays also occurs in photonic crystals and waveguides, extensive investigations of which have been spearheaded by Joannopoulous (see e.g. [26]).

To address the possibility of guiding with a wall of atoms, we develop in Section 3.3 a general theory for the scattering of scalar waves from quasi-1D periodic gratings of point scatterers, embedded in 2D. Because of the periodicity, characteristics of solid state systems appear, including Bloch waves and

band structure. However, because the grating is periodic only in one direction, and finite in the other, Bloch waves coexist with scattering phenomena: Transmission coefficients, reflection coefficients, and resonances are present, in addition to conduction along the array. Although our setup is an unusual one, many regimes and characteristics which these gratings exhibit are clear analogs of physical phenomena in more conventional waveguides, which can be treated by continuum theory.

A possible application of the ideas in this chapter is to chains of atoms adsorbed on metallic surfaces: Single chains of Au atoms have, for example, been deposited on NiAl(110) [27, 28] as well as Si(553) [29]. Standing wave patterns in the differential conductance of similar patterned atom systems have been successfully modeled via Foldy's multiple scattering theory [18], where the individual scatterers were taken to be ideal s wave absorbers [30–32]. Our formalism is not specfically designed to model atoms confined in optical lattices. However, such a system also forms a grating, and certain aspects of the physics are similar to our setup (for example, visible light can Bragg diffract from Cs atoms confined in optical lattices [33]). Confined atoms could, thus, conceivably be used to guide as well.

We begin, in Section 3.2, with a brief review of Foldy's method. In Section 3.3, we apply Foldy's method to the general periodic array of scatterers. We discuss diffraction, transmission resonances, and other phenomena which exist for a general grating, continuing in Section 3.4 to examine quasibound and bound states which conduct along the grating. In Section 3.5 we apply the general results of Section 3.3 to the simplest periodic system, a single wall of scatterers. We calculate the band structure of the wall and show that it is possible for conducting states to exist at positive energies, permitting injection into these states from the outside. Finally, in Section 3.6, we numerically demonstrate guiding by finite, semiinfinite, and gently curved chains of attractive scatterers.

3.2 Background: Foldy's Method

To model multiple scattering, we make extensive use of Foldy's method, originally presented in [18]. Foldy's method is a general model for multiple scattering of scalar waves from isotropic point scatterers. In addition to successfully modeling transport in quantum corrals [31, 32], Foldy's method (with various boundary conditions) has been applied to model a wide range of systems including acoustic scatterers [34], cold neutrons [35], and screens of bubbles [36]. We review the method briefly in this section.

Consider a wave $\phi(\vec{r})$ incident on a collection of N identical point scatterers at positions $\{\vec{r}_1, \ldots, \vec{r}_N\}$, where $\vec{r}_n = (x_n, y_n)$. Applying the t matrix formalism [37], we characterize a single scatterer at $\vec{r}_i$ by its t matrix,

$$t = s(k) \left|\vec{r}_i\right\rangle \left\langle\vec{r}_i\right|$$

where $s(k)$ is a function of the wavenumber, $k = \sqrt{2mE}/\hbar$. We choose the functional form of $s(k)$ to simulate the scatterer of interest, under the constraint that $s(k)$ must satisfy the optical theorem

$$-\frac{2\hbar}{m}^2 \mathrm{Im}s(k) = |s(k)|^2 . \tag{3.1}$$

In the t matrix formalism, the Lippmann-Schwinger equation for multiple scattering is

$$\psi(\vec{r}) = \phi(\vec{r}) + s(k) \sum_{i=1}^{N} \psi_i(\vec{r}_i) G_0(\vec{r}, \vec{r}_i) \tag{3.2}$$

where

$$G_0(\vec{r}, \vec{r}_0) = \frac{2m}{\hbar^2} \left[-\frac{i}{4} H_0(k \left|\vec{r} - \vec{r}_0\right|) \right]$$

is the 2D free-space Green's function satisfying

$$(\vec{\nabla}^2 + k^2) G_0(\vec{r}, \vec{r}_0) = \frac{2m}{\hbar^2} \delta^{(2)}(\vec{r}, \vec{r}_0),$$

and the $\psi_i(\vec{r}_i)$ are defined recursively as

$$\psi_i(\vec{r}_i) = \phi(\vec{r}_i) + s(k) \sum_{\substack{j=1 \\ j \neq i}}^{N} \psi_j(\vec{r}_j) G_0(\vec{r}_i, \vec{r}_j). \tag{3.3}$$

The $\psi_i(\vec{r}_i)$ are *effective* incoming wavefunctions at each scatterer: $\psi_i(\vec{r}_i)$ is the amplitude incident on the i^{th} scatterer after scattering from each of the other scatterers. The $\psi_i(\vec{r}_i)$ exclude the singular self-interaction of the i^{th} scatterer. In the remainder of this chapter, we set $\hbar = m = 1$.

Defining two N x 1 column vectors, $\vec{\phi}$ and $\vec{\psi}$ whose i^{th} elements are given by $\vec{\phi}_i \equiv \phi(\vec{r}_i)$ and $\vec{\psi}_i \equiv \psi(\vec{r}_i)$ respectively, the Lippmann-Schwinger equation can be written as a simple matrix equation by inverting (3.2-3.3) to yield

$$\vec{\psi} = \mathbf{M}^{-1} \vec{\phi} \tag{3.4}$$

where

$$\mathbf{M} \equiv 1 - s\mathbf{G}$$

and the matrix $\mathbf{G}$, defined by

$$G_{ij} \equiv \begin{cases} 0 & i = j \\ G_0(\vec{r_i}, \vec{r_j}) & i \neq j, \end{cases} \tag{3.5}$$

excludes the singular self-interactions of each scatterer with itself.

Substituting the values of $\vec{\psi_i}$ from (3.4) into (3.2) yields an expression for the scattered wavefunction:

$$\psi(\vec{r}) = \phi(\vec{r}) + s\sum_{i=1}^{N} G_0(\vec{r}, \vec{r_i}) \left(\mathbf{M}^{-1}\vec{\phi}\right)_i . \tag{3.6}$$

3.3 Multiple Scattering From General Periodic Structures: Bloch Waves

We discussed in Section 4.5.1 how a lattice which is infinite in one direction, and finite in the other, combines the ideas of Bloch waves from solid state systems with the phenomena of reflection, transmission, and resonance typical to scattering problems. The system can thus be approached from multiple points of view. One approach might be to begin with the standard 3D solid state plane wave methods, which yield Bloch waves and band structure, and generalize those methods to the 2D case. We choose, instead, to apply multiple scattering theory to the array. The drawback of the multiple scattering approach is that it is somewhat more involved: however, Foldy's method yields information about individual scattering events within a unit cell and between unit cells, and it also generalizes more easily to the introduction of disorder into the lattice.

In this section, we apply Foldy's method from Section 3.2 to solve the Lippmann-Schwinger equation for a plane wave scattering from a general, infinite periodic array of clusters of point scatterers with a Bravais lattice spanned by $d\hat{y}$ (Fig. 3.1). Applying (3.4) directly, the multiple scattering solution would seem to require inversion of a biinfinite matrix. However, in this section we reduce the solution to inversion of the $N \times N$ matrix (where N is the number of scatterers per unit cell), and demonstrate how Bloch waves arise from multiple scattering theory. The resulting Lippmann-Schwinger equation resembles (3.4-3.5), but with an effective scattering strength $\tilde{s}$ and an effective Green's matrix $\tilde{\mathbf{G}}$ which account for multiple scattering between unit cells. The renormaliza-

tion and interference effects in a periodic grating are very similar to the effects encountered when a single point scatterer is placed in a confined geometry (see e.g. [38]). We discuss this point in detail in Section 3.5.

Our approach turns out to be related to the Korringa-Kohn-Rostoker (KKR) method [39, 40], with the variation that we have represented our scatterers by t matrices and have begun with an s wave approximation. A related approach was applied previously to study scattering from two-dimensional periodic slabs of scatterers embedded in three dimensions [41].

3.3.1 Multiple Scattering from a Periodic Grating

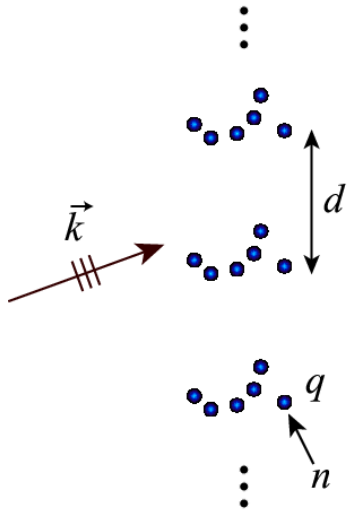

Figure 3.1: Plane wave incident on array with Bravais vector $d\hat{y}$. Unit cell is indexed by q, individual scatterer by n.

Denote by $\vec{r}_n^{(q)}$ the position of the n^{th} of N scatterers in unit cell q. We shall further suppose that all the scatterers in a unit cell are identical, with strength s, although the arguments in this section can easily be generalized for arbitrary scattering strengths. Applying Foldy's method, we can write the

Lippmann-Schwinger equation as

$$\psi(\vec{r}) = \phi(\vec{r}) + s \sum_{q=-\infty}^{\infty} \sum_{n=1}^{N} G_0(\vec{r}, \vec{r}_n^{(q)}) \psi_n^{(q)}(\vec{r}_n^{(q)}) \tag{3.7}$$

$$\psi_n^{(q)}(\vec{r}_n^{(q)}) = \phi(\vec{r}_n^{(q)}) + s \sum_{p=-\infty}^{\infty} \sum_{\substack{m=1 \\ (m,p)\neq(n,q)}}^{N} G_0(\vec{r}_m^{(p)}, \vec{r}_n^{(q)}) \psi_m^{(p)}(\vec{r}_m^{(p)}) \tag{3.8}$$

where

$$G_0(kr) = -\frac{i}{2} H_0(kr) \tag{3.9}$$

is the two-dimensional free space Green's function ($\hbar = m = 1$). Once again, if the effective incident wavefunction amplitudes at the scatterers, $\psi_n^{(q)}\left(\vec{r}_n^{(q)}\right)$ in (3.8), are known, the full wave function is determined using (3.7).

It is tedious, but straightforward to recursively sum and reindex (3.8) to show that for a translationally invariant incident wave,

$$\phi(\vec{r}) = e^{i\vec{k}\cdot\vec{r}}$$

the solutions to (3.8) are also translationally invariant:

$$\psi_n^{(q)}(\vec{r}_n^{(q)}) = e^{ik_y qd} \psi_n^{(0)}(\vec{r}_n^{(0)}). \tag{3.10}$$

Let us focus on the N scatterers in the unit cell indexed by $q = 0$. Using (3.10) on the right hand side of (3.8), evaluated for $q = 0$, we obtain

$$\psi_n^{(0)}(\vec{r}_n^{(0)}) = \phi(\vec{r}_n^{(0)}) + s \sum_{p=-\infty}^{\infty} \sum_{\substack{m=1 \\ (m,p)\neq(n,0)}}^{N} G_0(\vec{r}_m^{(p)}, \vec{r}_n^{(0)}) e^{ikypd} \psi_m^{(0)}(\vec{r}_m^{(0)}) \tag{3.11}$$

We wish to separate off the $m = n$ term, which corresponds to multiple scattering between each scatterer and its periodic counterparts in other unit cells. It is in this term that we must exclude the self interaction, which corresponds to

$m = n$ and $p = 0$. Breaking up the sum, we find

$$\begin{aligned}
\psi_n^{(0)}(\vec{r}_n^{(0)}) &= \phi(\vec{r}_n^{(0)}) + s \sum_{\substack{p=-\infty \\ p\neq 0}}^{\infty} G_0(k\,|p|\,d) e^{ikypd} \psi_n^{(0)}(\vec{r}_n^{(0)}) \\
&\quad + s \sum_{\substack{m=1 \\ m\neq n}}^{N} \left[\sum_{p=-\infty}^{\infty} G_0(\vec{r}_m^{(0)} + pd\hat{y}, \vec{r}_n^{(0)}) e^{ikypd} \right] \psi_m^{(0)}(\vec{r}_m^{(0)}) \\
&= \phi(\vec{r}_n^{(0)}) + sG_r \psi_n^{(0)}(\vec{r}_n^{(0)}) + s \sum_{m=1}^{N} \tilde{\mathbf{G}}_{mn} \psi_m^{(0)}(\vec{r}_m^{(0)})
\end{aligned}$$

where we have defined two quantities, a scalar quantity independent of the configuration of the unit cell,

$$G_r \equiv s \sum_{\substack{p=-\infty \\ p\neq 0}}^{\infty} G_0(k\,|p|\,d) e^{ik_y pd} \tag{3.12}$$

and an $N \times N$ matrix with entries

$$\tilde{\mathbf{G}}_{mn} = \begin{cases} 0 & m = n \\ \sum_{p=-\infty}^{\infty} G_0(\vec{r}_m^{(0)} + pd\hat{y}, \vec{r}_n^{(0)}) e^{ikypd}. & m \neq n \end{cases} \tag{3.13}$$

Defining the lattice sum

$$G(\vec{r}) = \sum_{p=-\infty}^{\infty} G_0(\vec{r}, pd\hat{y}) e^{ik_y pd} \tag{3.14}$$

we can rewrite (3.13) as

$$\tilde{\mathbf{G}}_{mn} = \begin{cases} 0 & m = n \\ G(\vec{r}_n^{(0)} - \vec{r}_m^{(0)}) & m \neq n \end{cases} \tag{3.15}$$

and then replace $G(\vec{r})$ in (3.14, 3.15) with the more rapidly converging expression (D.1.3), derived in Appendix D.

Defining vectors of wavelets

$$\vec{\phi}^{(0)} = \begin{pmatrix} \phi_1^{(0)}(\vec{r}_1^{(0)}) \\ \phi_2^{(0)}(\vec{r}_2^{(0)}) \\ \vdots \\ \phi_N^{(0)}(\vec{r}_N^{(0)}) \end{pmatrix},$$

$$\vec{\psi}^{(0)} = \begin{pmatrix} \psi_1^{(0)}(\vec{r}_1^{(0)}) \\ \psi_2^{(0)}(\vec{r}_2^{(0)}) \\ \vdots \\ \psi_N^{(0)}(\vec{r}_N^{(0)}) \end{pmatrix}$$

we can solve for the wavelets in the $q = 0$ unit cell:

$$\vec{\psi}^{(0)} = \frac{1}{1 - sG_r}\tilde{\mathbf{M}}^{-1}\vec{\phi}^{(0)} \tag{3.16}$$

where we have defined

$$\tilde{\mathbf{M}} = \mathbf{I} - \tilde{s}\tilde{\mathbf{G}}. \tag{3.17}$$

and

$$\tilde{s} = \frac{s}{1 - sG_r} \tag{3.18}$$

The remaining wavelets are then determined by (3.10):

$$\vec{\psi}^{(q)} = e^{ik_y qd}\vec{\psi}^{(0)}. \tag{3.19}$$

The full wavefunction is then given by substituting (3.16) and (3.19) in (3.7):

$$\psi(\vec{r}) = \phi(\vec{r}) + \tilde{s}\sum_{p=-\infty}^{\infty}\sum_{n=1}^{N} G_0(\vec{r}, \vec{r}_n^{(p)})e^{ik_y pd}\left(\tilde{\mathbf{M}}^{-1}\vec{\phi}^{(0)}\right)_n \tag{3.20}$$

$$= \phi(\vec{r}) + \tilde{s}\sum_{n=1}^{N}\left(\tilde{\mathbf{M}}^{-1}\vec{\phi}^{(0)}\right)_n \sum_{p=-\infty}^{\infty} G_0(\vec{r} - \vec{r}_n^{(0)}, pd\hat{y})e^{ik_y pd} \tag{3.21}$$

$$= \phi(\vec{r}) + \tilde{s}\sum_{n=1}^{N} G(\vec{r} - \vec{r}_n^{(0)})\left(\tilde{\mathbf{M}}^{-1}\vec{\phi}^{(0)}\right)_n \tag{3.22}$$

We note the similarity between (3.22) and (3.6): We can go from a single unit cell to a repeating array simply by replacing the t matrix $s(k)$ with its renormalized

version $\tilde{s}(\vec{k})$, and the free space Green's function $G_0(\vec{r};k)$ with the effective Green's function $G(\vec{r};k)$. The wavefunction (3.20) is a Bloch wave:

$$\psi(\vec{r}+d\hat{y}) = e^{ik_y d}\psi(\vec{r})$$

and the mapping from a single unit cell to an infinite array of unit cells is essentially a consequence of Bloch's theorem.

In this section, we have derived the scattered wavefunction when a plane wave is incident on a periodic grating. We have shown how Bloch waves emerge from Foldy's multiple scattering formalism, and that multiple scattering between unit cells gives rise to a renormalized scattering strength and effective Green's function. We now use our formalism to understand the transport phenomena which result when a plane wave is incident on a periodic grating, keeping in mind that our grating is also a quasi-1D "wire" which can transport waves along its axis.

3.3.2 Diffraction

The results in (3.14) are expressed as a superposition of spherical waves. In order to study diffraction, we choose to express the results in a basis of plane and evanescent waves. Using the lattice sums calculated in (D.1.3), we find that an alternate expression for (3.14) is

$$G(\vec{r}-\vec{r}_n^{(0)}) = -\frac{i}{d}e^{ik_y(y-y_n^{(0)})}\sum_{q=-\infty}^{\infty}\frac{1}{k_x^{(q)}}e^{ik_x^{(q)}|x-x_n^{(0)}|}e^{-\frac{2iq\pi}{d}(y-y_n^{(0)})} \tag{3.23}$$

where

$$k_y^{(q)} \equiv k_y - \frac{2q\pi}{d} \tag{3.24}$$

$$k_x^{(q)} \equiv \sqrt{k^2-\left(k_y^{(q)}\right)^2}. \tag{3.25}$$

Consider an incident beam

$$\phi(\vec{r}) = \frac{1}{\sqrt{k_x^{(0)}}}e^{i\vec{k}\cdot\vec{r}}$$

where we have normalized the incident beam to have unit flux on the unit cell of the array in order for unitarity of the **S** matrix to follow directly from current conservation.

Substituting (3.23) into (3.22) yields a plane plus evanescent wave expansion for the scattered wave:

$$\psi(\vec{r}) = \frac{e^{i\vec{k}_0\cdot\vec{r}}}{\sqrt{k_x^{(0)}}} - \frac{i\tilde{s}}{d}\sum_{q=-\infty}^{\infty}\sum_{n=1}^{N}\left(\tilde{\mathbf{M}}^{-1}\vec{\phi}^{(0)}\right)_n \frac{1}{k_x^{(q)}} e^{ik_x^{(q)}|x-x_n^{(0)}|} e^{ik_y^{(q)}(y-y_n^{(0)})}. \quad (3.26)$$

Eq. (3.26) is, in essence, Bragg diffraction: in the near field of the array, the wave contains an evanescent part, whereas in the far field the solution consists of diffracted plane waves propagating at the Bragg angles (3.24-3.25). The values of q for which $k_x^{(q)}$ is real correspond to diffracted plane waves, while the remaining values of q correspond to evanescent waves. The set $\mathcal{Q}$ of open channels, corresponding to diffracted plane waves, is defined by $\mathcal{Q} = [Q_{min}, Q_{max}]$ where

$$Q_{min} = \left\lceil \frac{(-k+k_y)d}{2\pi} \right\rceil \quad (3.27)$$

$$Q_{max} = \left\lfloor \frac{(k+k_y)d}{2\pi} \right\rfloor. \quad (3.28)$$

Only these open channels contribute in the far field. Note that for off normal incidence, $Q_{min} \neq -Q_{max}$.

In the far field, defined by $|x| \gg |x_n|$ for all n, we have the transmitted and reflected wavefunctions

$$\psi_r(\vec{r}) = \sum_{q\in\mathcal{Q}} R_q \frac{1}{\sqrt{k_x^{(q)}}} e^{-i\vec{k}_x^{(q)}x + ik_y^{(q)}y}$$

$$\psi_t(\vec{r}) = \sum_{q\in\mathcal{Q}} T_q \frac{1}{\sqrt{k_x^{(q)}}} e^{i\vec{k}_x^{(q)}x + ik_y^{(q)}y}$$

where we can read off from (3.26) that

$$R_q = -\frac{i\tilde{s}}{d} \times \frac{1}{\sqrt{k_x^{(q)}}} \sum_{n=1}^{N} (\tilde{\mathbf{M}}^{-1}\vec{\phi}^{(0)})_n e^{ik_x^{(q)}|x_n^{(0)}|} e^{-ik_y^{(q)}y_n^{(0)}}. \quad (3.29)$$

$$T_q = \delta_q - \frac{i\tilde{s}}{d} \times \frac{1}{\sqrt{k_x^{(q)}}} \sum_{n=1}^{N} (\tilde{\mathbf{M}}^{-1}\vec{\phi}^{(0)})_n e^{-ik_x^{(q)}|x_n^{(0)}|} e^{-ik_y^{(q)}y_n^{(0)}}. \quad (3.30)$$

We can define total reflection and transmission probabilities for the wall as

$$R = \sum_{q\in\mathcal{Q}} |R_q|^2 \tag{3.31}$$

$$T = \sum_{q\in\mathcal{Q}} |T_q|^2 . \tag{3.32}$$

The value of $\tilde{s}$ is constrained by combining (3.31-3.32) with the unitarity requirement $R+T=1$. This constraint is an analog of an optical theorem for the grating.

3.4 Mechanisms for Guiding: Quasibound and Bound States

Our goal in this chapter is to understand how waves can be guided along the grating. In this section, we discuss two mechanisms for conduction along the grating. Section 3.4.1 discusses quasibound states which arise purely due to the array's periodicity. Quasibound states have a finite lifetime; conduction in these states is limited by wave amplitude shedding off the periodic array. Similar quasibound states appear in a number of periodic systems ranging from periodic ocean coastlines to acoustics [42, 43]. The difference between a grating of atoms and the other periodic systems we have mentioned is that the individual atoms in a grating can possess bound states. These bound states can potentially give rise to bands of states which, in contrast to the quasibound states, are truly conducting along the array. In Section 3.4.2 we outline the criteria for the existence of these states. We shall examine both the quasibound and bound states, and their role in guiding, in more detail in Section 3.5. A third possible mechanism of guiding which we do not examine in this chapter is total internal reflection; this requires a thick array of scatterers which can behave like an effective medium.

Guided waves which propagate along periodic structures are termed Rayleigh-Bloch surface waves, or trapped waves, and are discussed in [44, 45]. These trapped waves are evanescent in the direction transverse to the array: They conduct along the array, but they do not carry energy away from the array. Trapped waves have been examined in a variety of physical contexts, including electromagnetics, acoustics, water waves, and edge waves along periodic coastlines [42]. In acoustics, trapped modes have become known as "Parker resonances," and can be excited by vortex shedding when air flows parallel to a set

of equally spaced flat plates [43].

3.4.1 Trapped Waves and Quasibound States

From (3.26), resonances occur when $k_x^{(q)} \to 0$, i.e., whenever one of the diffracted beams becomes parallel to the array: A similar process in atom-surface scattering is known as selective adsorption [46]. These threshold resonances are purely due to the periodicity of the array, and their existence does not depend on the scatterer configuration within the unit cell. From (3.25), a diffracted beam becomes parallel to the array when $k \to k_y^{(q)} \pm \epsilon$, and the lattice sum (D.2.7) yields

$$\lim_{k=k_y^{(q)}\pm\epsilon} G_r = -\frac{i}{d}\frac{1}{\sqrt{\pm 2k_y^{(q)}\epsilon}}. \tag{3.33}$$

From (3.18) and (3.33), we find that

$$\lim_{k=k_y^{(q)}\pm\epsilon} \tilde{s} = \frac{1}{G_r} \tag{3.34}$$

From (3.34), the dependence of $\tilde{s}$ on the bare t matrix $s(k)$ cancels. The threshold resonances are thus kinematical rather than dynamical: The resonance energies are independent not only of the configuration of each unit cell, but also of the properties of the individual scatterers. The shape of each resonance, however, does depend on the types of scatterers and their arrangement in a unit cell.

Near these resonances, the scattered wave travels along the y axis:

$$\begin{aligned}\lim_{k=k_y^{(q)}-\epsilon} \psi(\vec{r}) &= e^{i\vec{k}\cdot\vec{r}} + \sum_{n=1}^{N}\left(\tilde{\mathbf{M}}^{-1}\vec{\phi}^{(0)}\right)_n \\ &\quad \times e^{-\sqrt{2k_y^{(q)}\epsilon}\left|x-x_n^{(0)}\right|} e^{ik_y^{(q)}(y-y_n^{(0)})} + \mathrm{O}(\epsilon^{1/2})\end{aligned} \tag{3.35}$$

$$\begin{aligned}\lim_{k=k_y^{(q)}+\epsilon} \psi(\vec{r}) &= e^{i\vec{k}\cdot\vec{r}} + \sum_{n=1}^{N}\left(\tilde{\mathbf{M}}^{-1}\vec{\phi}^{(0)}\right)_n \\ &\quad \times e^{i\sqrt{2k_y^{(q)}\epsilon}\left|x-x_n^{(0)}\right|} e^{ik_y^{(q)}(y-y_n^{(0)})} + \mathrm{O}(\epsilon^{1/2})\end{aligned} \tag{3.36}$$

Fig. 3.2 illustrates a threshold resonance as in (3.35-3.36). As we approach threshold from below, the scattered state approaches a state which begins as bound in the x direction (Fig. 3.2a), but becomes progressively more weakly bound as we approach threshold. At threshold, the scattered state merges with the continuum, and for wavenumbers just above threshold, the scattered state

propagates slowly in the x direction (Fig. 3.2b). The threshold resonance thus corresponds to quasibound states which conduct along the wire. Because of resonant tunneling to other states, and because these states do not exist in the absence of an incoming wavefunction, these states are quasibound rather than truly bound. From (3.35-3.36), exactly on a threshold resonance, the array is entirely transparent and the incident beam is entirely transmitted. This transparency is a form of the Ramsauer-Townsend effect.

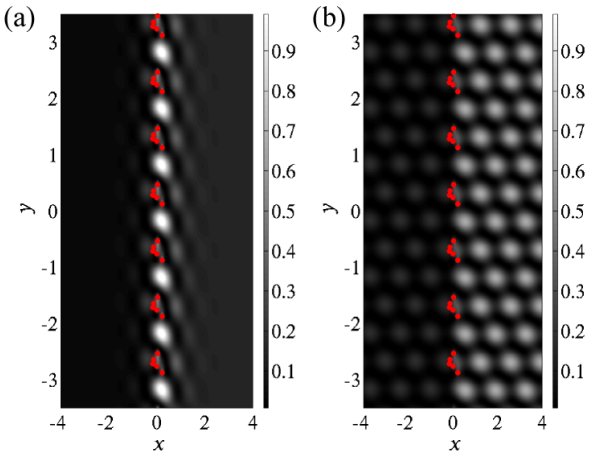

Figure 3.2: Threshold resonance for a unit cell with five randomly placed scatterers (hard disks, $a = 0.1$). For clarity, we show only the scattered wavefunction; the incident wave is a plane wave and is fully transmitted. The quasibound state just below resonance, at wave number $kd = 2\pi - 0.3$, becomes unbound just above resonance, at $kd = 2\pi + 0.3$ (right). The scattered wavefunction just above and below threshold is given by (3.35, 3.36). The scattered wavefunction is asymmetric across $x = 0$ because the unit cell is; a symmetric unit cell would yield a symmetric scattered wavefunction.

3.4.2 Conducting States

An array of attractive scatterers, in the limit where the scatterers are closely spaced, should resemble a 2D potential trough. We thus expect that an array of attractive scatterers will give rise to a set of states which are purely bound along the array. Such conducting states, like the quasibound states discussed in Section 3.4.1, would be evanescent in the x direction, but free in the y direction, and thus correspond to states conducting along the array. In contrast to the quasibound states in Section 3.4.1, which in a time dependent picture eventually

leak away from the wire, a true conducting state would conduct forever. We are particularly interested in conducting states which might be experimentally accessible and relevant to scattering processes, and we theref ore search for conducting states that exist for positive energies.

In any quantum system, a bound state must be localized, and exist in the absence of an incoming wavefunction. For a single point scatterer in free space, the existence of bound states thus corresponds to negative energy poles of the t matrix. In the array scattering case, Foldy's method turns the Lippman-Schwinger equation into the matrix equation (3.16), which we rewrite as

$$\left[(1 - sG_r)\,\tilde{\mathbf{M}}\right]^{-1} \vec{\psi}^{(0)} \quad = \quad \vec{\phi}^{(0)}. \tag{3.37}$$

The existence of a scattered wavefunction for a zero incoming wavefunction implies the existence of a homogeneous solution to (3.37). States which exist in the absence of an incoming wave thus exist at values of $\vec{k}$ which are roots of the secular equation

$$(1 - sG_r)^N \det \tilde{\mathbf{M}} = 0. \tag{3.38}$$

For the single wall, (3.38) simply becomes

$$1 - sG_r = 0. \tag{3.39}$$

It is not a given that bound states exist for a particular grating. While the quasibound states in Section 3.4.1 exist independent of the t matrix of the individual scatterers, the bound states determined from (3.38) depend on $s(k)$. An array of repulsive scatterers, while possessing infinitely many quasibound states, would not have any truly bound states.

We are interested in states which conduct along the array. Such states, which are evanescent in the $\hat{x}$ direction but propagate in the $\hat{y}$ direction, correspond to wavevectors of the form

$$\vec{k} = i\kappa_x \hat{x} + k_y \hat{y} \tag{3.40}$$

where κ_x is real. The solutions we seek to (3.38) are thus of this form. In order to find conducting states, we evaluate $\tilde{s}$ on a grid of values of (κ_x, k_y), and numerically search for poles. The energy of a bound state with wavevector (3.40) corresponds to an energy

$$E = \frac{1}{2}\sqrt{-\kappa_x^2 + k_y^2}.$$

A bound state which has $E > 0$ corresponds to a pole of the renormalized t

matrix, with $|k_y| > |\kappa_x|$. The conducting states depend sensitively on the nature of the individual scatterers, and must be calculated for a specific grating. In Section 3.5 we examine the conducting states for a single wall of atoms.

In this section, we have outlined a number of phenomena which are general to periodic gratings: Diffraction, the existence of quasibound conducting states at threshold resonances, and the equations determining the existence of bound states. To proceed, we must now choose a particular form of grating. In Section 3.5, we examine, in detail, the simplest grating which exhibits all of these features: the single wall of atoms.

3.5 Transport by Single Walls

The results of Section 3.3 combine two effects: multiple scattering effects within each unit cell, which are contained in the inversion of the matrix $\tilde{\mathbf{M}}$, and multiple scattering effects between unit cells, which are contained in the renormalized t matrix $\tilde{s}$ and the effective Green's function $G(\vec{r})$. In Section 3.3 we discussed certain effects which are independent of the configuration of each unit cell, e.g. diffraction, the existence of subthreshold bound states, and the existence of a set of purely bound states. In order to understand these effects which are purely due to periodicity, we examine a periodic array of equally spaced scatterers. Consider a beam $\phi(\vec{r}) = \frac{1}{\sqrt{k_x}} e^{i\vec{k}\cdot\vec{r}}$ incident on a wall of atoms at positions $\vec{r}_n = (0, nd)$. For this array, the second term in (3.16) (which corresponds to

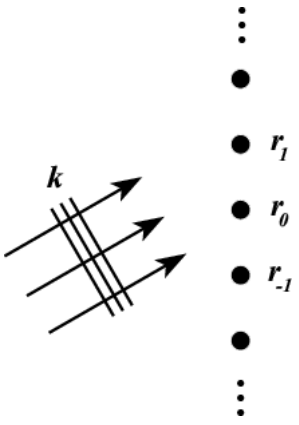

Figure 3.3: Scattering from a line of atoms.

multiple scattering within the unit cell) vanishes. Applying the formalism of

Section 3.3, the scattered wavefunction is

$$\psi(\vec{r}) = \phi(\vec{r}) + \tilde{s} \sum_{n=-\infty}^{\infty} G_0(\vec{r}, \vec{r}_n) e^{ik_y nd} \phi(0). \tag{3.41}$$

This result has been obtained in [34] via a different approach, in the context of scattering solutions to the semiinfinite array.

We note the similarity of our entire formalism to the formalism for scattering from point scatterers in a confined geometry (see e.g. [1], [11]). When a cluster of scatterers is placed in an external confining potential, the effect of the external potential can be absorbed into a renormalized t matrix and a new Green's function; the renormalized t matrix for a confined geometry in fact has a general form very similar to (3.18). The similarity results from the fact that both scattering from gratings and scattering in confined geometries involve interference phenomena related to multiple scattering. In a grating, renormalization effects arise due to multiple scattering between unit cells. If a single unit cell is placed in a waveguide, similar renormalization effects arise because reflection from the waveguide walls leads to multiple scattering from the unit cell.

For scattering from impurities confined in periodic or hard walled 2D strip waveguides, the mapping from a grating to a confined geometry is exact. Applying the method of images to a cluster of scatterers in a hard-walled or a periodic guide yields an array of image scatterers. Mathematically, the only difference between these confined geometries and the array is that in a confined geometry, the incident wave must satisfy the boundary conditions of the waveguide. In [38], we examined the case of a point impurity confined to a two-dimensional hard walled waveguide. With $k_y = 0$, (3.41) has the same form as the scattered wavefunction for a periodic wire with a scatterer in the middle, whereas if $k_y = \frac{\pi}{d}$ we recover the case of a Dirichlet waveguide with a scatterer in the middle.

In Section 3.6 we discuss why breaking the translational symmetry of the system, for example by truncating the infinite array, is required in order to use the array as a waveguide. Where possible, in this section we have compared the analytic results for the infinite array with corresponding numerical results for the semiinfinite wall. The methods we use in this section relate to work on other similar systems: scattering from a continuous, semiinfinite two dimensional line was solved analytically in a classic work by Sommerfeld [47]. Ref. [34] treats the problem of the infinite discrete array directly rather than as a special case of the results in Section 3.3, and applies the result to approximate scattering from

a discrete, semiinfinite array, and Ref. [48] treats scattering from continuous rather than discrete of atoms.

3.5.1 Walls of Scatterers and Unitarity

In this section we derive an effective optical theorem for the single wall of scatterers, and suggest that a similar optical theorem must be imposed in order to use the methods presented in Ref. [48]. Consider a beam

$$\phi(\vec{r}) = \frac{1}{\sqrt{k_x^{(0)}}} e^{i\vec{k}\cdot\vec{r}}$$

incident on the infinite array. In order for unitarity of the **S** matrix to follow directly from current conservation, we have normalized the incident beam to have unit flux on the unit cell of the array. For $|x|$ very large, (3.26) simplifies to give a plane wave expansion of the far field scattered wavefunction

$$\psi(\vec{r}) = \frac{1}{\sqrt{k_x^{(0)}}} e^{i\vec{k}_0\cdot\vec{r}} - \frac{i}{d}\tilde{s}\left[\sum_{q\in\mathcal{Q}} \frac{1}{\sqrt{k_x^{(0)}k_x^{(q)}}} \times \frac{1}{\sqrt{k_x^{(q)}}} e^{ik_x^{(q)}|x|} e^{ik_y^{(q)}y}\right] \quad (3.42)$$

We have omitted the evanescent modes, which decay far from the wall. Suppose the incident beam is at normal incidence, $\vec{k} = k\hat{x}$. The reflection and transmission probabilities from the incident (0^{th}) mode into the q^{th} mode are

$$\begin{aligned} R_q &= -\frac{i\tilde{s}}{d}\frac{1}{\sqrt{k_x^{(0)}k_x^{(q)}}} \\ T_q &= \delta_{q0} + R_q \end{aligned} \quad (3.43)$$

Unitarity of the **S** matrix requires that

$$\sum_{q\in\mathcal{Q}} \left(|R_q|^2 + |T_q|^2\right) = 1$$

or

$$\mathrm{Re}R_0 = -\sum_{q\in\mathcal{Q}} |R_n|^2 . \quad (3.44)$$

Eq. (3.44) relates the total probability of reflection to the real part of the coefficient reflected in the backwards direction. Furthermore, (3.44) yields an effective optical theorem for the wall, i.e., a restriction on the renormalized t

matrix resembling the ordinary optical theorem (3.1):

$$-\mathrm{Im}\tilde{s} = |\tilde{s}|^2 \sum_{q\in\mathcal{Q}} \frac{1}{k_x^{(q)} d}. \tag{3.45}$$

Using (3.18) and (D.2.7), it is straightforward to verify that $\tilde{s}$ satisfies the unitarity condition (3.45) as long as the single-scatterer t matrix $s(k)$ satisfies the free space unitarity condition

$$|s|^2 = -2\mathrm{Im}s.$$

In Appendix E we connect our formalism to the boundary wall method described in Ref. [48] for studying scattering from arbitrarily curved walls.

3.5.2 Phenomena Related to Guiding: Quasibound States and Conducting States

3.5.2.1 Threshold Resonances and Quasibound States

We define R, the total probability of reflection as

$$\begin{aligned} R &= \sum_{q\in\mathcal{Q}} |R_n|^2 \\ &= -\mathrm{Re}R_0 \\ &= -\frac{\mathrm{Im}\tilde{s}}{k_x^{(0)} d} \end{aligned}$$

where we have used (3.43,3.44). The total transmission T is, then

$$\begin{aligned} T &= 1 - R \\ &= 1 + \frac{\mathrm{Im}\tilde{s}}{k_x^{(0)} d}. \end{aligned}$$

From (D.2.7), as the incident beam becomes parallel to the array,

$$\lim_{k=k_y^{(q)}\pm\epsilon} G_r = -\frac{i}{d}\frac{1}{\sqrt{\pm 2k_y^{(q)}\epsilon}}$$

approaches infinity near resonances, and at these energies $T \to 1$ even when the scatterers are close together. The energies of the threshold resonances are independent of the properties of the individual scatterers that make up the wall:

Approaching a threshold resonance,

$$\lim_{k=k_y^{(q)}\pm\epsilon} \tilde{s} = \frac{1}{G_r} \tag{3.46}$$

so that from (3.46), all dependence on the bare t matrix $s(k)$ cancels. The shapes of the resonances do depend on the scatterers.

Fig. 3.4 shows the transmission of the wall as a function of the wavenumber of the incident beam. The transmission is nearly zero at low k, for which the scatterer spacing is comparable to the wavelength, but the incident wave is fully transmitted at high energies, where the scatterers are far apart compared to a wavelength. In this limit we explicitly recover semiclassical ray-tracing: Substituting the asymptotic form of the Hankel function in (D.1.1), we obtain the semiclassical expression

$$G(\vec{r}) \approx \frac{1}{2} e^{-3i\pi/2} \sum_{n=-\infty}^{\infty} \sqrt{\frac{2}{\pi k \left|\vec{r}-\vec{r}_n\right|}} e^{ik|\vec{r}-\vec{r}_n|} e^{ik_y nd}.$$

The wavefunction at $\vec{r}$ includes a contribution from each scatterer, with the appropriate phase. The phase includes a contribution proportional to the classical action (in this case, the path length to the scatterer) in addition to the phase of the incident wavefunction at the scatterer.

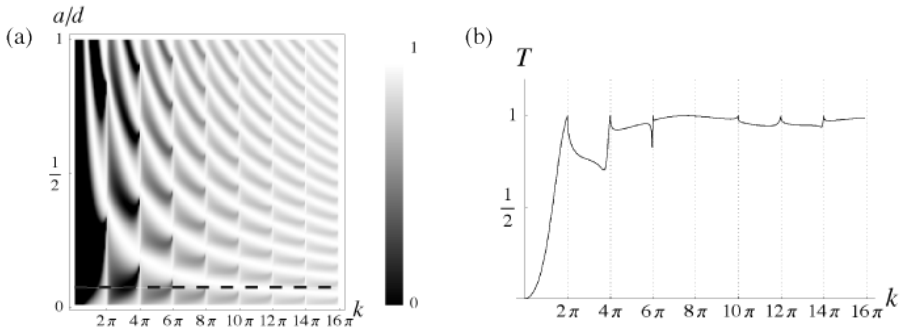

Figure 3.4: (a) Transmission coefficient for scattering of an incident beam with wavenumber k from a wall of hard disks with radius a. The incident beam is at normal incidence ($k_y^{(0)} = 0$). At low energies, the beam is fully reflected; at high energies the beam is almost entirely transmitted. Note the transmission resonances occur at $k = k_y^{(n)}$, which are discussed further in Section 3.5.2.1. (b) Structure of the resonances at $a = 0.1$ (dashed line in (a)).

Quasibound States As demonstrated in Section 3.3, the incident beam is transmitted near a resonance, but the *scattered* wave travels along the y axis. For the single chain of atoms, (3.35,3.36) simplify to

$$\lim_{k=k_y^{(q)}-\epsilon} \psi(\vec{r}) = e^{i\vec{k}_0\cdot\vec{r}} + \frac{i}{d} e^{-\sqrt{2k_y^{(n)}\epsilon}|x|} e^{ik_y^{(n)}y} + \mathrm{O}(\epsilon^{1/2}) \tag{3.47}$$

$$\lim_{k=k_y^{(q)}+\epsilon} \psi(\vec{r}) = e^{i\vec{k}_0\cdot\vec{r}} - \frac{1}{d} e^{i\sqrt{2k_y^{(n)}\epsilon}|x|} e^{ik_y^{(n)}y} + \mathrm{O}(\epsilon^{1/2}). \tag{3.48}$$

For the infinite array, the incident beam is fully transmitted at threshold: Flux is conserved because the trapped wave carries no current away from the array. This transparency of the wall at threshold is related to the Ramsauer-Townsend effect. Fig. 3.5 illustrates the threshold resonance, and compares results for the infinite wall with numerical results for the finite wall. Our numerical results suggest that the trapping is significantly weaker for the finite array, as amplitude sheds off the array and also diffracts from the ends. For the finite array, however, the trapped state does not behave very differently above and below threshold.

3.5.2.2 Conducting States and Band Structure for the Single Wall

In Section 3.4.2, we discussed conducting states bound in the x direction, as well as the criteria for such states to exist. For the single wall, these states satisfy (3.39). We examine these states in detail in this section. The presence or absence of bound states depends sensitively on the form of the scatterer potential: an extreme example is that no wall of repulsive hard disks will bind. We discussed in Section 3.2 how a t matrix could exactly simulate the s wave scattering from any potential, if we chose the form of $s(k)$ appropriately; we here briefly discuss how to choose our t matrix $s(k)$ to simulate particular potentials.

Generic Scatterers with a Bound State We choose $s(k)$ to represent a scatterer with a bound state at $k = i\kappa$. This requires that $s(k)$ have a pole at $k = i\kappa$, satisfy the free space optical theorem (3.1), and vanish as $k \to 0$. By arguments similar to [49, p. 417] we find that the simplest form of $s(k)$ which satisfies these requirements is

$$s(k) = \frac{-2ik}{k - i\kappa}. \tag{3.49}$$

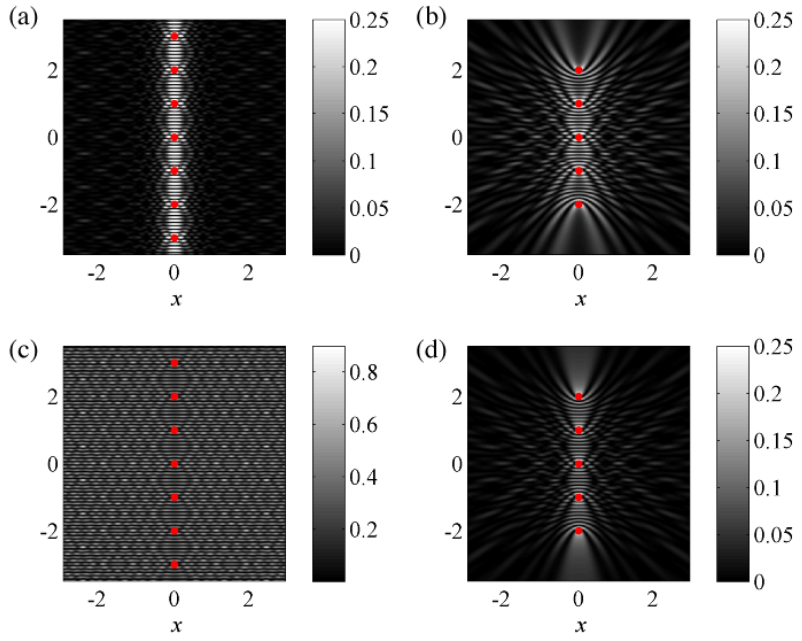

Figure 3.5: Quasibound States at Threshold Resonances: Probability density $|\psi_s(\vec{r})|^2$ of the scattered wavefunction near threshold for $kd = 10\pi - 0.1$ ((a), (b)) and $kd = 10\pi + 0.1$ ((c), (d)). This figure shows only the scattered portion of the wavefunction; the full wavefunction is given for the infinite array in (3.47, 3.48). We have omitted the incident plane wave, as it obscures the features we wish to emphasize. We have assumed normal incidence ($k_y^{(0)} = 0$). Comparing the finite ((a), (c)) and infinite ((b),(d)) arrays, the trapped wave remains mostly trapped in the finite array–though the trapping is weaker, and some leakage away from the array is visible. The tradeoff is that in contrast to the infinite array (c), the finite array shows trapping even above threshold (d).

Soft Disk The potential in Section 3.5.2.2 is a generic representation of a bound state, and does not correspond to a physical potential; for any realistic potential, $s(k)$ should vanish as $k \to \infty$. An example of a potential for which we can analytically calculate the s wave scattering properties is a soft disk of radius a,

$$V(r) \quad = \quad V_0 \Theta(R - a). \tag{3.50}$$

We are particularly interested in the case $V_0 < 0$, corresponding to an attractive disk.

The s wave phase shift δ_0 for the soft disk potential is determined by continuity of the logarithmic derivative of the wavefunction at $r = a$:

$$\tan \delta_0 = \frac{qJ_0(ka)J_1(qa) - kJ_1(ka)J_0(qa)}{qY_0(ka)J_1(qa) - kY_1(ka)J_0(qa)} \tag{3.51}$$

where

$$q \equiv \sqrt{2(E - V_0)}$$

is the wavenumber inside the disk.

Having calculated the s wave phase shift, it is straightforward to confirm that we can simulate the s wave scattering from a soft attractive disk with a t matrix

$$s(k) = \frac{-2 \tan \delta_0}{1 - i \tan \delta_0}. \tag{3.52}$$

The negative energy poles of the t matrix (A.0.6) occur at

$$qK_0(\kappa a)J_1(qa) = \kappa K_1(\kappa a)J_0(qa) \tag{3.53}$$

where $\kappa \equiv \sqrt{-2E}$. Eq. (A.0.7) can easily be shown to be the characteristic equation for bound states of the 2D cylindrical well.

Band Structure for Conducting States We used the forms in (3.49) and (A.0.6) to simulate three potentials: A potential with a generic bound state at $\kappa = 5$, a soft disk with a single bound state at $\kappa \approx 1.38$, and a soft disk with two bound states at $\kappa \approx 1.38$ and $\kappa = 4.02$. We discussed in 3.4.2 how conducting states of the array correspond to poles of $\tilde{s}(\vec{k})$, where the wavevector $\vec{k}$ has the form

$$\vec{k} = i\kappa_x \hat{x} + k_y y.$$

To find the conducting states, $\tilde{s}(k)$ was numerically evaluated on a 2D grid in order to search for poles. Our results, and the manifold of poles in $\vec{k}$ space, are indicated in Fig. 3.6(a, c, e) for each of the three potentials. In each panel, the solid black curves correspond to the manifolds of conducting states for the array. The dashed red curves, for comparison, are the contours

$$-\kappa_x^2 + k_y^2 = -\kappa^2,$$

corresponding to the bound state energies of a single scatterer. A more traditional view of the band structure for each potential is presented in Fig. 3.6(b, d, f), where the energies of the conducting states versus k_y have been plotted.

For the generic bound state, as indicated in Fig. 3.6(a, b), we are always in the tight binding limit. The renormalized t matrix $\tilde{s}(k)$ has poles exactly where, and only where $s(k)$ does–the array binds states at the binding energy of the scatterer. We are not able to create bound states in the continuum, for $E > 0$. The results are more interesting in the two arrays of physical potentials, with finite scattering lengths. In these examples, the array deforms the bound states of a single scatterer. In both cases we see in Fig. 3.6(d, f) that bound states are embedded in the continuum at $E > 0$, and can in principle be accessed with a propagating incident wave 3.6. These poles are the only poles of the infinite array, but are also are a subset of the poles of the array of any repeating unit cell of scatterers. Fig. 3.7 illustrates a representative bound state.

3.6 Arrays of Atoms as Waveguides

We discuss, in this section, how a wall of atoms might be used to guide waves. By guiding, we mean that if an incident beam is focused on some part of the grating, the scattered wave propagates along the grating for a long distance. In Sections 3.5.2 and 3.4, we discussed the existence of states that are quasibound or bound along the infinite array. These states, as such, are not an example of transport; being translationally invariant along the array, they can only be accessed by initial conditions that are already translationally invariant, such as plane waves. Any actual application of the phenomena discussed in this chapter thus requires that the array have a symmetry breaking point where an incident wave can be injected. In particular, in order for a localized beam aimed at the array to conduct, the array must have a defect or an end. The asymmetry will of course affect the properties of the grating, e.g. diffraction, impedance, etc. While we can use our results on the infinite array as a basis for studies of guiding in related systems, the infinite array itself is not a waveguide.

3.6.1 Guiding by a Semiinfinite Array

Consider an incident beam

$$\phi(\vec{r}) = \frac{1}{2\pi} \int_{-\pi/2+\beta}^{\pi/2+\beta} g(\theta_k - \beta) e^{i\vec{k}(\theta_k)\cdot\vec{r}} d\theta_k, \tag{3.54}$$

where $g(\theta_k) = e^{-(\theta_k/w)^2}$. Eq. (3.54) represents a beam incident from the right, focused on the scatterer at $\vec{r} = 0$, and rotated by an angle β from the positive x axis. The incident beam (3.54) with $\beta = 0$ (normal incidence) is shown in

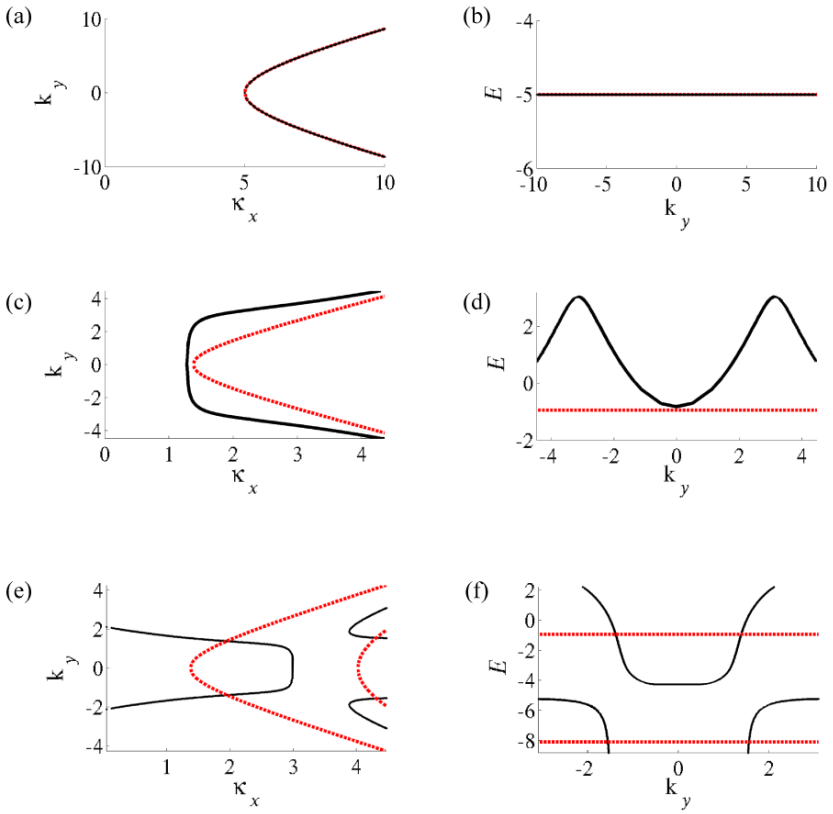

Figure 3.6: (a,c,e) show the curves along which $\tilde{s}(i\kappa_x, k_y)$ has poles (the symmetry across $k_y = 0$ is due to reflection symmetry of the array along $y = 0$). These curves correspond to manifolds of states bound in the x direction, and propagating along the array. The red curves, for comparison, are contours of wavevectors corresponding to bound state energy of a single scatterer. (b,d,f) show the band structure (E vs. k_y) for the conducting states. Panels (a,b) are for the t matrix (3.49) with $\kappa = 5$: The conducting states are trivial tight binding states at the single scatterer binding energy. with wavevectors along the contour $-\kappa_x^2 + k_y^2 = 5^2$. (c,d) For a soft disk with $V_0 = -10, a = 0.2$, a single bound state exists at $\kappa \approx 1.38$. This state is perturbed in the array. (e,f) Increasing the disk radius to $a = 1.0$, a second bound state appears at $\kappa \approx 4.02$. Both states are perturbed in the array. In (b-f) the bound states can be shifted to $E > 0$.

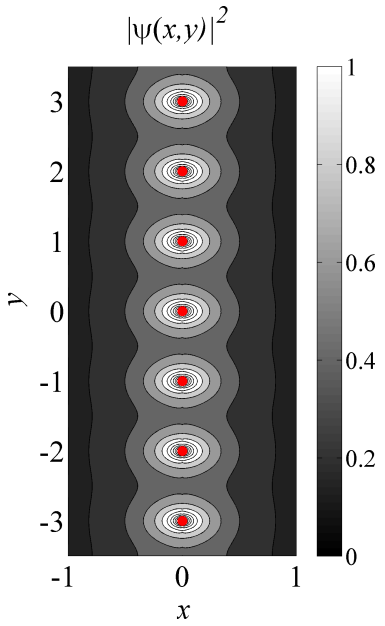

Figure 3.7: Contour plot of a conducting state at positive energy: The bound state corresponds to the wavevector $\vec{k} = (i, 1.665)$ in Fig. 3.6(e-f).

Fig. 3.8(a). As $w \to 0$, $\phi(\vec{r})$ approaches a plane wave, and for $w \to \infty$, $\phi(\vec{r})$ becomes a spherical wave, and its form is related to the Fourier transform of the spherical wave $J_0(kr)$. We are interested in intermediate values of w, for which (3.54) represents a focused beam.

Using our results for the infinite array as a guide, we take a purely numerical approach to the study of guiding in finite and semiinfinite arrays, as these systems are difficult to treat analytically. Analytical studies (e.g. [47], [34]) typically conclude that scattering from the semiinfinite array reproduces certain major features of the infinite array: Resonances, diffraction, etc. The main difference is that in the semiinfinite case, a spherical wave emanates from the end of the array. Most studies of semiinfinite arrays begin with the infinite solution, and derive this spherical edge wave as a correction term.

We demonstrate guiding numerically in Fig. 3.8. The scatterers are closely spaced, and the focused beam is aimed at the end of the array. In Fig. 3.8(c), a guided state clearly propagates along the array. The guiding occurs at low energies, near bound states of the infinite array. Guiding does not occur for repulsive scatterers, confirming that the coupling is to the true bound states of the array rather than the quasibound states.

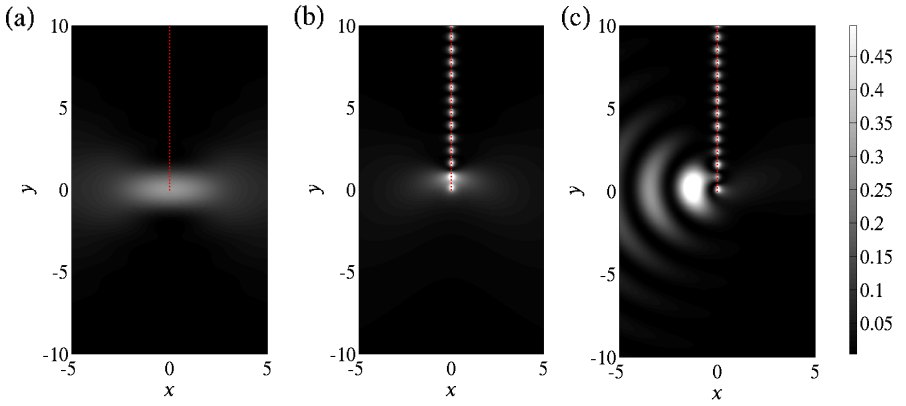

Figure 3.8: Guiding of a focused beam with $k = 0.5\pi$, $d = 0.1$. The scatterers are indicated by red dots. These plots show the probability densities of (a) the incident beam, focused on the end of the array (b) The scattered wave, which is guided along the array, and (c) the full scattered wavefunction (incident plus scattered). The individual scatterers are attractive wells with $V_0 = -10$ and radius $a = 0.2$, the same form used in Fig. 3.6(c)-(d). The spherical edge wave is clearly visible in (c).

The guiding is robust and extends to gently curved and finite walls as well, as we demonstrate in Fig. 3.9, where a beam focused on one end of a curved wall emerges at the other end. The scatterers are effectively behaving like a light pipe for a matter wave. If the wall is curved sharply relative to the wavelength of the incident beam, amplitude leaks out as adiabaticity breaks down.

In this section, we have demonstrated via numerical simulations that the $E > 0$ conducting states of the array can be exploited to guide waves along a semiinfinite wall of attractive, closely spaced scatterers. The physical explanation is that a semiinfinite wall of attractive potentials behaves like a trough, and furthermore that because the trough has an end, it is possible to couple into conducting states via injecting a beam into the end.

3.7 Conclusions and Future Directions

In this chapter, we have examined scattering from, and guiding by, quasi-1D periodic gratings of scatterers embedded in 2D. This system is an unusual one due to the coexistence of scattering phenomena, such as transmission, reflection, and resonance, with features typical to periodic systems: Band structure, diffraction and conduction along the array. Our motivation for examining this

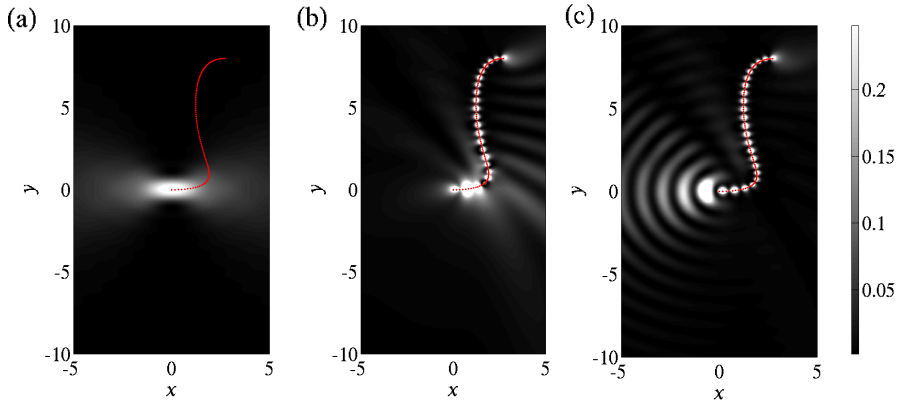

Figure 3.9: Guiding of a focused beam along a finite wall; $k = 3\pi$. The scatterers are the same attractive disks as in Fig. 3.8. These plots show the probability densities of (a) the incident beam, (b) the scattered wave, and (c) the full scattered wavefunction (incident plus scattered). In (b), amplitude visibly leaks away near the sharp bend near $y = 0$, as a consequence of nonadiabaticity.

system is that the system can be built, modeled, and applied: (1) Arranging individual atoms on substrates, often in patterns far more intricate than gratings, has become an established experimental technique [27–29, 50] (2) The standing wave patterns in these systems have been very successfully modeled by multiple scattering theories, such as we have applied here [30–32] and (3) A grating of particles which possess bound states can potentially serve as a waveguide for other particles.

We have, in this chapter, developed a multiple scattering theory (related to the KKR method) for quasi-1D gratings of s wave scatterers, embedded in 2D. The central physics is Bloch's theorem: We can obtain the full scattered wavefunction from the solution for a single unit cell, by replacing the t matrix of an individual scatterer with its renormalized version, and the free space Green's function with an effective Green's function. We have used the result to discuss some general effects, such as resonances, quasibound states, and bound states, each of which we have examined in detail for the simplest grating: A single chain of atoms. Finally, we have demonstrated numerically that bound states of the semiinfinite or finite array can be used to guide waves along straight or curved walls.

This work can be extended in a number of directions. We have chosen to embed our system in 2D because 2D is the relevant dimensionality for electrons in surface states scattering from atoms adsorbed on a metallic surface. With

a change in the free space Green's function, one could, however, revise the entire theory to treat a quasi-1D array embedded in 3D, such as might be relevant if the scatterers were atoms confined to an optical lattice. The physics of renormalization and interference in a 3D system would be very similar, and presumably near identical guiding effects would arise. Among the reasons that we have taken a multiple scattering approach to the system is that it can be generalized to the introduction of impurities or defects into the array. We have discussed how symmetry breaking is required for guiding to occur. Introducing an impurity or defect in an infinite array is one way of breaking symmetry; the impurity behaving as an antenna which brings an incident wave into the conducting state. The problem of impurities in the array is also interesting from a theoretical point of view, in the sense that the array with an impurity becomes a scattering system in the conducting mode, yielding, in essence, a scattering theory within a scattering theory. Furthermore, Foldy's method has recently been extended to include Rashba spin-orbit coupling [51], and it may be possible to modify the results of this chapter to examine spintronic versions of guiding.

Chapter 4

Further Applications of t Matrices

In this chapter we present analytic solutions for several seemingly disparate systems, which can all be treated via renormalized t matrices. We begin by examining the problem of two particles interacting on the surface of a tube. We then show how the renormalized t matrix formalism can be extended to treat a single two-level atom in confinement. We continue to study the problem of scattering from a double wall of atoms, and to examine scattering from a circle of atoms. We then propose a formalism for going beyond the s wave limit, and including the scattering of higher partial waves into some of the periodic systems we have described here.

4.1 Particles Interacting on a Tube

In this section, we consider the problem of low-energy scattering of two moving atoms confined to the surface of a tube. We model the interaction via a zero range interaction along the cylinder surface. We reduce the problem in the relative coordinate to that of one scatterer in a hard or periodic 2D wire, depending on the parity of the states.

4.1.1 Introduction

Consider two particles interacting on the surface of a cylinder. This problem is of interest for two reasons: The first is that it is a simple example of interacting particles in a confined geometry, and the second is that it is a simple model for

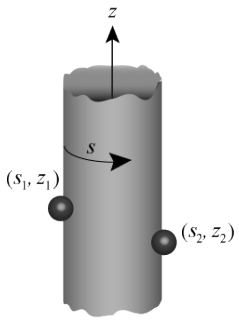

Figure 4.1: Two particles confined on the surface of a nanotube. The coordinates of the i^{th} particle are (s_i, z_i).

the physics of atoms or molecules moving just outside nanotubes. In particular, for molecules coating the inner surface of nanotubes having a radius of approximately $6-9$ Angstroms, the nanotube is well approximated as an infinitely long tube of radius R [52].

Suppose two interacting particles are free to move on the tube surface. Define the coordinates of the i^{th} particle on the cylinder as $\vec{r}_i = (s_i, z_i)$ as in Fig. 4.1. For the moment, we shall consider an interaction along the surface of the nanotube, generated by screening effects for example. The interaction potential would be along the tube's geodesic:

$$V(\vec{r}) = \sqrt{(s_2 - s_1)^2 + (z_2 - z_1)^2}.$$

Schrodinger's equation for the two scatterers, with periodic boundary conditions, is

$$\left[-\frac{\hbar^2}{2m}\left(\nabla_1^2 + \nabla_2^2\right) + V(\vec{r})\right]\Psi(s_1, z_1, s_2, z_2) = E\Psi(s_1, z_1, s_2, z_2) \quad (4.1)$$

$$\Psi(s_1 + 2\pi R, z_1, s_2, z_2) = \Psi(s_1, z_1, s_2, z_2) \quad (4.2)$$

$$\Psi(s_1, z_1, s_2 + 2\pi R, z_2) = \Psi(s_1, z_1, s_2, z_2) \quad (4.3)$$

In the absence of the waveguide boundary conditions (4.2-4.3), we would separate (4.1) into center of mass and relative coordinates. This problem (two bodies plus a potential) belongs to a class of problems called a restricted two body problem; such problems are not generally analytically soluble. However, as shown in [53], this problem happens to be nearly separable. We show that,

in the limit of s wave scattering, we can use this near separability to map the problem onto two sub-problems, each of which is closely related to the quantum wire discussed in Chapter 2. We find analytic solutions to these sub-problems by methods similar to those in Chapter 2.

4.1.2 Separation of Variables

As in [53], we define "relative" and "center of mass" coordinates

$$\begin{aligned} \vec{r} &= \vec{r}_2 - \vec{r}_1 \\ \vec{R} &= \frac{1}{2}\left(\vec{r}_1 + \vec{r}_2\right). \end{aligned}$$

As in the free space case, Schrodinger's equation (4.1) separates:

$$\left[-\frac{\hbar^2}{2M}\nabla^2_{\vec{R}} - \frac{\hbar^2}{2\mu}\nabla^2_{\vec{r}} + V(\vec{r})\right]\Psi(\vec{R},\vec{r};E) = E\Psi(\vec{R},\vec{r};E) \tag{4.4}$$

where we define the total mass $M = 2m$ and the reduced mass $\mu = m/2$.

We must also transform the boundary conditions (4.2, 4.3) into the new coordinate system. The transformed boundary conditions are

$$\begin{aligned} \Psi(s,S,z,Z) &= \Psi(s - 2\pi R, S + \pi R, z, Z) \\ &= \Psi(s + 2\pi R, S + \pi R, z, Z). \end{aligned}$$

Suppose our wavefunction consists of a superposition of terms of the form

$$\Psi(\vec{r},\vec{R}) = \chi(\vec{R})\psi(\vec{r}). \tag{4.5}$$

The product wavefunctions (4.5) satisfy separate Schrodinger equations

$$\begin{aligned} -\frac{\hbar^2}{2M}\nabla^2_{\vec{R}}\chi(\vec{R};E_{cm}) &= E_{cm}\chi(\vec{R};E_{cm}) \\ -\frac{\hbar^2}{2\mu}\nabla^2_{\vec{r}}\psi(\vec{r};E_r) + V(\vec{r}) &= E_r\psi(\vec{r};E_r) \end{aligned}$$

where

$$E_{cm} + E_r = E.$$

The product wavefunctions now have boundary conditions

$$\chi(S + \pi R, Z) = \pm\chi(S, Z) \tag{4.6}$$
$$\psi(s + 2\pi R, z) = \pm\psi(s + 2\pi R, z) \tag{4.7}$$

where the plus and minus signs are correlated–which is the difference from free space. If the problem were truly separable, any χ multiplied by any ψ would give a solution. In this case the solutions are quasiseparable, and χ and ψ must have common parity. Note that this separation fails for other very similar problems, such as the case of two interacting particles in a hard wire. We henceforth attach a superscript denoting the parity of each solution, so that $\chi^{\pm}(S, Z)$ and $\psi^{\pm}(s, z)$ are the center of mass and relative wavefunctions which satisfy the appropriate boundary conditions in (4.6, 4.7).

4.1.3 Incident Wave

We now wish to find scattering solutions to (4.4). Suppose the incoming wavefunction is a plane wave

$$\begin{aligned}\Phi(\vec{r}_1, \vec{r}_2) &= e^{i\vec{k}_1\cdot\vec{r}_1} e^{i\vec{k}_2\cdot\vec{r}_2} \\ &= \xi(\vec{R})\phi(\vec{r})\end{aligned} \tag{4.8}$$

where $\xi(\vec{R}) = e^{i\vec{K}\cdot\vec{R}}$, $\phi(\vec{r}) = e^{i\vec{k}\cdot\vec{r}}$, and $\vec{K} = \vec{k}_1 + \vec{k}_2$, $\vec{k} = \frac{1}{2}\left(\vec{k}_2 - \vec{k}_1\right)$ are the relative and center of mass wavevectors. The incident wave must satisfy the boundary conditions

$$\xi(S + \pi R, Z) = \pm\xi(S, Z) \tag{4.9}$$
$$\phi(s + 2\pi R, z) = \pm\phi(s + 2\pi R, z) \tag{4.10}$$

of the waveguide. These boundary conditions lead to constraints on the values of K_S and k_s:

$$\begin{aligned}K_S^{(n)} &= \frac{n}{R} \\ k_s^{(p)} &= \frac{p}{2R}\end{aligned}$$

where n or p are either both even, or both odd. The other two radial quantum numbers, K_Z and k_z, are not quantized: The set of all quantum numbers is

constrained by

$$\frac{\hbar^2}{2}\left(\frac{K^2}{M}+\frac{k^2}{\mu}\right)=E.$$

4.1.4 Center of Mass Wavefunction

The center of mass wavefunction satisfies the following relation for a free particle with periodic or antiperiodic boundary conditions:

$$\begin{aligned} -\frac{\hbar^2}{2M}\nabla^2_{\vec{R}}\chi^{\pm}(\vec{R};E_{cm}) &= E_{cm}\chi^{\pm}(\vec{R};E_{cm}) \quad (4.11)\\ \chi^{\pm}(S+\pi R,Z) &= \pm\chi^{\pm}(S,Z). \quad (4.12)\end{aligned}$$

Since (4.11) corresponds to free propagation, the scattering solution is simply the incoming center of mass wavefunction given in (4.8):

$$\chi^{\pm}_n(\vec{R};E_{cm})=e^{inS/R}e^{iK_Z^{(n)}Z},\ n \text{ even (odd)}$$

where

$$\frac{\hbar^2}{2M}\left[\left(\frac{n}{R}\right)^2+\left(K_z^{(n)}\right)^2\right]=E_{cm}^{(n)}.$$

While E_{cm} is a continuous parameter, for a given E_{cm}, K_S and K_Z are quantized.

4.1.5 Relative Wavefunction

The relative wavefunction satisfies the equation

$$\begin{aligned}\left[-\frac{\hbar^2}{2\mu}\nabla^2_{\vec{r}}+V(\vec{r})\right]\psi^{\pm}(\vec{r};E_r) &= E_r\psi^{\pm}(\vec{r};E_r)\\ \psi^{\pm}(s+2\pi R,z) &= \pm\psi^{\pm}(s,z)\end{aligned}$$

We have again denoted the parity with a superscript. Suppose we represent the interaction potential $V(\vec{r})=V(s,z)$ between the two particles as s wave scattering. In this approximation, we can shift to the T matrix formalism where

$$VG\psi=T\phi$$

and

$$t=s(k)\left|\vec{0}\right\rangle\left\langle\vec{0}\right|$$

represents the scatterer. The problem thus maps onto that of a scatterer centered in a hard or periodic strip waveguide of width $2\pi R$.

Applying the results of [54], the solution to this problem is

$$\psi^{\pm}(\vec{r}) = \phi(\vec{r}) + \tilde{s}^{\pm}(\vec{k})G^{\pm}(\vec{r};\vec{k})\phi(\vec{0})$$

where $\phi(\vec{r})$ is an incoming wavefunction and $\tilde{s}^{\pm}$ is an effective t matrix describing the interaction. The forms of $G^{\pm}(\vec{r})$ and $\tilde{s}^{\pm}(\vec{k})$ are

$$G^{+}(\vec{r};\vec{k}) = \sum_{n=-\infty}^{\infty} G_0(\vec{r}, 2\pi nR\hat{y}) \tag{4.13}$$

$$G^{-}(\vec{r};\vec{k}) = \sum_{n=-\infty}^{\infty} (-1)^n G_0(\vec{r}, 2\pi nR\hat{y}) \tag{4.14}$$

$$\tilde{s}^{+}(\vec{k}) = \sum_{\substack{n=-\infty \\ n\neq 0}}^{\infty} G_0(\vec{r}, 2\pi nR\hat{y})$$

$$\tilde{s}^{-}(\vec{k}) = \sum_{\substack{n=-\infty \\ n\neq 0}}^{\infty} (-1)^n G_0(\vec{r}, 2\pi nR\hat{y})$$

We have previously shown that

$$\begin{aligned} G(\vec{r}) &= \sum_{n=-\infty}^{\infty} G_0(k\,|\vec{r} - 2\pi nR\hat{y}|)e^{ik_s^{(0)}\times 2\pi nR} \\ &= \frac{i}{2\pi R}\sum_{q=-\infty}^{\infty} \frac{1}{k_z^{(q)}} e^{ik_z^{(q)}|z|}e^{ik_s^{(q)}s} \end{aligned} \tag{4.15}$$

where

$$\begin{aligned} k_s^{(q)} &= k_s^{(0)} + \frac{q}{R} \\ k_z^{(q)} &= \sqrt{k^2 - \left(k_s^{(q)}\right)^2}. \end{aligned}$$

We see that with $k_s^{(0)} = 0$, (4.15) becomes (4.13), whereas with $k_s^{(0)} = \frac{1}{2R}$, (4.15) becomes (4.14).

The result is that the wavevectors are characterized by parity:

$$\begin{aligned} k_s^{(q,\pm)} &= \frac{q}{2R} \\ k_z^{(q,\pm)} &= \sqrt{k^2 - \left(\frac{q}{2R}\right)^2} \end{aligned}$$

where $\vec{k}^{(q,\pm)}$ corresponds to q even or odd respectively.

We thus have a plane wave expansion for the scattered wavefunction in the relative coordinate. If the initial relative wavefunction is

$$\phi(\vec{r}) = \frac{1}{\sqrt{k_z^{(p)}}} e^{ik_z^{(0)}z} e^{i\frac{p}{2R}}, \tag{4.16}$$

with p even, the scattered relative wavefunction is

$$\psi^{(+)}(\vec{r};\vec{k}) = \frac{1}{\sqrt{k_z^{(p)}}} e^{ik_z^{(0)}z} e^{i\frac{p}{2R}} - \frac{i\tilde{s}_+}{2\pi R} \sum_{q \text{ even}} \frac{1}{k_z^{(q)}} e^{ik_z^{(q)}|z|} e^{ik_s^{(q)}s}.$$

If the initial wavefunction (4.16) has p odd, it scatters into the odd parity modes

$$\psi^{(-)}(\vec{r};\vec{k}) = \frac{1}{\sqrt{k_z^{(p)}}} e^{ik_z^{(0)}z} e^{i\frac{p}{2R}} - \frac{i\tilde{s}_-}{2\pi R} \sum_{q \text{ odd}} \frac{1}{k_z^{(q)}} e^{ik_z^{(q)}|z|} e^{ik_s^{(q)}s}.$$

The parity of the relative wavefunction is conserved by the scattering.

4.1.6 The S Matrix

A first step to understanding the many-body system is to write down the **S** matrix for the two body collision.

If the energy of the system is fixed, the initial state is indexed by the total energy E as well as the center of mass and relative radial quantum numbers, n and p. Since we are considering only elastic scattering processes, E is fixed in a collision, and the entries of the **S** matrix are indexed by $S_{nm,pq}$. An incident wavefunction

$$\Phi(\vec{r},\vec{R}) = \frac{1}{\sqrt{K_z^{(n)} k_z^{(p)}}} e^{iK_z^{(n)}z} e^{inS/R} e^{ik_z^{(p)}z} e^{ips/R}$$

scatters into the following state:

$$\Psi(\vec{r},\vec{R}) = \frac{1}{\sqrt{K_z^{(n)}}} e^{iK_z^{(n)}z} e^{inS/R} \times \left[e^{ik_z^{(p)}z} e^{ips/R} - \frac{i\tilde{s}_\pm}{2\pi R} \sum_{q\,\text{even/odd}} \frac{1}{\sqrt{k_z^{(p)}k_z^{(q)}}} \frac{1}{\sqrt{k_z^{(q)}}} e^{ik_z^{(q)}|z|} e^{iqs/2R} \right]. \tag{4.17}$$

The $\pm$ indices as well as the parity of q over which the sum runs depend on the parity of p. Defining the parity function $\Pi(p,q) = 1$ if (p,q) are of the equal parity, and zero otherwise, we can read off reflection and transmission coefficients from (4.17):

$$R_{nm,pq} = \begin{cases} \delta_{nm} \times \left(-\frac{i\tilde{s}_\pm}{2\pi R}\right) \frac{1}{\sqrt{k_z^{(p)}k_z^{(q)}}} & \Pi(p,q) = 1 \\ 0 & \Pi(p,q) = 0 \end{cases}$$

$$T_{nm,pq} = \delta_{nm}\delta_{pq} + R_{nm,pq}$$

The scattering conserves parity, and the **S** matrix can be made block diagonal.

We have, in this section, solved for the scattering of two particles interacting via s wave scattering, with an arbitrary potential, along the surface of a tube. We have characterized the solutions by parity, and derived an analytic expression for the scattering matrix for this system. This result has two potential uses: One could use it as a simple model for the problem of particles on nanotubes, which is typically solved using an exact potential rather than a t matrix representation (see e.g. [52]) or alternately one could use this **S** matrix as a launching point for a general study of collisional decoherence in confined dilute many-body systems, assuming that only binary collisions are relevant. While the model of a tube is not a particularly realistic model for an atom waveguide (although one could imagine using counterpropagating beams to generate a cylindrical optical trap) many features of the solution are probably general to different types of confinement. The problem of two particles with a point s wave interaction on a tube is extremely unusual in that it can be completely solved analytically, whereas the equally reductionist problem of two particles in a hard-walled wire cannot (that problem does, however, reduce to scattering from a delta wire stretched across a box). We thus close this section with an **S** matrix for this system, and some suggestions for its potential use.

4.2 Two Level Atoms in a Hard Walled Guide

In this section we present a calculation which shows that the renormalized t matrix formalism can be extended to treat scattering from a multilevel impurity confined to a hard-walled guide. We stress that this calculation is a very preliminary one, as we have not incorporated dissipation. Dissipation effects could perhaps be included phenomenologically by taking a master equation approach to the system, using the scattering eigenstates we have calculated here.

4.2.1 Two Level Scattering in Free Space, No Dissipation

Consider the problem of a two level particle scattering from a fixed target in a waveguide (or identically, a stuctureless particle scattering from a two level particle). Denote the particle states as $|1\rangle, |2\rangle$ such that the energy difference is $E_2 - E_1 = \Delta$. The incident wavefunction is then

$$\phi = \phi^{(1)}(\vec{r}; E) \otimes |1\rangle + \phi^{(2)}(\vec{r}; E) \otimes |2\rangle .$$

When this beam scatters from an impurity, the possible transitions of the particle's internal state are

$$\begin{aligned} |E;1\rangle &\leftrightarrow |E;1\rangle \\ |E;1\rangle &\leftrightarrow |E-\Delta;2\rangle \\ |E;2\rangle &\leftrightarrow |E+\Delta;1\rangle \\ |E;2\rangle &\leftrightarrow |E;2\rangle \end{aligned}$$

Our incident state is not an eigenstate of the total energy of the system, but a combination of eigenstates with total energies E and $E + \Delta$. The first two states are degenerate with total energy E, and the second two are degenerate with energy $E + \Delta$.

We would like to find the scattering eigenstates of the system with total energy E. We characterize a transition from level i to level j via the t matrix $s_{ij}(E_1, E_2)$, where E_1 and E_2 are the initial and final energies of the incident particle. These t matrices determine the characteristics of the collision.

Define the free space Green's function

$$G_0(\vec{r}, \vec{r}_0; E) = -\frac{i}{2} H_0(\sqrt{E}|\vec{r} - \vec{r}_0|)$$

where H_0 denotes the Hankel function of the first kind. In free space, we can set

up the problem of a two state particle scattering from a structureless particle at $\vec{r}_0$ as follows:

$$\begin{bmatrix} \psi^{(1)}(\vec{r};E) \\ \psi^{(2)}(\vec{r};E-\Delta) \end{bmatrix} = \begin{bmatrix} \phi^{(1)}(\vec{r};E) \\ \phi^{(2)}(\vec{r};E-\Delta) \end{bmatrix} + \mathbf{G}_0(\vec{r},\vec{r}_0;E)\mathbf{s}(E) \begin{bmatrix} \phi^{(1)}(\vec{r}_0;E) \\ \phi^{(2)}(\vec{r}_0;E-\Delta) \end{bmatrix}$$

where

$$\begin{aligned} \mathbf{G}_0(\vec{r},\vec{r}_0;E)\mathbf{s}(E) &\equiv \begin{bmatrix} G_0(\vec{r},\vec{r}_0;E) & 0 \\ 0 & G_0(\vec{r},\vec{r}_0;E-\Delta) \end{bmatrix} \\ &\times \begin{bmatrix} s_{11}(E,E) & s_{12}(E,E-\Delta) \\ s_{21}(E-\Delta,E) & s_{22}(E-\Delta,E-\Delta) \end{bmatrix}. \end{aligned}$$

We can choose the elastic scattering t matrix elements to have the form of hard spheres, while the inelastic elements include Breit-Wigner resonances at the level transition frequency Δ, as the maximal inelastic cross section will occur at Δ.

4.2.2 Scattering in a Waveguide, Still No Dissipation

Confinement changes the scattering properties of the impurity; we use the method of images to calculate the renormalized t matrices in the wire, in terms of their free space values.

Using Foldy's method, we can convert the confined problem to a problem of multiple scattering from an infinite array of images at positions $\{\vec{r}_i\}$:

$$\begin{bmatrix} \psi^{(1)}(\vec{r};E) \\ \psi^{(2)}(\vec{r};E-\Delta) \end{bmatrix} = \begin{bmatrix} \phi^{(1)}(\vec{r};E) \\ 0 \end{bmatrix} + \sum_{i=-\infty}^{\infty} \mathbf{G}_0(\vec{r},\vec{r}_i;E)\mathbf{s}(E) \begin{bmatrix} \psi_i^{(1)}(\vec{r}_i;E) \\ \psi_i^{(2)}(\vec{r}_i;E-\Delta) \end{bmatrix}.$$

where

$$\begin{bmatrix} \psi_i^{(1)}(\vec{r}_i;E) \\ \psi_i^{(2)}(\vec{r}_i;E-\Delta) \end{bmatrix} = \begin{bmatrix} \phi^{(1)}(\vec{r}_i;E) \\ 0 \end{bmatrix} + \sum_{j\neq i} \mathbf{G}_0(\vec{r}_i,\vec{r}_j;E)\mathbf{s}(E) \begin{bmatrix} \psi_j^{(1)}(\vec{r}_j;E) \\ \psi_j^{(2)}(\vec{r}_j;E-\Delta) \end{bmatrix}.$$

Define the function

$$\begin{aligned} G_R(E) &\equiv \lim_{\vec{r}\to\vec{r}_0} \left[G_W(\vec{r},\vec{r}_0;E) - G_0(\vec{r},\vec{r}_0;E) \right] \\ &= \sum_{\substack{j=-\infty \\ j\neq 0}}^{\infty} (-1)^j G_0(\vec{r}_0,\vec{r}_j;E) \end{aligned}$$

which we recognize from Chapter 2 as the regular part of the wire Green's function, evaluated at the scatterer.

The condition of hard walls implies that the wavefunction must satisfy

$$\begin{bmatrix} \psi_j^{(1)}(\vec{r}_j;E) \\ \psi_j^{(2)}(\vec{r}_j;E-\Delta) \end{bmatrix} = (-1)^j \begin{bmatrix} \psi_0^{(1)}(\vec{r}_0;E) \\ \psi_0^{(2)}(\vec{r}_0;E-\Delta) \end{bmatrix}$$

The equations then become

$$\begin{bmatrix} \psi_0^{(1)}(\vec{r}_0;E) \\ \psi_0^{(2)}(\vec{r}_0;E-\Delta) \end{bmatrix} = [\mathbf{I} - \mathbf{G_R}(E)\mathbf{s}(E)]^{-1} \begin{bmatrix} \phi^{(1)}(\vec{r}_0;E) \\ 0 \end{bmatrix}$$

where

$$\mathbf{G_R}(E) \equiv \begin{bmatrix} G_R(E) & 0 \\ 0 & G_R(E-\Delta) \end{bmatrix}.$$

These are simply four algebraic equations, in four unknowns. The full multiple scattering solution thus is the same in the wire, except with an *effective* incoming wavefunction where the components are mixed:

$$\begin{aligned} \begin{bmatrix} \psi^{(1)}(\vec{r};E) \\ \psi^{(2)}(\vec{r};E-\Delta) \end{bmatrix} &= \begin{bmatrix} \phi^{(1)}(\vec{r};E) \\ 0 \end{bmatrix} + \mathbf{G}_W(\vec{r},\vec{r}_0;E)\mathbf{s}(E) \\ &\quad \times \left\{ [\mathbf{I} - \mathbf{G_R}(E)\mathbf{s}(E)]^{-1} \begin{bmatrix} \phi^{(1)}(\vec{r}_0;E) \\ 0 \end{bmatrix} \right\}. \end{aligned}$$

We have here demonstrated that the renormalized t matrix approach can, in principle, be modified to treat to multistate systems. An accurate treatment of a two-level system, however, would have to (perhaps phenomenologically) incorporate radiative decay, our treatment here is a preliminary one.

4.3 Scattering from a Circle of Atoms

In this section we consider scattering of a spherical wave scattering from a circle of N atoms. We show that the solution is analytic, and also that far from the circle, the circle looks like a point scatterer–but not with N times the strength of a single scatterer, as one might expect; the difference is due to the usual multiple scattering effects.

4.3.1 Scattering in a Circle

Suppose we have a circle of N atoms, indexed by $n = 0, 1, 2, \ldots N-1$, with the n^{th} atom located at

$$\vec{r}_n = R(\cos\theta_n, \sin\theta_n)$$

where

$$\theta_n = \frac{2\pi n}{N}$$

(see Fig. 4.2).

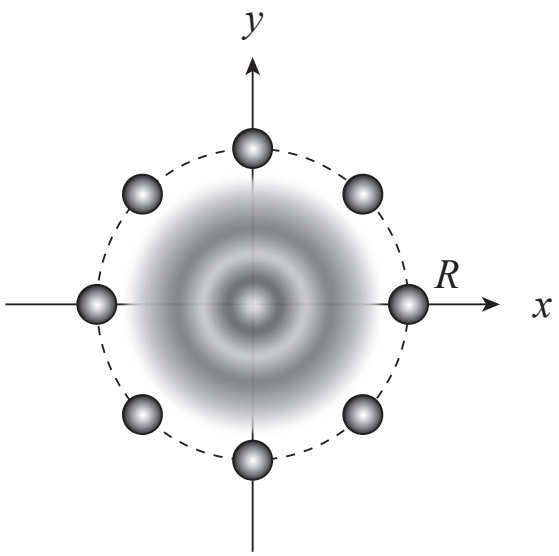

Figure 4.2: Spherical wave scattering from a circle of N atoms.

Suppose each atom has an energy dependent scattering length, represented by a t matrix $s(k)$. Further suppose a spherical wave $\phi(r)$ emanating from the center of the circle,

$$\phi(r) = -\frac{i}{2}H_0(kr).$$

The recursive Foldy-Lax equations for multiple scattering are

$$\psi(\vec{r}) = \phi(\vec{r}) + s(k) \sum_{n=0}^{N-1} G_0(\vec{r}, \vec{r}_n)\psi_n(\vec{r}_n) \tag{4.18}$$

$$\psi_n(\vec{r}_n) = \phi(R) + s(k) \sum_{n \neq m} G_0(\vec{r}_m, \vec{r}_n)\psi_m(\vec{r}_m) \tag{4.19}$$

By symmetry,

$$\psi_n(\vec{r}_n) = \psi_0(\vec{r}_0). \tag{4.20}$$

Combining (4.20) with (4.19) allows us to simplify the multiple scattering equations:

$$\begin{aligned} \psi_0(\vec{r}_0) &= \phi(\vec{r}_0) + s(k)\psi_0(\vec{r}_0) \sum_{n=1}^{N-1} G_0(\vec{r}_m, \vec{r}_0) \\ &= \frac{\phi(\vec{r}_0)}{1 - s(k) \sum_{n=1}^{N-1} G_0(\vec{r}_m, \vec{r}_0)}. \end{aligned} \tag{4.21}$$

Substituting, we can thus find the full scattered wavefunction,

$$\begin{aligned} \psi(\vec{r}) &= \phi(r) + \frac{s(k)\phi(R)}{1 - s(k) \sum_{n=1}^{N-1} G_0(\vec{r}_m, \vec{r}_0)} \sum_{n=0}^{N-1} G_0(\vec{r}, \vec{r}_n) \\ &= \phi(r) + \frac{s(k)\phi(R)}{1 + \frac{is}{2} \sum_{n=1}^{N-1} H_0\left(kR\sqrt{2\left(1 - \cos\frac{2n\pi}{N}\right)}\right)} \sum_{n=1}^{N} G_0(\vec{r}, \vec{r}_n) \\ &= \phi(r) + \tilde{s}(k)\phi(R) \sum_{n=1}^{N} G_0(\vec{r}, \vec{r}_n) \end{aligned} \tag{4.22}$$

where we have defined a renormalized scattering strength

$$\tilde{s}(k) = \frac{s(k)}{1 + \frac{is(k)}{2} \sum_{n=1}^{N-1} H_0\left(2kR \sin\frac{n\pi}{N}\right)}. \tag{4.23}$$

See Fig. 4.3. Note that in the limit of one scatterer ($N = 0, R = 0$) $\tilde{s}(k) = s(k)$, and the scattered wavefunction also has the correct form for a single scatterer. To simplify the sum in (4.23), we could use the identity

$$H_0\left(kR\sqrt{2(1 - \cos\theta)}\right) = J_0(kR)H_0(kR) + 2\sum_{l=1}^{\infty} J_l(kR)H_l(kR)\cos l\theta.$$

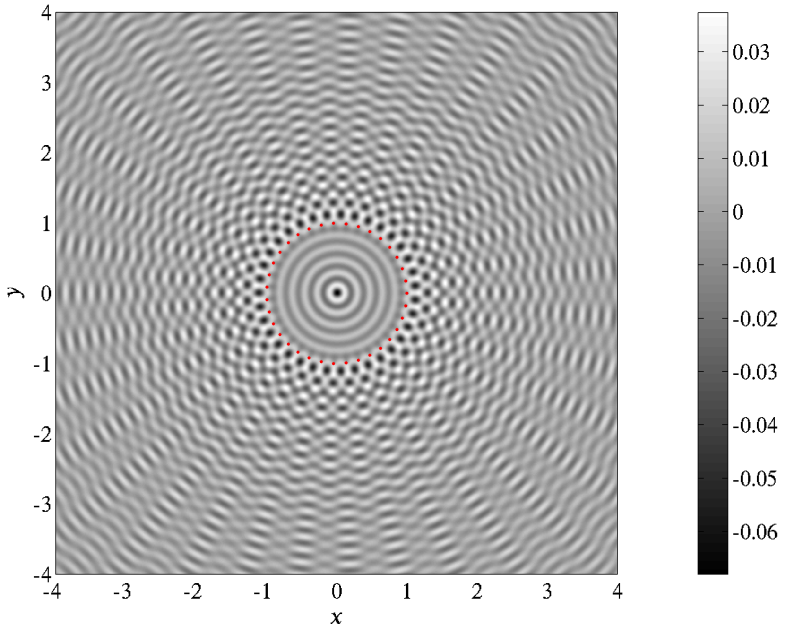

Figure 4.3: Real part of a spherical wave scattering from a circle of 35 scatterers (indicated in red). Incident wave has wavenumber $k = 36.1318$, halfway between resonances.

This identity, which is applied to the continuous circle in [48], yields

$$\sum_{n=1}^{N-1} H_0\left(kR\sqrt{2\left(1-\cos\frac{2n\pi}{N}\right)}\right) = (N-1)J_0(kR)H_0(kR) + 2\sum_{l=1}^{\infty} J_l(kR)H_l(kR)\sum_{n=1}^{N-1}\cos\frac{2ln\pi}{N}.$$

4.3.2 Transmission Properties of the Circle

To simplify the Lippmann Schwinger equation (4.22), we can now use the limiting form of the Hankel function,

$$\lim_{kr\to\infty} H_0(kr) = \sqrt{\frac{2}{\pi kr}}e^{i(kr-\frac{\pi}{4})}.$$

At radii far from the circle, $r \gg R$, we have

$$\begin{aligned}\psi(\vec{r}) &\approx -i\sqrt{\frac{1}{2\pi k}}\left[\frac{e^{i(kr-\frac{\pi}{4})}}{\sqrt{r}}\right. \\ &\left. +\tilde{s}\phi(R)e^{-i\pi/4}\sum_{n=1}^{N}\frac{e^{ik\sqrt{r^2+R^2-2rR\cos\left(\theta-\frac{2n\pi}{N}\right)}}}{\left[r^2+R^2-2rR\cos\left(\theta-\frac{2n\pi}{N}\right)\right]^{1/4}}\right].\end{aligned}$$

We can simplify the series expansion for $|\vec{r}-\vec{r}_n|$ that we have used for $\frac{R}{r} \ll 1$:

$$\begin{aligned}|\vec{r}-\vec{r}_n| &= r\sqrt{1+\left(\frac{R}{r}\right)^2-\frac{2R}{r}\cos\left(\theta-\frac{2n\pi}{N}\right)} \\ &\approx r\left[1-\frac{R}{r}\cos\left(\theta-\frac{2n\pi}{N}\right)\right]\end{aligned}$$

and

$$\sqrt{|\vec{r}-\vec{r}_n|} \approx \sqrt{r}\left[1-\frac{1}{2}\frac{R}{r}\cos\left(\theta-\frac{2n\pi}{N}\right)\right]$$

so that

$$\begin{aligned}\psi(\vec{r}) &\approx -i\sqrt{\frac{1}{2\pi}}\left\{\frac{e^{i(kr-\frac{\pi}{4})}}{\sqrt{kr}}\right. \\ &\left. +\tilde{s}\phi(R)e^{-i\pi/4}\sum_{n=1}^{N}\frac{e^{ikr\left[1-\frac{R}{r}\cos\left(\theta-\frac{2n\pi}{N}\right)\right]}}{\sqrt{kr}\left[1-\frac{1}{2}\frac{R}{r}\cos\left(\theta-\frac{2n\pi}{N}\right)\right]}\right\}.\end{aligned}$$

To calculate the transmission properties, we go to the limit $r/R \to \infty$, in which

$$\psi(\vec{r}) = -i\sqrt{\frac{1}{2\pi}}\left\{\frac{e^{i(kr-\pi/4)}}{\sqrt{kr}}+N\tilde{s}\phi(R)\frac{e^{i(kr-\pi/4)}}{\sqrt{kr}}\right\}. \tag{4.24}$$

For comparison, scattering from a free space point scatterer at the origin goes, at large r, as

$$\psi(\vec{r}) = \phi(\vec{r}) - is(k)\frac{e^{i(kr-\pi/4)}}{\sqrt{2kr}}\phi(0) \tag{4.25}$$

where the scatterer has t matrix $s(k)$. Comparing (4.24) with (4.25), we can see that the wavefunction scattered from the circle of scatterers behaves effectively like the wave scattered by a point scatterer at large radius. The effective scattering strength is $N\tilde{s}$ rather than simply Ns, which we might expect to be the

result if we did not include multiple scattering.

For a single point scatterer in free space, we can define an effective cross section

$$\sigma = \frac{1}{k} |s(k)|^2 .$$

The effective "cross section" of the circle of scatterers is thus

$$\sigma = \frac{1}{k} N^2 |\tilde{s}(k)|^2 .$$

4.3.3 Quantum Interference Effects on Transmission

We wish to measure the "leakiness" of the cavity. The incident radial probability flux is

$$\begin{aligned} \Phi_i &= \int_0^{2\pi} d\theta j_{r,inc} \\ &= 1 \end{aligned}$$

The flux transmitted out of the cavity is

$$\begin{aligned} \Phi_t &= 1 + 2N\mathrm{Re}\left(\tilde{s}\phi(R)\right) + N^2 |\tilde{s}\phi(R)|^2 \\ &\approx 1 + 2N\mathrm{Re}\left(\tilde{s}\phi(R)\right) + \frac{N^2 |\tilde{s}|^2}{kR} \end{aligned}$$

We find (Fig. 4.4) resonances in the reflection coefficient, roughly near the bound state energies of the closed circle (k_n defined by $J_0(k_n R) = 0$). These resonances have a finite width corresponding to the finite lifetime due to leakage between the scatterers. This width corresponds to the quality factor Q of the cavity.

4.4 Scattering from Double Walls

We present here the solution for scattering from a double wall, which is a particular case of the results in Chapter 3 that can be solved analytically. The double wall is a problem of interest in the context of billiards that can trap waves along their edges.

4.4.1 Solution for the Double Array

Consider a beam $\phi(\vec{r}) = e^{i\vec{k}\cdot\vec{r}}$ incident on a double wall of identical atoms at positions $\vec{r}_n = (-\frac{w}{2}, nd)$, $\vec{r}_m = (\frac{w}{2}, md)$. Each atom has an energy dependent t

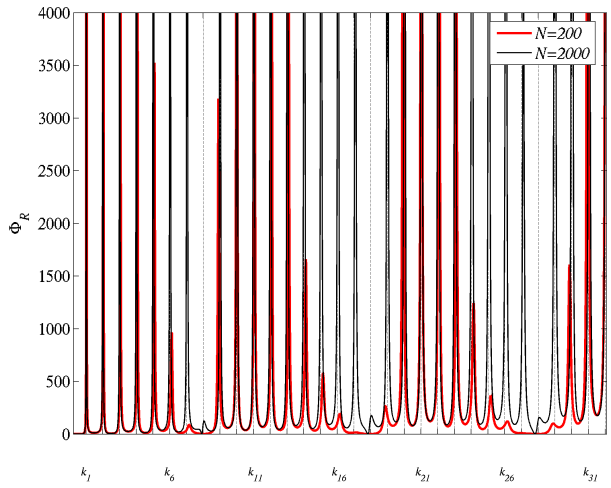

Figure 4.4: Flux trapped inside a circle of N atoms; $N = 200$ and $N = 2000$. The resonances are approximately (but not always exactly) at wavenumbers k_n such that $J_0(k_n R) = 0$, corresponding to bound states of the hard walled circle billiard (ticks and grid lines on the plot). Bringing the scatterers closer together increases the Q factor, and also moves the resonances closer to the billiard values. Note the difference at high energies.

matrix $s(k)$.

We apply Foldy's method, where the indices n, p run over the arrays at $x = \mp\frac{w}{2}$ respectively. The resulting Lippmann Schwinger equation is

$$\psi(\vec{r}) \quad = \quad \phi(\vec{r}) + s\sum_n G_0(\vec{r},\vec{r}_n)\psi_n(\vec{r}_n) + s\sum_p G_0(\vec{r},\vec{r}_p)\psi_p(\vec{r}_p) \qquad (4.26)$$

where

$$\begin{aligned}
\psi_n(\vec{r}_n) \quad &= \quad \phi(\vec{r}_n) + s\sum_{m\neq n} G_0\left(k\left|m-n\right|d\right)\psi_m(\vec{r}_m) \qquad (4.27)\\
&\quad\quad +s\sum_p G_0\left(k\sqrt{w^2+(p-n)^2\,d^2}\right)\psi_p(\vec{r}_p)\\
\psi_p(\vec{r}_p) \quad &= \quad \phi(\vec{r}_p) + s\sum_m G_0\left(k\sqrt{w^2+(m-p)^2\,d^2}\right)\psi_m(\vec{r}_m)\\
&\quad\quad +s\sum_{q\neq p} G_0\left(k\left|q-p\right|d\right)\psi_q(\vec{r}_q)
\end{aligned}$$

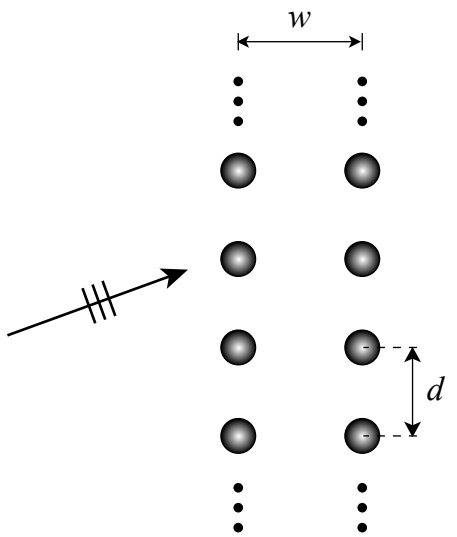

Figure 4.5: Scattering from a double line of atoms.

and

$$G_0(kr) \quad = \quad -\frac{i}{2}H_0(kr) \tag{4.28}$$

is the two-dimensional free space Green's function ($\hbar = m = 1$).

To make a long story short, we are able to find the solution simply by replacing the t matrix $s(k)$ with two renormalized t matrices:

$$\psi(\vec{r}) = \phi(\vec{r}) + \tilde{s}_L \sum_n G_0(\vec{r}, \vec{r}_n)\psi_n(\vec{r}_n) + \tilde{s}_R \sum_p G_0(\vec{r}, \vec{r}_p)\psi_p(\vec{r}_p)$$

where

$$\begin{aligned}
\tilde{s}_L &\equiv \frac{1}{2}s\left[\frac{1+e^{ik_x w}}{1-s(G_s+G_d)} + \frac{1-e^{ik_x w}}{1-s(G_s-G_d)}\right] \\
\tilde{s}_R &\equiv \frac{1}{2}s\left[\frac{1+e^{-ik_x w}}{1-s(G_s+G_d)} + \frac{1-e^{-ik_x w}}{1-s(G_s-G_d)}\right]
\end{aligned}$$

and we have defined two sums,

$$G_s \equiv \sum_{u\neq 0} G_0(kd\,|u|)e^{ik_y ud} \tag{4.29}$$

$$G_d \equiv \sum_{u} G_0\left(k\sqrt{w^2+u^2d^2}\right)e^{ik_y ud}. \tag{4.30}$$

to which we can apply Kummer's method to put in a nicer form.

4.4.2 Details

Consider first the wavelets $\psi_n(\vec{r}_n)$ representing the left hand side of the array. Iterating (4.27) to second order in s, we find

$$\begin{aligned}
\psi_n(\vec{r}_n) \quad = e^{ik_y nd}\times \quad & \Bigg[e^{-ik_x \frac{w}{2}} + se^{-ik_x \frac{w}{2}} \sum_{m\neq n} G_0\left(k\left|m-n\right|d\right) e^{ik_y md} \\
& + se^{ik_x \frac{w}{2}} \sum_{m} G_0\left(k\sqrt{w^2+\left(m-n\right)^2 d^2}\right) e^{ik_y md} \\
& \times s\sum_{p\neq m} G_0\left(k\left|p-m\right|d\right) e^{ik_y pd} \\
& + s^2 e^{ik_x \frac{w}{2}} \sum_{m\neq n} G_0\left(k\left|m-n\right|d\right) \\
& + se^{ik_x \frac{w}{2}} \sum_{m} G_0\left(k\sqrt{w^2+\left(m-n\right)^2 d^2}\right) e^{ik_y md} \\
& + s^2 e^{-ik_x \frac{w}{2}} \sum_{m\neq n} G_0\left(k\left|m-n\right|d\right) \\
& \times s\sum_{p\neq m} G_0\left(k\left|p-m\right|d\right) e^{ik_y pd} + s^2 e^{ik_x \frac{w}{2}} \sum_{m\neq n} G_0\left(k\left|m-n\right|d\right) \\
& \times \sum_{p} G_0\left(k\sqrt{w^2+\left(p-m\right)^2 d^2}\right) e^{ik_y pd} \\
& + s^2 e^{ik_x \frac{w}{2}} \sum_{m} G_0\left(k\sqrt{w^2+\left(m-n\right)^2 d^2}\right) \\
& \times \sum_{p\neq m} G_0\left(k\left|p-m\right|d\right) e^{ik_y pd} \\
& + s^2 e^{-ik_x \frac{w}{2}} \sum_{m} G_0\left(k\sqrt{w^2+\left(m-n\right)^2 d^2}\right) \\
& \times \sum_{p} G_0\left(k\sqrt{w^2+\left(p-m\right)^2 d^2}\right) e^{ik_y pd} \\
& + O(s^3)\Bigg]
\end{aligned}$$

As formidable as the above expression appears, its diagrammatic representation would be quite simple. Furthermore, upon re-indexing the sums, they

each collapse, so that the above reduces to

$$\begin{aligned}\psi_n(\vec{r}_n) &= e^{-ik_x\frac{w}{2}}e^{ik_y nd}\times[1+sG_s+se^{ik_x w}G_d \\ &\quad +s^2G_s^2+2s^2e^{ik_x w}G_sG_d+s^2G_d^2 \\ &\quad +O(s^3)]\end{aligned}$$

We see that this is simply a modified binomial series, where the terms with odd orders of G_d carry a relative phase of $e^{ik_x w}$. Simplifying,

$$\begin{aligned}\psi_n(\vec{r}_n) &= \phi(\vec{r}_n)\times\frac{1}{2}\sum_{n=0}^{\infty}s^n\left\{(G_s+G_d)^n+(G_s-G_d)^n\right. \\ &\quad \left.+e^{ik_x w}\times[(G_s+G_d)^n-(G_s-G_d)^n]\right\} \\ &= \phi(\vec{r}_n)\times\frac{1}{2}\left[\frac{1+e^{ik_x w}}{1-s(G_s+G_d)}+\frac{1-e^{ik_x w}}{1-s(G_s-G_d)}\right].\end{aligned}$$

By an identical argument,

$$\psi_m(\vec{r}_m) = \phi(\vec{r}_m)\times\frac{1}{2}\left[\frac{1+e^{-ik_x w}}{1-s(G_s+G_d)}+\frac{1-e^{-ik_x w}}{1-s(G_s-G_d)}\right].$$

4.5 Higher Partial Wave Scattering from an Impurity in a Quantum Wire[1]

4.5.1 Introduction

In Chapter 2, we had examined scattering from an s wave scatterer in a 2D wire. At energies relevant to electron imaging experiments, an AFM tip cannot be accurately modeled as an s wave scatterer. One way of modeling the tip is to build a "bump" out of many small s wave scatterers of variable scattering lengths. Although this method is one way to approach the problem, it is computationally expensive, particularly when the scatterer is confined in a waveguide. Furthermore, it is not amenable to analytic treatment. In this section, we generalize our multiple scattering formalism for the single scatterer in a wire to include higher partial waves. Our approach is based on the method presented in [55] for including higher partial waves in free space multiple scattering.

[1] This section was written in collaboration with J. D. Walls.

4.5.2 Including Higher Partial Waves in Free Space 2D Scattering

In this section we briefly review the free space formalism presented in [55], to which we refer the reader for a more thorough treatment. The notation in this chapter differs slightly from our notation in previous chapters, for consistency with [55]. Suppose a plane wave

$$\phi_m(\vec{r}) = e^{i\vec{k}(\theta_m)\cdot\vec{r}}$$

is incident on a scatterer in free space. We shall work in the t matrix formalism, and include all higher partial waves. Ref. [55] (Eq. 6.31) models 2D free space scattering, including all higher partial waves, with a scattered wavefunction of the form

$$\begin{aligned} \psi(\vec{r}) &= \phi(\vec{r}) + \frac{1}{2}\sum_{l=0}^{\infty} s^{(l)} H_l(k\,|\vec{r}-\vec{r}_n|)\cos l(\theta_n-\theta_m)\phi(\vec{r}_n) \qquad (4.31) \\ &= \phi(\vec{r}) + \frac{1}{2}\sum_{l=0}^{\infty} s^{(l)} H_l(k\,|\vec{r}-\vec{r}_n|) \qquad (4.32) \\ &\quad \times(\cos l\theta_n \cos l\theta_m + \sin l\theta_n \sin l\theta_m)\phi(\vec{r}_n) \end{aligned}$$

where θ_n is the local angular coordinate with origin at the scatter location, $\vec{r}_n$, and the incident wavefunction is a plane wave coming from direction θ_m. Note that in the case of s wave scattering, (4.31) reduces to the usual free space scattering equation

$$\psi(\vec{r}) = \phi(\vec{r}) + s^{(0)} H_0(k\,|\vec{r}-\vec{r}_n|)\phi(\vec{r}_n).$$

Our goal is to adapt the free space formalism to study scattering, including higher partial waves, in a Dirichlet wire; under this confinement, the wavefunction satisfies the boundary conditions $\psi(x,0) = \psi(x,d) = 0$. As we are considering an array of images of a single scatterer in a wire, we are particularly interested in the situation where the impurity lies on the y axis: See Fig. 4.6.

We define the raising/lowering operators

$$L_{\pm} = \frac{1}{ik}(\partial_x \pm i\partial_y)$$

which are two dimensional counterparts of the usual angular momentum operators in three dimensions. Applying these operators to the incident wavefunction

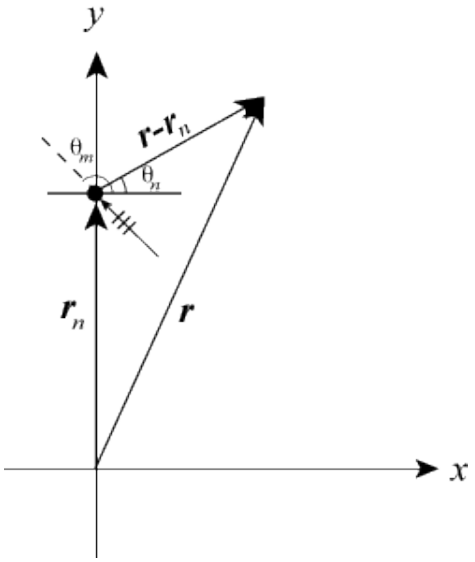

Figure 4.6: Free space scattering from a point scatterer on the y axis, at $\vec{r}_n = (0, y_n)$. We define a local angular coordinate θ_n. The incident wavefunction $\phi_m(\vec{r}) = e^{i\vec{k}(\theta_m)\cdot\vec{r}}$ is a plane wave coming from direction θ_m.

yields

$$\hat{L}_{\pm}^{l} e^{i\vec{k}(\theta_m)\cdot\vec{r}} = e^{il\theta_m} e^{i\vec{k}(\theta_m)\cdot\vec{r}}.$$

Defining

$$\begin{aligned} \hat{P}_x^{(l)} &= \frac{1}{2}\left(\hat{L}_+^l + \hat{L}_-^l\right) \\ \hat{P}_y^{(l)} &= \frac{1}{2i}\left(\hat{L}_+^l - \hat{L}_-^l\right) \end{aligned}$$

we can rewrite (4.35) in terms of our raising and lowering operators as

$$\begin{aligned} \psi(\vec{r}) &= \phi(\vec{r}) + \\ &\frac{1}{2}\sum_{l=0}^{\infty} H_l(k\,|\vec{r}-\vec{r}_n|) \times \left(\cos l\theta_n \hat{P}_x^{(l)} + \sin l\theta_n \hat{P}_y^{(l)}\right)\phi(\vec{r})\Big|_{\vec{r}_n} \end{aligned} \tag{4.33}$$

We have expressed the scattered wave entirely in terms of the values and partial derivatives of the incident wavefunction, evaluated at the point $\vec{r}_n$.

By linearity, these arguments apply to any incident function which can be constructed as a superposition of plane waves, including modes of the Dirichlet quantum wire.

4.5.3 Including p Waves in the Wire

The p wave "Green's function" in free space satisfies

$$\left(\nabla^2 + k^2\right) G^{(1)}(\vec{r} - \vec{r}') = \hat{r}_0 \cdot \nabla \delta(\vec{r} - \vec{r}')$$

(Eq. 6.13 of [55]). By analogy with the s-wave case, this relation enables us to use the method of images for p waves (and other higher partial waves) also.

Although the formalism is general, we consider for now the case of only p wave scattering. Suppose we have a series of images at $\vec{r}_n$, in the configuration shown in Chapter 2. Assume a single incident mode $\phi(\vec{r})$ which satisfies the Dirichlet boundary conditions. The solution in the wire then takes the general form

$$\begin{aligned} \psi(\vec{r}) &= \phi(\vec{r}) + s^{(0)} \sum_{n=-\infty}^{\infty} H_0(k\,|\vec{r} - \vec{r}_n|)\psi_n(\vec{r}_n) + \\ &\quad \frac{1}{ik} s^{(1)} H_1(k\,|\vec{r} - \vec{r}_n|) \times \left(\cos\theta_n \partial_x + \sin\theta_n \partial_y\right) \psi_n(\vec{r})|_{\vec{r}_n} \end{aligned} \tag{4.34}$$

where the $\psi_n(\vec{r})$ are effective wavefunctions, defined at $\vec{r}_n$ by

$$\begin{aligned} \psi_n(\vec{r}_n) &= \phi(\vec{r}_n) + s^{(0)} \sum_{p \neq n} H_0(k\,|\vec{r}_n - \vec{r}_p|)\psi_p(\vec{r}_p) + \\ &\quad \frac{1}{ik} s^{(1)} \sum_{p \neq n} H_1(k\,|\vec{r}_n - \vec{r}_p|) \left(\cos\theta_p \partial_x - \sin\theta_p \partial_y\right) \psi_p(\vec{r})|_{\vec{r}_p} \end{aligned} \tag{4.35}$$

In order that the scattered wavefunction (4.34) satisfy the Dirichlet boundary conditions, we require the $\psi_n(\vec{r})$ to satisfy the following boundary conditions:

$$\psi_n(\vec{r}_n) = (-1)^n \psi_0(\vec{r}_0) \tag{4.36}$$

$$\partial_x \psi_n(\vec{r}_n) = (-1)^n \partial_x \psi_0(\vec{r}_0) \tag{4.37}$$

$$\partial_y \psi_n(\vec{r}_n) = \partial_y \psi_0(\vec{r}_0). \tag{4.38}$$

Applying (4.36-4.38), and then evaluating (4.35) with $n = 0$, where $\theta_p = \pm\pi/2$ for $p > 0$ or $p < 0$ respectively, we find

$$\psi_0(\vec{r}_0) = \partial_y \phi(\vec{r}_0) + s_0 \psi_0(\vec{r}_0) G_r + \frac{1}{ik} s_1 \partial_y \psi_0(\vec{r}_0) G_y^{(1)} \tag{4.39}$$

where we have defined sums

$$\begin{aligned} G_r &= \sum_{p\neq 0}(-1)^p H_0(k\,|\vec{r}_0-\vec{r}_p|) \\ G_y^{(n)} &= \sum_{n=1}^{\infty}\left[H_n(k\,|\vec{r}_0-\vec{r}_{-j}|)-H_n(k\,|\vec{r}_0-\vec{r}_j|)\right] \end{aligned}$$

Similarly, differentiating $\psi_0(\vec{r})$ with respect to y and then evaluating at $\vec{r}_0$ yields

$$\begin{aligned} \partial_y\psi_0(\vec{r}_0) &= \partial_y\phi(\vec{r}_0)-ks_0\psi_0(\vec{r}_0)G_y^{(1)} \\ &\quad -iks_1\partial_y\psi_0(\vec{r}_0)\left(G_y^{(0)}-G_y^{(2)}\right) \end{aligned} \tag{4.40}$$

We can now use (4.39-4.40) to solve for $\psi_0(\vec{r}_0)$ and $\partial_y\psi_0(\vec{r}_0)$.

Similarly, if we differentiate $\psi_0(\vec{r})$ with respect to x and then evaluate at $\vec{r}_0$, we find

$$\partial_x\psi_0(\vec{r}_0)=\partial_x\phi(\vec{r}_0)+\frac{s_1}{ik}\partial_x\psi_0(\vec{r}_0)G_x \tag{4.41}$$

where

$$G_x=\sum_{j=1}^{\infty}(-1)^j\left[\frac{H_1(k\,|\vec{r}_0-\vec{r}_{-j}|)}{|\vec{r}_0-\vec{r}_{-j}|}+\frac{H_1(k\,|\vec{r}_0-\vec{r}_j|)}{|\vec{r}_0-\vec{r}_j|}\right].$$

Rearranging (4.41) yields

$$\partial_x\psi_0(\vec{r}_0)=\frac{\partial_x\phi(\vec{r}_0)}{1-\frac{s_1}{ik}G_x}.$$

Given the form of the initial wavefunction, and in particular its value and the value of its derivatives at the scatterers, we are thus, able to solve for $\psi_0(\vec{r}_0)$, $\partial_x\psi_0(\vec{r}_0)$, and $\partial_y\psi_0(\vec{r}_0)$. Substituting these values into (4.34), we have the full scattered wavefunction including p wave scattering. This method generalizes to higher partial waves.

A number of lattice sums arise in this formalism: In addition to G_r (which we used frequently in Chapter 2), G_x and G_y are required. Standard techniques exist for calculating rapidly convergent expansions for such sums: See in particular [56].

Chapter 5

Nonadiabaticity

This chapter diverges from the previous chapters on multiple scattering. Here, we examine breakdown of the adiabatic approximation in two physical systems. The first system, which we discuss in Section 5.1, is a simple wavepacket model of two cold atoms. The second system, treated in Section 5.2, is a simple model Hamiltonian for four interacting atoms.

5.1 Measuring Nonadiabaticity via Trap Loss: The Cold Atomic Hot Potato[1]

A problem of general interest in atom trapping is the validity of the Born-Oppenheimer (BO) approximation, i.e., determining the relative time scales at which the nuclear and electronic degrees of freedom evolve. We propose a scenario which addresses this question. Trapping potentials typically depend on an atom's internal state. A single two-level atom in its ground state might feel a trapping potential, while the same atom in its excited state would feel an anti-trapping potential. Suppose we have many such atoms, coupled by van der Waals interactions. If all the atoms are trapped initially, what happens when a single atom suddenly becomes excited? Two possible limits suggest themselves: (1) the excited atom leaves the trap, or (2) the atoms share the excitation so rapidly that they all remain trapped–an effective "hot potato!" Asking how well the BO approximation holds means determining which limit applies in a real

[1]This section has benefitted from helpful discussions with D. V. Bevilaqua and M. Lara Garrido.

cold atom gas. We begin with a time-dependent quantum mechanical model for the simplest possible case, two atoms confined to lines. The results suggest that the real physical situation, millions of atoms in three dimensions, may be amenable to mixed quantum-classical treatment.

5.1.1 Introduction

In the adiabatic Born-Oppenheimer approximation, the nuclear and electronic degrees of freedom of a problem separate. However, when a system's electronic energies become degenerate, the BO approximation fails–meaning that the motion of atoms causes the atoms to (nonradiatively) change their electronic states. Breakdown of the BO approximation has observable consequences in many physical systems–but the results are generally obtained indirectly via analysis of line broadening, etc.

We propose a scheme which would render BO breakdown directly experimentally observable. Suppose we have a two-level atom in a trap. The trapping potential an atom feels generally depends on the atom's internal state (e.g., its hyperfine-Zeeman sublevel). Suppose the atom in its electronic ground state feels a trapping potential, and the same atom in its excited state feels a repulsive potential and flies out of the trap.

Now consider many such atoms in a trap, coupled by van der Waals interactions. We begin with all the atoms in their ground (trapped) state. Suppose that suddenly, a laser is turned on and one atom becomes excited. What happens? One possibility is that the excited atom is simply ejected from the trap. Another possibility is that the excitation is shared among all the atoms so quickly that on average, each atom feels a trapping potential, and none falls out of the trap–an effective atomic hot potato! By way of context, the hot potato lies at the intersection of two physical phenomena: (1) transitions between trapped and untrapped atomic states and (2) resonant (nonradiative) energy transfer. The first phenomenon has applications in BEC formation by radiofrequency (rf) evaporative cooling [57], as well as in rf output couplers [58]. Additionally, such transitions are the mechanism underlying Majorana loss. Hopping via van der Waals interactions is called Forster-Dexter energy transfer; it has applications in molecular fluorescent resonant energy transfer (FRET), and plays a major role in phenomena ranging from photosynthesis to CH_2I_2 photodissociation [59]. Forster exchange between Rydberg atoms has been proposed as a mechanism for neutral atom quantum computing [60–62].

Although the hot potato is an interesting problem in its own right, the

connection to BO breakdown is not immediately obvious. However, one can phrase the problem in terms of adiabatic and diabatic nuclear dynamics. Recall that the nuclear motion is related to the motion of the atom in the trap, while excitation transfer corresponds to motion in the electronic degrees of freedom. Thus, in the *adiabatic* scenario, the nuclear motion is slow–the atom has a long time to transfer its excitation to another atom before leaving the trap. In an *diabatic* situation, the nuclear motion is fast, and the atom leaves before it has a chance to transfer its excitation. Experimentally, in the extreme adiabatic limit, one would not expect to see any trap loss, whereas in the extreme diabatic limit a steady trickle of atoms would leave the trap.

Inspired by a similar problem in chemical physics [59], we model the cold atom system first with a very simple time-dependent quantum mechanical model of two atoms on rails, approaching each other with some impact parameter. This model is deliberately minimalist; we wish to capture only two relevant aspects of the physics, the interplay between dissociation and resonant energy exchange.

The quantum mechanical model, although realistic, is only tractable for oversimplified reduced-dimensionality models (and thus impractical for a real system). The quantum mechanical treatment, however, suggests that the nuclear degrees of freedom are amenable to classical treatment, thus opening up the idea of treating more realistic systems via mixed-quantum classical methods.

The immediate question arises of what sorts of systems would lend themselves to experimental investigation of the hot potato. Many alkali atoms have coupled trapped and untrapped levels. For example, in ^{23}Na, the trapping potential depends on the hyperfine-Zeeman state of each atom. Trapped and untrapped states include $3^2S_{1/2}$, $|F = 1, M_F = 1\rangle$ and $3^2P_{1/2}$, $|F = 2, M_F = 2\rangle$ states, which are low- and high-field seeking respectively. Another example is the $|F = 2, M_F = 1\rangle$ and $|F = 2, M_F = 0\rangle$ states of the $5S_{1/2}$ manifold of ^{87}Rb, coupled by an rf field; in fact, these two states have been proposed as trapped and untrapped states for output coupler experiments on BECs [58]. The mechanisms of resonant energy transfer would be the van der Waals interaction between electric dipole moments in the first case, and spin exchange in the second.

Resonant energy transfer has been observed at a rapid rate in experiments on frozen Rydberg gases [63]. Rydberg gases are perhaps the ideal system to observe the hot potato effect in; the huge electric dipole moments between levels mean a fast transfer rate, while the spontaneous emission lifetimes are very large [64].

5.1.2 Formalism

We describe our N-atom system by the wavefunction

$$\Psi(\vec{r}, \vec{R}; t) = \sum_{i=1}^{N} \chi_i(\vec{R}; t)\phi_i(\vec{r}) \tag{5.1}$$

where $\vec{R} = (\vec{R}_1, \vec{R}_2, ...\vec{R}_N)$ is the vector of nuclear coordinates and describes the position of each atom, and $\vec{r} = (\vec{r}_1, \vec{r}_2, ..., \vec{r}_N)$ are electronic coordinates. The $\chi_i(\vec{R}; t)$ are the nuclear wavefunctions describing the distribution of the atoms in the trap, while the $\phi_i(\vec{r})$ are the basis of electronic states, related to which of the atoms is the "hot potato."

Our system starts out in its ground state, with each atom feeling an attractive trapping potential. We model the trap potential as harmonic, so that the initial state of the system is the ground state $|\Psi_g\rangle$ of the Hamiltonian

$$\hat{H}_0 = \vec{T} + \frac{1}{2}\sum_{i=1}^{N} \vec{R}_i^2 + \sum_{i<j} V(\vec{R}_{ij}),$$

the sum of kinetic energy, trapping, and interatomic potentials, R_{ij} being the distance between atoms i and j. Note that, due to the repulsive potential, this Hamiltonian is non-separable, thus N particles require the full $3N$ coordinates.

The interatomic potential is approximately $V(R_{ij}) = \frac{C_6}{R_{ij}^6} - \frac{C_8}{R_{ij}^8} + \frac{C_{10}}{R_{ij}^{10}}$, where values of the C_n for various atoms are readily available. The well due to $V(R_{ij})$ is extremely narrow on the scale of the trap, and the vast difference in length scales presents a problem numerically–if we choose a grid with spacing appropriate to the trap, then the interatomic potential falls between grid points and disappears completely. Fortunately, when such a vast difference in length scales is present, the only relevant parameter describing the narrow potential is its scattering length a. A common trick in time-independent treatments of combined trap/interatomic potentials is to replace the interatomic potential by a zero-range Fermi pseudopotential of equivalent scattering length [65]. Zero-range potentials are, however, difficult to deal with numerically in our time-dependent formalism. We therefore replace the interatomic potential by a finite-width *dilated* pseudopotential–a shallow square well with sufficient width that it shows up on our grid, but with scattering length a. In any case, the effect of the interatomic potential is quite negligible on the scale of the trap.

To return to our problem, suppose that the j^{th} atom suddenly jumps (perhaps due to brief application of a resonant, σ_+-polarized optical field) from its

ground state to its excited state. In our picture, the system has now landed on one of the N coupled, excited-state diabatic surfaces. Each of the N surfaces corresponds to one atom being excited, and they are all coupled because the excited atom can pass its excitation to other atoms via van der Waals interactions. We need to specify the new model Hamiltonian in the basis of these diabatic states. Let $\vec{R} = (\vec{R}_1, \vec{R}_2, ...\vec{R}_N)$ denote the positions of the N atoms, and approximate the trapping (and repulsive) potentials as locally harmonic. Then the relevant Hamiltonian is

$$\hat{H}_{ij} = \begin{cases} \hat{T}_i + \hat{V}_i^{diab}(\vec{R}) & i = j \\ \hat{V}_{ij}(\vec{R}) & i \neq j \end{cases} \tag{5.2}$$

where $\hat{T}_i = -\frac{1}{2}\nabla^2_{\vec{r}_i}$ are the kinetic energy operators ($\hat{T}$ is diagonal, since we have constructed $\hat{H}$ in a diabatic basis) and $\hat{V}_{ij}$ are the electronic energy surfaces. The off-diagonal terms of $\hat{H}$ correspond to the coupling by which the excitation hops between the atoms. Let $\hat{V} = \hat{V}^{(trap)} + \hat{V}^{(c)}$ where $\hat{V}^{(trap)}$ is the external trapping potential and $\hat{V}^{(c)}$ is the interatomic coupling. We consider only the sum of two-dipole interactions, and note that, if $W_{dd} = \frac{e^2}{R_{ij}^3}\left[\vec{R}_i \cdot \vec{R}_j - 3\left(\vec{R}_i \cdot \hat{n}\right)\left(\vec{R}_j \cdot \hat{n}\right)\right]$ is the usual dipole-dipole interaction between atoms i and j, then $V_i^{dd}(\vec{R}) = \langle ns, np|W_{dd}|ns, np\rangle = 0$, and $V_{ij} = \langle ns, np|W_{dd}|np, ns\rangle \propto \frac{1}{R_{ij}^3}$ for R_{ij} larger than the atomic radii [66]. Thus,

$$\hat{V}_i = \frac{1}{2}\sum_{j\neq i} R_i^2 - \frac{1}{2}R_j^2 \tag{5.3}$$

$$\hat{V}_{ij} = \sum_{j\neq i}\frac{C_3}{R_{ij}^3}, \quad R_{ij} \text{ large} \tag{5.4}$$

in dimensionless units. The diabatic potentials in (5.3) correspond to the i^{th} atom being excited, with the other $N-1$ atoms in their ground states. Thus, the i^{th} atom feels a *repulsive* harmonic potential, while the other atoms feel attractive harmonic potentials.

Applying the usual spectroscopic formalism in a manner very similar to that of photodissociation problems, all the time-dependent spectroscopic information about our system is contained in the evolution of the wavefunction

$$|\Psi_0\rangle = (\vec{\mu} \cdot \hat{e}_i)|\Psi_g\rangle$$

on the excited energy surfaces (5.3,5.4). We approximate the transition dipole

operator $\vec{\mu} \cdot \hat{e}_i$ as constant.

Having our initial wavefunction and Hamiltonian in hand, what remains is to numerically integrate the coupled time-dependent Schrodinger equations,

$$[\hat{T}_i + V_i(\vec{R})]\chi_i(\vec{R};t) + \sum_{j \neq i} V_{ij}(\vec{R})\chi_j(\vec{R};t) = i\dot{\chi}_i(\vec{R};t) \tag{5.5}$$

with the potentials (5.3, 5.4).

A short and elegant scaling argument [67] comparing the time scales of resonant energy transfer and superradiant spontaneous emission shows that it is possible to maintain coherence if the atoms are localized to a length closer then the wavelength of the radiation. In any case, frozen Rydberg gases are often cited as candidates for quantum logic operations primarily because their coherence time is so much longer than the gate time.

5.1.2.1 Quantum Mechanical Approach

Wavepacket Methods

Propagation In order to investigate the dynamics of the system, we must numerically integrate (5.5). To this end, we use the split-operator fast Fourier transform algorithm [68] as generalized to coupled energy surfaces [69]. The basic idea is to approximate the propagator as

$$e^{-i\hat{H}\Delta t} = e^{-i\hat{T}\Delta t/2} e^{-i\hat{V}\Delta t} e^{-i\hat{T}\Delta t/2} + O(\Delta t^3) \tag{5.6}$$

and switch back and forth between the position and momentum representations while propagating. $\hat{T}$ is diagonal in our (diabatic) basis; however, $\hat{V}$ is not, complicating its exponentiation in (5.6). So, to evaluate the potential energy part of the propagator, we transform to the adiabatic basis, in which $\hat{V}$ is diagonal, do the exponentiation, and then transform back.

The split-operator algorithm involves implicit periodic boundary conditions at the edges of our (finite) grid. As our problem deals with non-confining potentials, reflection from the edges of the grid becomes an issue. A standard method of dealing with reflection is to forcibly damp the wavefunction out near the grid edges [70]. We choose the function

$$f(x) = \begin{cases} e^{-\beta(x - x_{abs})^2} & x \geq x_{abs} \\ 1 & x < x_{abs} \end{cases}$$

where x represents any coordinate and x_{abs} is where the absorption begins.

5.1.2.2 Simplifying the Model

Using the above machinery, our problem of N atoms in a trap translates, from a numerical point of view, into propagating N coupled $3N$-dimensional wavepackets on repulsive energy surfaces. This is a formidable task, particularly as repulsive energy surfaces generate high-momentum components, which in turn require a very fine grid. Our first simplification to reduce the dimensionality of our problem by confining each atom to a rail which passes through the trap. The rails are separated, at their closest approach, by an impact parameter b.

The simplified, two-state version of (5.1) is

$$\Psi(\vec{r},\vec{R};t) = \chi_1(\vec{R};t)\otimes|t,u\rangle + \chi_2(\vec{R},t)\otimes|u,t\rangle$$

where $|t,u\rangle$ and $|u,t\rangle$ are a diabatic electronic basis corresponding to Atom 2 untrapped and Atom 1 untrapped, respectively. Applying (5.2), the time-dependent Schrodinger equation for the nuclear wavefunctions,

$$\hat{H}\Psi(\vec{r},\vec{R};t) = i\partial_t\Psi(\vec{r},\vec{R};t)$$

becomes

$$\Longrightarrow \begin{bmatrix} -\frac{1}{2}\nabla_1^2 + V_{11}\left(\vec{R}\right) & V_{12}\left(\vec{R}\right) \\ V_{12}\left(\vec{R}\right) & -\frac{1}{2}\nabla_2^2 + V_{22}\left(\vec{R}\right) \end{bmatrix} \begin{bmatrix} \chi_1(\vec{R};t) \\ \chi_2(\vec{R};t) \end{bmatrix} = i \begin{bmatrix} \dot{\chi}_1(\vec{R};t) \\ \dot{\chi}_2(\vec{R};t) \end{bmatrix}$$

with diabatic potentials

$$V_{11} = \frac{1}{2}(\vec{R}_1^2 - \vec{R}_2^2) \tag{5.7}$$

$$V_{22} = \frac{1}{2}(-\vec{R}_1^2 + \vec{R}_2^2) \tag{5.8}$$

$$V_{12} = \frac{C_3}{R_{12}^3} \tag{5.9}$$

as in (5.3,5.4). The diabatic surface (5.7) corresponds to Atom 1 trapped and Atom 2 untrapped, while the diabatic surface (5.8) corresponds to Atom 2 trapped and Atom 1 untrapped. The diabatic coupling term in (5.9) is due

to the dipole-dipole coupling between atoms,

$$\begin{aligned} \hat{V}_{dd} \quad &\propto \quad \frac{\vec{R}_1 \cdot \vec{R}_2 - 3(\vec{R}_1 \cdot \hat{n})(\vec{R}_2 \cdot \hat{n})}{R_{12}^3} \\ &\Longrightarrow \quad \left\langle SP \left| \hat{V}_{dd} \right| PS \right\rangle \propto \frac{C_3}{R_{12}^3}, \qquad R_{12} \text{ large} \end{aligned}$$

where $C_3 \propto e^2 a_0^2$ in cgs units, and depends on which levels are coupled.

We note that due to the parabolic level crossing and sharp coupling, the intersection is neither a Landau-Zener (linear) nor Renner-Teller (parabolic) situation.

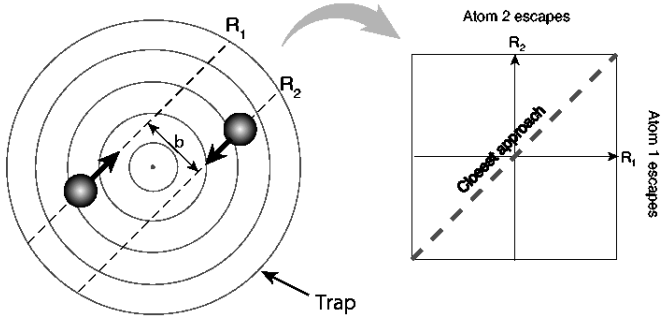

Figure 5.1: Mapping of physical coordinates to the space the wavefunction lives on. The dashed line corresponds to the closest approach of the two atoms, where they are separated by the impact parameter b.

Fig. 5.2 shows the adiabatic and diabatic energy surfaces. Note that the coupling is significant along the line $r_1 = r_2$, away from which the adiabatic surfaces reduce to the diabatic surfaces.

We can define a dimensionless adiabaticity parameter (the analog of the usual Massey parameter) for this system as $\xi = \frac{\omega}{\Omega} = \frac{\omega r_0^3}{C_3}$. This parameter compares the frequency of trap oscillation to the Rabi frequency of energy transfer. For $\xi \ll 1$ the system is in the adiabatic regime. For $\xi \gg 1$ the system is in the diabatic limit. The following factors contribute to adiabatic behavior: high

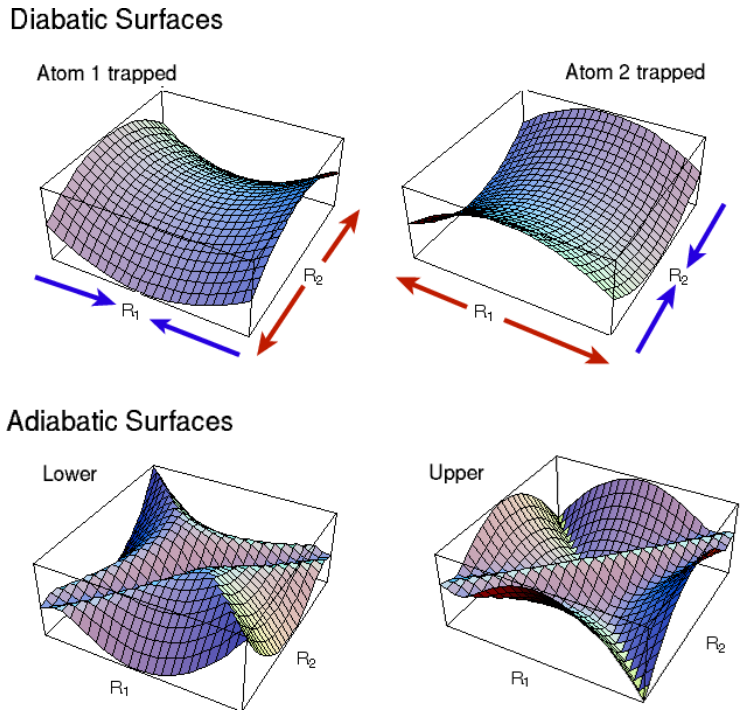

Figure 5.2: Adiabatic and diabatic surfaces. The adiabatic surfaces are flat along $r_1 = r_2$, corresponding (in a quasiclassical picture) to the excitation being exchanged so quickly among the atoms that on average each atom feels zero potential. The two atom scenario is the "worst-case" scenario for observing the hot potato, as the average "trapping" potential is non-binding. This escape should, however, be much slower than the equivalent escape on a repulsive surface.

atomic densities, strongly coupled atomic levels, or a weak trap potential. Conversely, a low density of atoms, weak interaction, or a tight trap favor a diabatic limit.

5.1.2.3 Results and Discussion

Rapid resonant exchange is observed in [63] between the $25s$ and $24p$ Rb atoms. We choose parameters from this system, and calculate C_3 between the $25s$ and $24p$ Rydberg levels of Rb ($Z = 37$) as

$$\frac{1}{R_{AB}^3} \left| \int_0^\infty r^2 R_{25s}(r) R_{24p}(r) dr \right|^2 \times \frac{4\pi}{3} (\delta_{m,1} - 2\delta_{m,0} + \delta_{m,-1})$$

Calculating C_3 The usual van der Waals interaction between two atoms at $\vec{r}_A$ and $\vec{r}_B$ is

$$V_{dd} = \frac{x_A x_B + y_A y_B - 2 z_A z_B}{R_{AB}^3}.$$

Taking the matrix element between the states nS and $n'P$, we find

$$\begin{aligned} < nS_A n'P_B | \hat{V}_{dd} | n'P_A nS_B > &= \frac{e}{R_{AB}^3} \int d\vec{r}_A \int d\vec{r}_B nS(\vec{r}_A) \times \\ & \quad n'P(\vec{r}_B) \hat{V}_{dd} n'P(\vec{r}_A) nS(\vec{r}_B) \\ &= \frac{\mu}{R_{AB}^3} \times \frac{4\pi}{3} (\delta_{m,1} - 2\delta_{m,0} + \delta_{m,-1}) \end{aligned}$$

where μ is the transition dipole moment between the two states. We note that the matrix element depends on the polarization of the atoms.

C_3 depends on the projection of angular momentum. For $m = \pm 1$, we find a value of $C_3 = (139 e a_0)^2$. From [63], a typical atomic density of $10^9 \mathrm{cm}^{-3}$, $V_{12}(R)$ corresponds to a Rabi frequency of 0.329 MHz. This oscillation is much faster than a typical magnetic trap frequency (a few kHz). However, the other relevant time scale is the escape time in the inverted trap, which depends strongly on the initial conditions. Thus a priori it is not at all obvious which limit we will end up in.

Suppose we choose a typical magnetic trap frequency of 1 kHz. It turns out that a realistic physical picture lies between the adiabatic and diabatic limits, with the relevant limit depending strongly on the atomic density: Some representative results are shown in Figs. 5.3 and 5.4.

We draw two principal conclusions from our quantum mechanical simulations. The first is that whether we are in the adiabatic or diabatic limit depends sensitively on the impact parameter of a collision. The second is that the collision dynamics, even in this truly quantum system of cold atoms, looks surprisingly classical.

5.1.3 Possibility of a Mixed Quantum-Classical Approach

The above model gives some insight into the rather restrictive, toy model of two atoms confined to rails in a trap. A realistic physical situation, however, corresponds to roughly 10^8 atoms in a trap, each of which lives in three dimensions– i.e., a realistic physical model requires not two, but 3×10^8 atoms. Cold atom systems typically exhibit quantum phenomena. So the results of the previous section are surprising in that the atoms appear to behave classically (albeit half of each atom escapes, rather than one atom escaping entirely). The reason

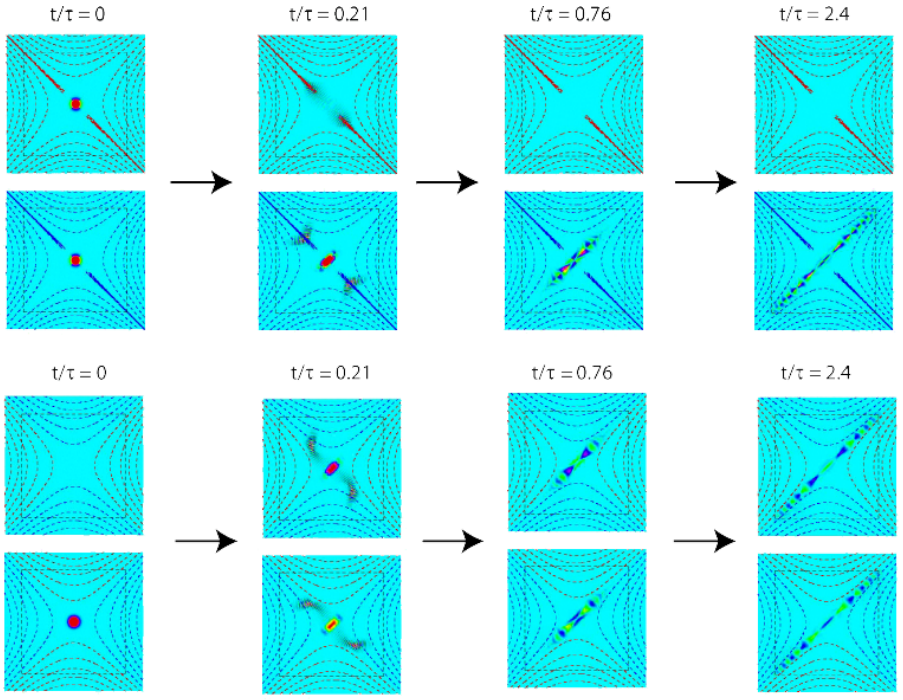

Figure 5.3: This figure shows the time evolution of the two atom systems for an impact parameter $b = 4.0$. The top row shows the evolution on the adiabatic surfaces; the bottom row shows evolution on the two diabatic surfaces. The initial condition is Atom 2 excited; the wavepacket is fully on one diabatic surface. Although some amplitude leaks away, some amplitude remains trapped for 2.4 trap periods. This trapped amplitude is on both diabatic surfaces, corresponding to the excitation hopping between atoms, and the atoms remaining trapped. (Color online).

for this classical behavior is simply that interference does not matter in systems with unstable degrees of freedom; the amplitude "leaks" away along the unstable degree of freedom and does not return to interfere with itself.

An approximation is obviously required to treat the real system, and the one that immediately suggests itself is some version of Tully-Preston surface hopping [71]. The physical meaning of this is that we approximate the motion of atoms within the trap classically, while modelling the excitation hopping quantum-mechanically. This method is only strictly suited to weak couplings, and in our case, as there is a great deal of hopping near $r_1 = r_2$, conservation of energy becomes a problem. One approach would be to consider hopping between adiabatic surfaces–the obstacle being that our Hamiltonian is better suited to a

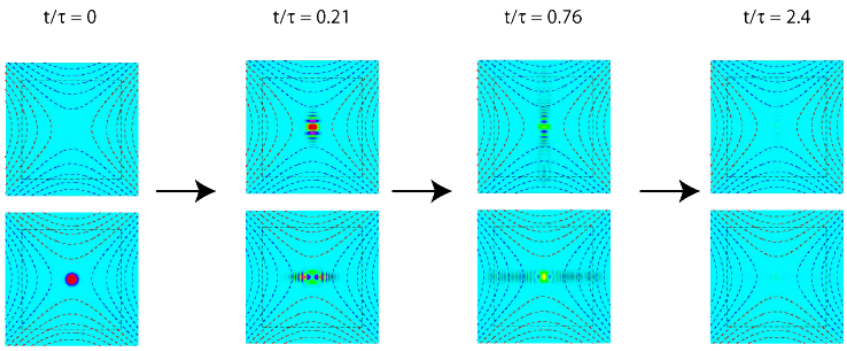

Figure 5.4: This figure shows evolution in the diabatic basis for an impact parameter much larger than in Fig. 5.3, $b = 15.0$. By 2.4 trap periods, the beam has entirely leaked away, in contrast to Fig. 5.3 where a fraction has remained trapped. Whether we are in an adiabatic or diabatic limit is a sensitive function of the atom density. (Color online).

diabatic representation, and the diabatric couplings are much simpler than the nonadiabatic matrix elements. A solution might be to tweak our model so that hopping conserves a particle's energy, rather than its position. In summary, our quantum mechanical results show that the potential exists for applying quasiclassical methods to this system, and examining the many body problem of adiabaticity vs. nonadiabaticity.

Suppose the atoms follow classical trajectories, $\vec{R}_i(t)$, in the trap. As each atom moves forward in time, it sees an effective 1D potential surface; that is, $V_i(\vec{R}) \to V_i(\vec{R}(t)) = V_i(t)$. Using a variation on the usual surface hopping, we compute the hopping probability at each time.

Under the above assumptions, our wavefunction becomes

$$\psi(t) = \chi_1(\vec{R}(t);t) \otimes |t,u\rangle + \chi_2(\vec{R}(t);t) \otimes |u,t\rangle \,,$$

where the χ_i satisfy the time dependent Schrodinger equation,

$$\begin{aligned} H_{el}\psi(t) &= i\partial_t\psi(t) \\ &= i\left[\left(\partial_t + \vec{v}\cdot\vec{\nabla}_{\vec{R}}\right)\otimes I\right]\left(\chi_1(\vec{R}(t);t)\otimes|t,u\rangle + \chi_2(\vec{R}(t);t)\otimes|u,t\rangle\right) \end{aligned}$$

where $\vec{v} = \frac{d\vec{R}}{dt}$. Putting this in matrix form, we would end up with the usual

ugly matrix elements $\langle\phi_i|\,\vec{v}\cdot\vec{\nabla}_{\vec{R}}\,|\phi_j\rangle$ where the $\{\phi\}$ are the electronic basis. Had we chosen the $\{\phi\}$ adiabatically, the magnitudes of these matrix elements would blow up at degeneracies, where the electronic wavefunctions changed character quickly. However, our Hamiltonian is in a physical (diabatic) basis in which we have already assumed that the magnitudes of such coupling terms are negligible. Thus we have simply

$$i\begin{bmatrix}\dot{\chi}_1\\ \dot{\chi}_2\end{bmatrix}=\begin{bmatrix}V_{11}(\vec{R}(t)) & V_{12}(\vec{R}(t))\\ V_{12}(\vec{R}(t)) & V_{22}(\vec{R}(t))\end{bmatrix}\begin{bmatrix}\chi_1\\ \chi_2\end{bmatrix}. \tag{5.10}$$

We integrate this equation when the hot potato approaches another particle, in order to calculate the $|\chi_i|^2$, which determine the hopping probability at each time step. We find again that whether we end up in the adiabatic or diabatic picture depends strongly on the atomic density; see e.g. Fig. 5.5.

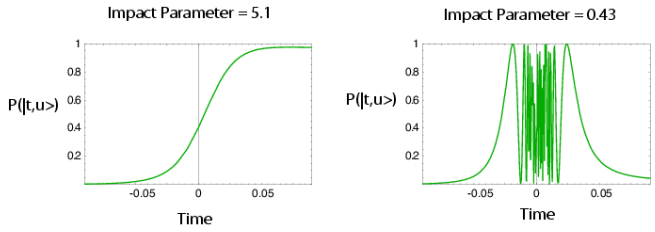

Figure 5.5: Beginning in $|u,t>$, probability $|\chi_1(t)|^2$ during the collision of finding $|t,u>$ (excitation transfer). The probability clearly depends on the impact parameter of the collision. At high impact parameters (left) there is time for only one exchange before the atoms separate. At lower impact parameters (right) the excitation can hop back and forth many times, and remain trapped briefly, before the untrapped atom escapes.

To summarize, we have in this chapter examined a model system which loosely represents the dynamics of a pair of two level atoms in a trap/antitrap. We find that whether the atoms are in the adiabatic limit of rapid transfer, or the diabatic limit of trap loss, depends sensitively on the nature of the collision. We further find that this problem is amenable to approximation via a method that would allow the treatment of many atoms.

5.2 Degeneracies in a Simple Model System

The basic question we examine in this section is the breakdown of adiabaticity in even a very simple, model N atom system. We know that the space of degeneracies in a system generally has codimension two. In the case of three interacting atoms (for example the hydrogen exchange reaction) the space of degeneracies is trivial, and degeneracies occur at a diabolical point. With N atoms the situation is considerably more complicated, and the space of degeneracies can be a complicated hypersurface in many dimensions. Here we choose a toy matrix Hamiltonian which loosely mimics a system of four interacting atoms, and explore the degeneracies of the energy levels. We find that even in this small and simple system, the degeneracies are complicated hypersurfaces which do not necessarily correspond to any symmetries in the system. It is an interesting thought that a molecule consisting of N atoms is always navigating a forest of diabolical points, with concomitant Berry phases appearing every time the system makes a circuit of a degeneracy.

5.2.1 Hamiltonian

Transitions within the first excited manifold of a system of interacting dipoles are described in [72] with the Hamiltonian:

$$\begin{aligned} H_{ii} &= \omega_0 - i\gamma_0 \\ H_{ij} &= \gamma_0(\Delta_{ij} - iC_{ij}) \end{aligned}$$

where ω_0 is the energy, γ_0 is a decay constant, and

$$\Delta_{ij} = \frac{3}{2}\left(\frac{\cos r_{ij}}{r_{ij}^3} + \frac{\sin r_{ij}}{r_{ij}^3} - \frac{\cos r_{ij}}{r_{ij}}\right) \tag{5.11}$$

$$C_{ij} = \frac{3}{2}\left(-\frac{\sin r_{ij}}{r_{ij}^3} + \frac{\cos r_{ij}}{r_{ij}^3} + \frac{\sin r_{ij}}{r_{ij}}\right). \tag{5.12}$$

By first excited manifold, we refer to the set of states with a single excitation, e.g. $\{|egg\cdots>, |geg\cdots>, |gge\cdots>\}$ where g and e denote ground and excited states. This Hamiltonian assumes fixed nuclei, which intuitively makes sense for cold atoms. However, adiabatic approximations break down near nuclear configurations where energy surfaces cross. That is, one can no longer separate nuclear and electronic motions, and nuclear motion causes transitions between electronic states.

As we are interested in a simple model N-atom system, we examine the following simplified Hamiltonian, loosely based on the dipole-dipole Hamiltonian in [72]. It comes from dropping the non-Hermitian part (neglecting transitions to other manifolds) and assuming small interatomic distances:

$$\begin{aligned} H_{ii} &= \omega_0 \\ H_{ij} &= \frac{\cos(r_{ij})}{r_{ij}^3} \end{aligned}$$

N atoms in a plane will have, excluding rotations and translations, $2N-3$ independent degrees of freedom. Assuming a real, Hermitian Hamiltonian, surfaces of conical intersections will always have codimension two. We take $N = 4$, that is, a 5-D parameter space consisting of displacements along two strain modes, two shuffle modes, and a breathing mode. Surfaces of intersections of two PESs will be three-dimensional.

5.2.2 Energy Surfaces

Figure 5.6 shows how the energies vary along each normal mode, and the corresponding nuclear configurations. Degeneracies or avoided crossings appear in each of these plots, often in configurations that do not have any obvious symmetries. The first and second strain modes pass through points where two nuclei are in the same place; not surprisingly, the energies diverge there. The breathing mode is–surprisingly, not trivial. The symmetric stretch vibration occurs entirely on the surface of symmetry-allowed degeneracies at the D_{4h} configuration. So only three eigenvalues appear on the plot, because two are everywhere degenerate. The interesting point to note is that *multiple* surfaces intersect in several places. The first and second shuffle modes have equal energies, by symmetry, and we do not illustrate the second shuffle mode.

5.2.3 Level Spacings

An interesting question might be, if we randomly choose points in the parameter space (corresponding to nuclei moving randomly through a set of configurations) how often we land near a degeneracy. The distribution of level spacings is shown in Fig. 5.7.

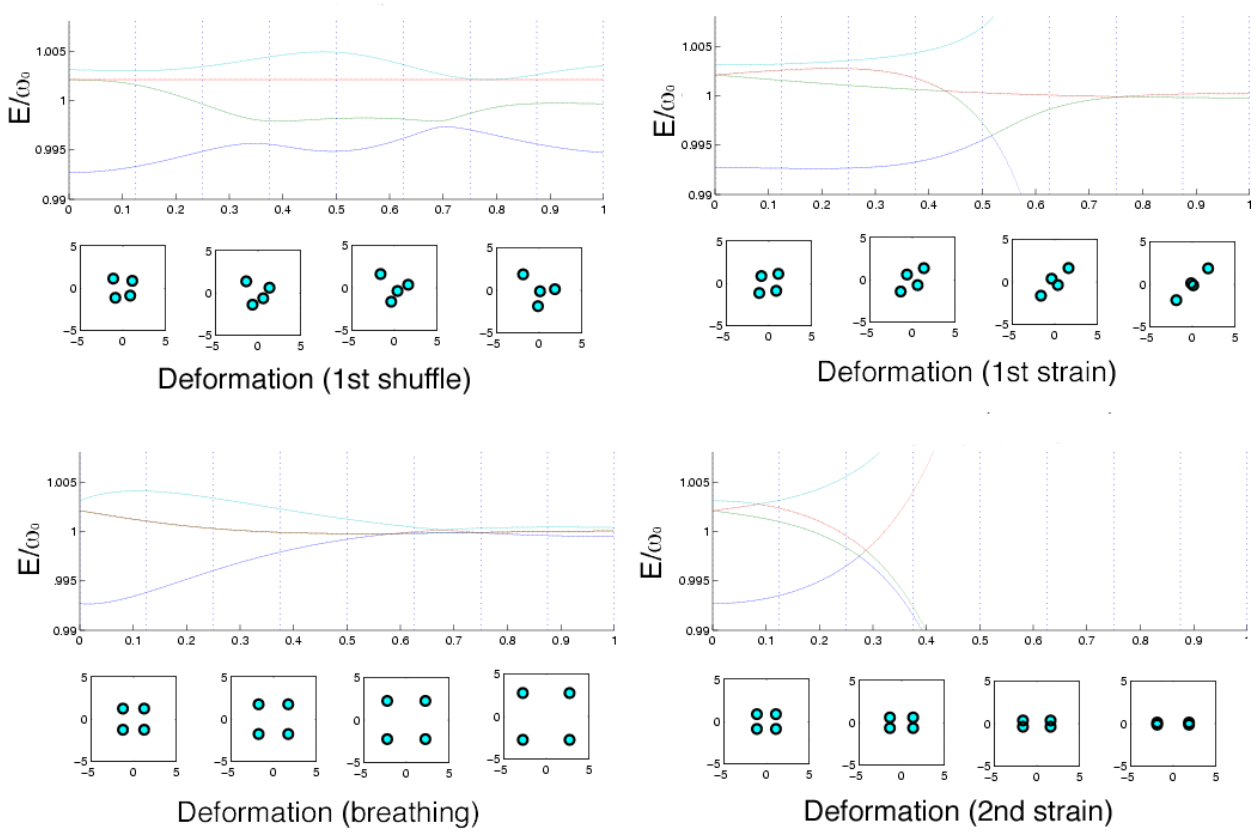

Figure 5.6: Variation of the energies as the nuclei are moved through each mode (deformation illustrated below). The units of deformation are arbirary.

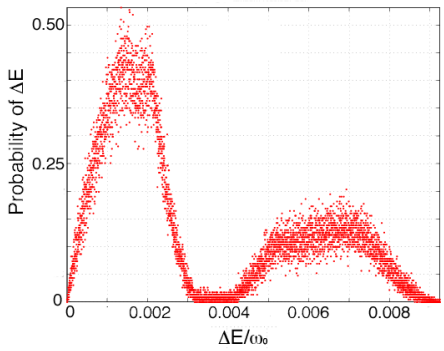

Figure 5.7: Energy Spacings– If we randomly choose points in some bounded region of the parameter space, we obtain the above distribution of nearest-neighbor energy spacings. Note the double peak structure: Random matrix theory predictions for the Gaussian Orthogonal Ensemble do not apply–our ensemble of matrices is not random, but rather highly constrained.

5.2.4 Degeneracies

Degeneracies will occur in 3-D subspaces of the full 5-D parameter space. The first goal is to locate and understand the topology of these surfaces of intersections.

Degeneracies were located by minimizing the squared energy differences ΔE_{ij}^2 using a Nelder-Mead simplex functional optimization algorithm with several thousand random initial conditions. Fig. 5.8 shows a section of the 3-D surface of degeneracies, as the nuclei are deformed along the first strain and breathing modes.

These curves are slices of much more complicated 3-D hypersurfaces. Figure (5.9) shows what the surfaces look like in one more dimension. Notable features are the existence of multiple, disjoint surfaces. One parameter value can correspond to multiple degeneracy surfaces.

We have, in this section, examined a very simple matrix Hamiltonian with interactions depending on atomic distances. We have demonstrated that not only do degeneracies arise frequently in configuration space, but that the surfaces of energy degeneracies have a complicated structure. Although our model does not represent a specific physical system, the phenomena we describe are general. Surfaces of degeneracies have codimension two, and for many-atom systems, sheets of degeneracies occur in unexpected locations: A moving system of many atoms can circle one of these surfaces, and pick up a Berry phase.

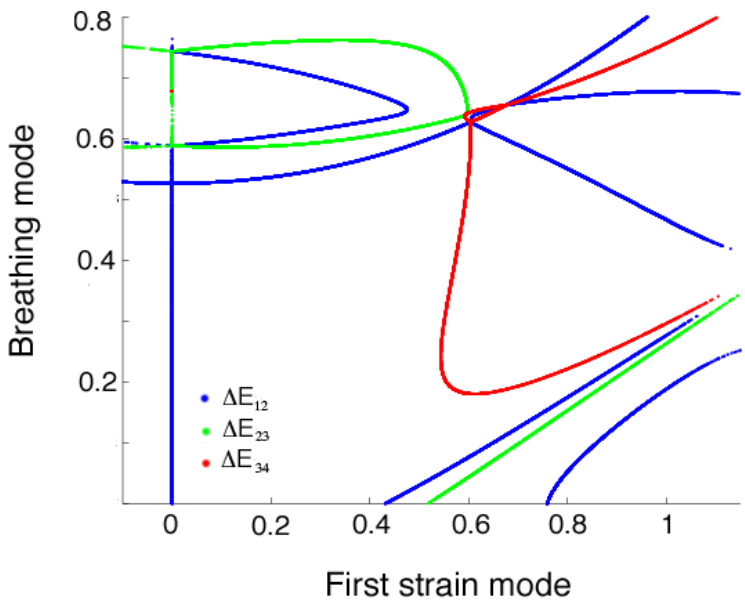

Figure 5.8: Cross-section of the three separate surfaces of degeneracies. We saw before (Fig. 5.6) that there should be a degeneracy for all square configurations, i.e., along the y-axis of this figure. Interesting points are the bifurcations in the curves of degeneracies, and the fact that at several points, *three* energy surfaces intersect. The axes describe the deformation, in the same arbitrary units as in Fig. 5.6.

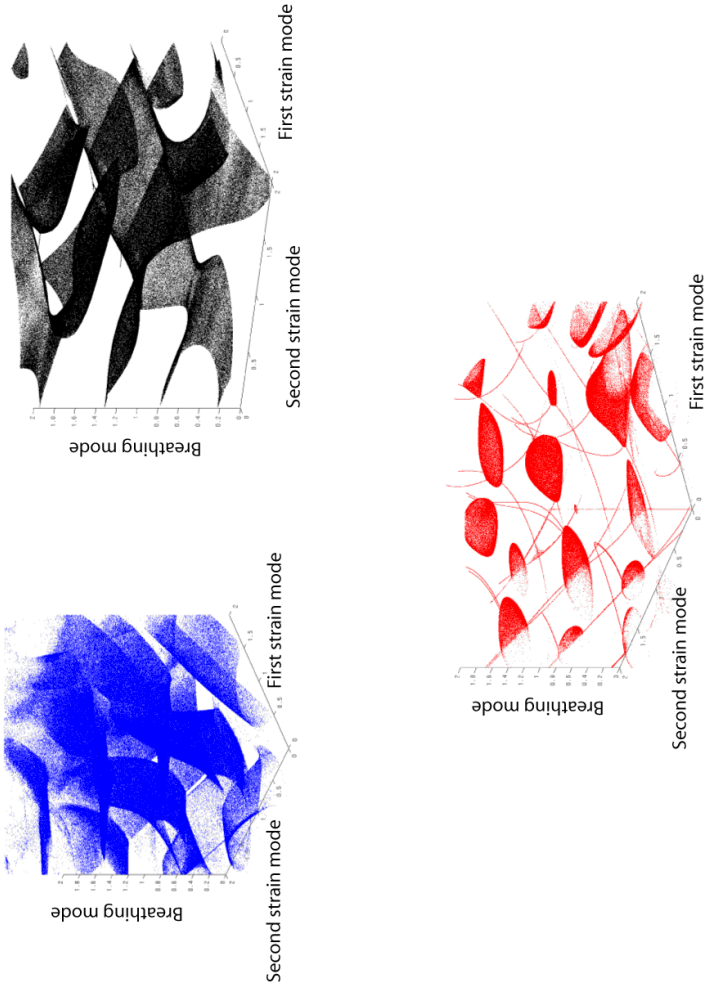

Figure 5.9: Cross sections of the three degeneracy surfaces, for deformation along the two strain modes and the breathing mode. Note the interesting structure of the surfaces, and also that degeneracies are present across almost the entire space.

Appendix A

2D Scattering and the t Matrix

Multiple scattering via Foldy's Method [18] has been treated extensively in several other theses in the Heller Group [1, 32, 55]; the notation I shall follow is identical to that of [55]. Beyond the bare essentials, I shall not reproduce the methodology here.

Consider a particle, in two dimensions, scattering from a radial potential $V(r)$ which is finite range. For our purposes, a t matrix is a formal tool for representing, exactly, the long range s wave scattering of any potential. In the t matrix approximation, outside the potential, the scattered wavefunction is

$$\psi(\vec{r}) \quad = \quad e^{i\vec{k}\cdot\vec{r}} - \frac{i}{2}\sum_{l=-\infty}^{\infty} i^l s_l(k) H_l^{(1)}(kr) e^{il\theta},$$

an incoming wave plus a scattered wave which is a superposition of higher partial waves. Using the Jacobi-Anger expansion for a plane wave,

$$\psi(\vec{r}) = \frac{1}{2}\sum_{l=-\infty}^{\infty} i^l e^{il\theta}\left\{\left[1 - is_l(k)\right] H_l^{(1)}(kr) - iH_l^{(2)}(kr)\right\}.$$

The scattered wavefunction is a superposition of incoming and outgoing partial waves. The amplitude of each incoming partial wave cannot change; only its phase can, and we thus define the phase shifts in the usual way, so that

$$1 - is_l(k) = e^{2i\delta_l}. \tag{A.0.1}$$

This requirement is a case of the optical theorem, and applying

$$|1 - is_l(k)|^2 = 1$$

yields the optical theorem on the t matrix:

$$\mathrm{Im}s(k) = -\frac{1}{2}\left|s_l(k)\right|^2. \tag{A.0.2}$$

In the low-energy limit, we can work in the s wave approximation, where

$$\psi(\vec{r}) \quad = \quad e^{i\vec{k}\cdot\vec{r}} - \frac{i}{2}s(k)H_0^{(1)}(kr). \tag{A.0.3}$$

Essentially, the t matrix representation takes the part of the scattered wavefunction which is outside of the potential, and extends it to all space. This means that inside the potential, the t matrix representation is meaningless, but outside of the potential, the point t matrix potential mimics exactly the long-range s wave scattering for any potential.

Simulating Different Scattering Potentials

To simulate a hard disk of radius $r = a$, we can apply the boundary condition $\psi(a) = 0$. Applying this boundary condition to (A.0.3), and expanding the incoming wavefunction in cylindrical waves, we find the condition

$$s(k) = -2i\frac{J_0(ka)}{H_0^{(1)}(ka)}. \tag{A.0.4}$$

It is easy to show that (A.0.4) satisfies the optical theorem (A.0.2).

Suppose we wish to simulate an attractive scatterer.[1] An example of a potential for which we can analytically calculate the s wave scattering properties, is a soft attractive disk

$$V(r) \quad = \quad -V_0\Theta(r-a)$$

[1] An immediate thought might be to simply use (A.0.4) with $a < 0$; however, it turns out that for $a < 0$, (A.0.4) is nonunitary. A related form which *is* unitary for all ka is

$$s(k) = -2i\mathrm{sign}(ka)\frac{J_0(ka)}{H_0^{(1)}(ka)},$$

however $a < 0$ is no longer a scattering length, since the zero-energy wavefunction no longer vanishes there.

where $V_0 > 0$. The s wave phase shift is determined by the continuity of the logarithmic derivative of the wavefunction at $r = a$:

$$\tan \delta_0 = \frac{kJ_0(qa)J_1(ka) - qJ_1(qa)J_0(ka)}{qJ_1(qa)Y_0(ka) - kJ_0(qa)Y_1(ka)} \tag{A.0.5}$$

where the inside wavenumber is

$$q \equiv \sqrt{2(E + V_0)}.$$

Combining (A.0.1) with (A.0.5), we can find the t matrix appropriate to the attractive potential:

$$s(k) = \frac{i \tan \delta_0}{1 - i \tan \delta_0}. \tag{A.0.6}$$

After some algebra, it is possible to confirm that the negative energy poles of the t matrix (A.0.6) occur at

$$qK_0(\kappa a)J_1(ka) = \kappa K_1(\kappa a)J_0(ka) \tag{A.0.7}$$

where $\kappa \equiv \sqrt{-2E}$; Eq. (A.0.7) can be derived directly as the characteristic equation for bound states of the 2D cylindrical well.

Appendix B

Wire as a Diffraction Grating

In Sec. 2.3.1, we used the mathematical equivalence of the wire to a periodic array of image scatterers. Further extending the analogy, we now reformulate the problem of the confined impurity as one of diffraction from an infinite, periodic grating, and the scattered wavefunction as a diffracted beam. We wish to note the detail that because of our Dirichlet boundary conditions, our incident beam is a sum of two plane waves rather than a single plane wave:

$$\begin{aligned}\phi_m(x,y) &= \frac{1}{\sqrt{k_x^{(m)}}} e^{ik_x^{(m)}|x-x_0|}\chi_m(y) \\ &= \frac{1}{id}\frac{1}{\sqrt{k_x^{(m)}}} e^{ik_x^{(m)}|x-x_0|} \times \left(e^{ik_y^{(m)}y} - e^{-ik_y^{(m)}y}\right).\end{aligned}$$

Due to the linearity of Schrodinger's equation, we can consider each of the constituent plane waves as scattering independently. The relevant physics thus reduces to diffraction of a single plane wave incident on a periodic array of scatterers.

When our incident wavefunction strikes the diffraction grating, we expect that in the Fraunhofer limit, far from the array, the diffracted beam will be a sum of plane waves at the Bragg angles (see Fig. B.1).

Each order of the diffracted beam will have a different weighting; our object is to cast our Green's function (2.18) in a manner that makes these weightings explicit. This formulation is of interest because it is equivalent to determining

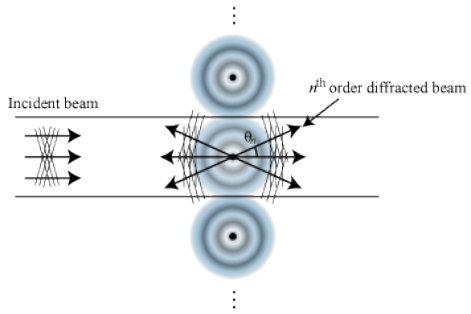

Figure B.1: A mode incident on an impurity in the hard wire is, effectively, a superposition of two plane waves incident on an infinite diffraction grating. At large distances from the scatterer, the scattered wave must therefore be a sum of plane waves at the Bragg angles. Closer to the scatterers, evanescent modes appear also.

the transmission and reflection coefficients of our system. Namely, if we send in a mode, we would like to know what modes come out and with what intensities, which is precisely what we shall find by casting our scattering wavefunction as a diffracted beam.

To begin, we note that Bessel functions are regular, and consequently have plane wave expansions. In fact, the well-known integral form of the Bessel function

$$J_0(kr) = \frac{1}{2\pi}\int_0^{2\pi} e^{i\vec{k}(\theta)\cdot\vec{r}}d\theta \tag{B.0.1}$$

expresses the Bessel function as an isotropic sum of plane waves emanating in all directions from the origin. We can rewrite (B.0.1) in terms of a line integral over $k_y$as

$$\begin{aligned} J_0(kr) &= \frac{1}{2\pi}\int_C \frac{d(k\sin\theta)}{k\cos\theta} e^{i(k_x,k_y)\cdot(x,y)} \\ &= \frac{1}{2\pi}\int_C \frac{dk_y}{k_x} e^{i(k_x,k_y)\cdot(x,y)} \end{aligned} \tag{B.0.2}$$

where C lies along the real axis, going back and forth within the interval $(-k, k)$.

We seek an analogous expression for the Hankel function. Since $|k_y|$ is always less than k in (B.0.2), k_x is always real, and the plane waves in (B.0.2) do not include evanescent waves. Suppose we modify the right-hand side of (B.0.2). By permitting k_y to range from $-\infty$ to ∞, we may include contributions from

all possible evanescent waves, yielding

$$\frac{1}{2\pi}\int_{-\infty}^{\infty}\frac{dk_y}{k_x}e^{i(k_x,k_y)\cdot(x,y)}. \tag{B.0.3}$$

For $|k_y| > k$, the corresponding value of $k_x = \pm i\kappa_x$, where $\kappa_x \equiv \sqrt{k_y^2 - k^2}$, is imaginary. Choosing the positive value makes the evanescent waves die off to the right ($x > 0$) and diverge to the left ($x < 0$). Therefore, with this choice of sign, we may expect (B.0.3) to converge only in the right half-plane.

By adding on an evanescent contribution to the Bessel function's plane wave expansion, we have in fact arrived (up to a constant) at an integral form of the Hankel function, valid in the right half-plane only,

$$H_0^{(1)}(kr) \quad = \quad \frac{1}{\pi}\int_{-\infty}^{\infty}\frac{dk_y}{k_x}e^{i(k_x,k_y)\cdot(x,y)} \tag{B.0.4}$$

where

$$k_x = \begin{cases} \sqrt{k^2 - k_y^2} & |k_y| \le k \\ i\sqrt{k_y^2 - k^2} & |k_y| > k. \end{cases}$$

Eq. (B.0.4) is a well-known expansion, [21] readily obtained by Fourier transforming Green's equation.

Consider now the sum

$$G_p(\vec{r}; d) = -\frac{i}{2}\sum_{n=-\infty}^{\infty} H_0(k\,|\vec{r} - (x_0, nd)|) \tag{B.0.5}$$

which is the Green's function for a fully periodic array of scatterers at (x_0, nd) (or equivalently, a periodic wire with walls at $y = 0, y = 2d$ and a scatterer halfway between). Based on the physical picture of diffraction (Fig. B.1), the sum in (B.0.5) must be a superposition of plane and evanescent waves at real and complex Bragg angles respectively. We wish to find the weighting on each wave (analogous to the structure factor in X-ray diffraction).

To find the weights, we calculate the expansion explicitly. Using (B.0.4) in (B.0.5), we find

$$
\begin{aligned}
G_p(\vec{r},\vec{0}) &= -\frac{i}{2}\sum_{n=-\infty}^{\infty} H_0(k|\vec{r}-\vec{r}_n|) \\
&= -\frac{i}{2\pi}\sum_{n=-\infty}^{\infty}\int_{-\infty}^{\infty}\frac{dk_y}{k_x}e^{i(k_x,k_y)\cdot(x-x_0,y-nd)} \\
&= -\frac{i}{2\pi}\int_{-\infty}^{\infty}\frac{dk_y}{k_x}e^{i(k_x,k_y)\cdot(x-x_0,y)}\sum_{n=-\infty}^{\infty}\left(e^{-i(k_y d)}\right)^n \\
&= -\frac{i}{d}\int_{-\infty}^{\infty}\frac{dk_y}{k_x}e^{i(k_x,k_y)\cdot(x-x_0,y)} \\
&\quad\times\sum_{m=-\infty}^{\infty}\delta(k_y-\frac{2m\pi}{d})
\end{aligned}
\tag{B.0.6}
$$

where we have used

$$
\sum_{n=-\infty}^{\infty}\left[e^{ik_y d}\right]^n = 2\pi\sum_{n=-\infty}^{\infty}\delta(k_y d-2\pi n),
$$

(similar to stationary phase) to reach the expression (B.0.6). One can, more rigorously, reach (B.0.6) via the Poisson sum formula. [34, 73]

Performing the integral in (B.0.6) yields the final expression

$$
G_p(\vec{r},\vec{r}_m;k,d) = -\frac{i}{d}\sum_{n=-\infty}^{\infty}\frac{1}{k_x^{(n)}}e^{ik_x^{(n)}|x-x_0|}\cos(k_y^{(n)}y)
$$

where we use the absolute value signs to extend the Green's function to converge on $x < x_0$, and we define

$$
\begin{aligned}
k_x^{(n)} &= k\cos\theta_n \\
k_y^{(n)} &= k\sin\theta_n
\end{aligned}
$$

where the θ_n are the Bragg angles

$$
\theta_n = \arcsin\frac{2n\pi}{kd} \qquad n \text{ integer}
$$

and the complex-valued θ_n are the result of the logarithmic singularity.

The image representation of our wire is not exactly the periodic array of Fig. B.1. The images alternate in sign, and in general the scatterer is off-center. We can, however, represent our image array as a sum of two arrays, as in Fig. B.2.

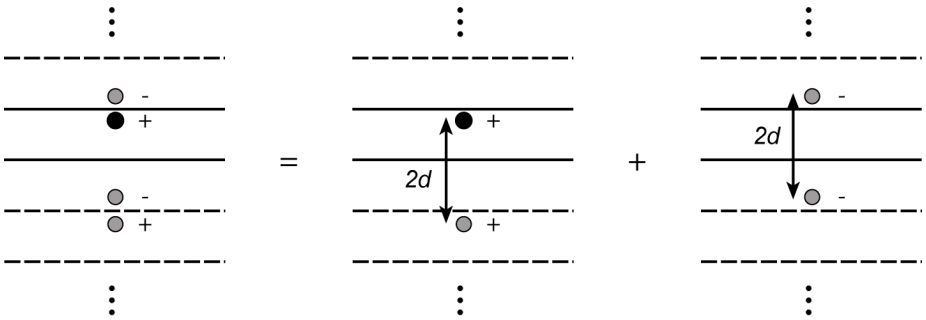

Figure B.2: In the case of the off-center scatterer, the relevant image array is the sum of two periodic arrays of opposite signs. If the source is at (x_0, y_0), the image locations are $(x_0, y_0 + 2nd)$, $(x_0, -y_0 + 2nd)$ for the positive and negative arrays respectively, where $n = \pm 1, \pm 2, \ldots$.

One can easily verify that the Green's function for the wire with point source at $\vec{r}_0 = (x_0, y_0)$ becomes the sum

$$\begin{aligned} G_w(\vec{r}, \vec{r}_0) &= \frac{1}{2}\left[G_p(\vec{r} - y_0\hat{y}; 2d) - G_p(\vec{r} + y_0\hat{y}; 2d)\right] \\ &= -i\sum_{n=1}^{\infty} \frac{1}{k_x^{(n)}} e^{ik_x^{(n)}|x-x_0|} \\ &\quad \times \chi_n(y)\chi_n(y_0) \end{aligned} \tag{B.0.7}$$

where the Bragg angles are modified slightly from the case of the periodic wire, and defined by

$$\sin\theta_n = \frac{n\pi}{kd}.$$

The form (B.0.7) is identical to (2.14). We have shown that diffraction translates the method of images into the usual eigenfunction expansion of the Green's function.

Appendix C

Improving Convergence of the Green's Function

Form (2.14) of the Green's function converges slowly also. The reason for the slow convergence is the singularity at the source, which is present but disguised in the evanescent modes. We use the Kummer method for convergence acceleration [73], which also makes the singularity explicit. Kummer's method involves adding and subtracting a multiple of the static ($k = 0$) Green's function.

The wire Green's function is

$$G_w(\vec{r},\vec{r};k) \quad = \quad -i\sum_{m=1}^{\infty}\frac{1}{k_x^{(m)}}\chi_m(y)\chi_m(y_0)e^{ik_x^{(m)}|x-x_0|}$$

We wish to consider a more rapidly converging form of the Green's function:

$$\begin{aligned} G_w(\vec{r},\vec{r}_0;k) \quad = \quad & [G_w(\vec{r},\vec{r}_0;k) - \alpha G_w(\vec{r},\vec{r}_0;0)] \\ & +\alpha G_w(\vec{r},\vec{r}_0;0) \end{aligned} \tag{C.0.1}$$

where α is a constant which we shall determine. The static Green's function happens to be the potential which solves Poisson's equation for a point charge between two grounded, conducting plates, [21] and we can put it in closed form

as follows:

$$\begin{aligned}
G_w(\vec{r},\vec{r}_0;0) &= -\sum_{m=1}^{\infty}\frac{d}{m\pi}\chi_m(y)\chi_m(y_0)e^{-\frac{m\pi}{d}|x-x_0|} \\
&= -\frac{1}{\pi}\sum_{m=1}^{\infty}\frac{d}{m}\times\frac{2}{d}\sin\left(\frac{m\pi y}{d}\right) \\
&\qquad \times\sin\left(\frac{m\pi y_0}{d}\right)e^{-\frac{m\pi}{d}|x-x_0|} \\
&= \frac{1}{\pi}\sum_{m=1}^{\infty}\frac{1}{m}\left[\cos\left(\frac{m\pi(y+y_0)}{d}\right)\right. \\
&\qquad \left.-\cos\left(\frac{m\pi(y-y_0)}{d}\right)\right]e^{-\frac{m\pi}{d}|x-x_0|} \\
&= \frac{1}{\pi}\mathrm{Re}\sum_{m=1}^{\infty}\frac{1}{m}e^{-\frac{m\pi}{d}|x-x_0|}\left[e^{\frac{im\pi(y+y_0)}{d}}\right. \\
&\qquad \left.-e^{\frac{im\pi(y-y_0)}{d}}\right] \\
&= \frac{1}{\pi}\mathrm{Re}\sum_{m=1}^{\infty}\left(\frac{Z_+^m}{m}-\frac{Z_-^m}{m}\right)
\end{aligned}$$

where

$$Z_\pm \equiv e^{-\frac{\pi}{d}|x-x_0|}e^{\frac{i\pi(y\pm y_0)}{d}}.$$

Using the identities

$$\sum_{m=1}^{\infty}\frac{Z^m}{m} = -\ln(1-Z)$$

and

$$\mathrm{Re}\ln Z = \ln|Z|$$

we find

$$\begin{aligned} G_w(\vec{r},\vec{r}_0;0) &= \frac{1}{\pi}\ln\left|\frac{1-Z_-}{1-Z_+}\right| \\ &= \frac{1}{2\pi}\ln\left(\left|\frac{1-Z_-}{1-Z_+}\right|^2\right) \\ &= \frac{1}{2\pi}\ln\left|\frac{e^{\frac{\pi}{d}|x-x_0|}-e^{\frac{i\pi}{d}(y-y_0)}}{e^{\frac{\pi}{d}|x-x_0|}-e^{\frac{i\pi}{d}(y+y_0)}}\right|^2 \\ &= \frac{1}{2\pi}\ln\left[\frac{\left(e^{\frac{\pi}{d}|x-x_0|}-e^{\frac{i\pi}{d}(y-y_0)}\right)}{\left(e^{\frac{\pi}{d}|x-x_0|}-e^{\frac{i\pi}{d}(y+y_0)}\right)}\right. \\ &\qquad \left.\times\frac{\left(e^{\frac{\pi}{d}|x-x_0|}-e^{-\frac{i\pi}{d}(y-y_0)}\right)}{\left(e^{\frac{\pi}{d}|x-x_0|}-e^{-\frac{i\pi}{d}(y+y_0)}\right)}\right] \\ &= \frac{1}{2\pi}\ln\frac{\cos\left[\frac{\pi}{d}(y-y_0)\right]-\cosh\left[\frac{\pi}{d}(x-x_0)\right]}{\cos\left[\frac{\pi}{d}(y+y_0)\right]-\cosh\left[\frac{\pi}{d}(x-x_0)\right]}. \end{aligned} \tag{C.0.2}$$

The singularity of the Green's function arises from a logarithmic singularity in the Hankel term at the source. Near the scatterer, the contribution from this term becomes

$$\begin{aligned} \lim_{r\to r_0} G_0(r,r_0;k) &= -\frac{i}{2}\lim_{\vec{r}\to\vec{r}_0} H_0(k\,|\vec{r}-\vec{r}_0|) \\ &= -\frac{i}{2}+\frac{1}{\pi}\ln\left(\frac{k}{2}\,|\vec{r}-\vec{r}_0|\right)+\frac{1}{\pi}\gamma \\ &= -\frac{i}{2}+\frac{\gamma-\ln 2}{\pi}+\frac{1}{\pi}\ln\left(k|r-r_0|\right) \end{aligned}$$

where γ is the Euler-Mascheroni constant, while from Eq. (C.0.2), we find that the limiting behavior of the static Green's function is (after some algebra)

$$\begin{aligned} \lim_{\vec{r}\to\vec{r}_0} G_w(\vec{r},\vec{r}_0;0) &= -\frac{1}{\pi}\ln\frac{2kd}{\pi}\sin\left(\frac{\pi y_0}{d}\right) \\ &\quad +\frac{1}{\pi}\ln\left(k|r-r_0|\right). \end{aligned}$$

In order to cancel the logarithmic singularity in Green's function, we thus require that

$$\alpha = 1 \tag{C.0.3}$$

so that

$$\begin{aligned}\lim_{\vec{r}\to\vec{r}_0}\left[G_w(\vec{r},\vec{r}_0;0)-G_0(\vec{r},\vec{r}_0;k)\right] &= -\frac{1}{\pi}\ln\left[\frac{kd}{\pi}\sin\left(\frac{\pi y_0}{d}\right)\right] \\ &\quad +\frac{i}{2}-\frac{\gamma}{\pi}\end{aligned}$$

Our final form for the Green's function, using (C.0.1-C.0.3) is

$$\begin{aligned}G_w(\vec{r},\vec{r}_0;k) &= \sum_{m=1}^{\infty}\chi_m(y)\chi_m(y_0)\left(\frac{1}{ik_x^{(m)}}e^{ik_x^{(m)}|x-x_0|}\right. \\ &\quad \left.+\frac{d}{m\pi}e^{-\frac{m\pi}{d}|x-x_0|}\right) \\ &\quad +\frac{1}{2\pi}\ln\frac{\cos\left[\frac{\pi}{d}(y-y_0)\right]-\cosh\left[\frac{\pi}{d}(x-x_0)\right]}{\cos\left[\frac{\pi}{d}(y+y_0)\right]-\cosh\left[\frac{\pi}{d}(x-x_0)\right]}.\end{aligned}$$

This expression is of further use in that it allows us to obtain another form of the renormalization constant (2.23), which we had shown to have the slowly convergent expansion

$$G_r=-\frac{i}{2}\sum_{m=1}^{\infty}(-1)^m H_0(k|\vec{r}_m-\vec{r}_0|).$$

We can now express G_r in an equivalent, but more rapidly convergent expression, suitable for numerical purposes:

$$\begin{aligned}G_r &= \lim_{\vec{r}\to\vec{r}_0}\left(G_w(\vec{r},\vec{r}_0;k)-G_0(\vec{r},\vec{r}_0;k)\right) \\ &= \lim_{\vec{r}\to\vec{r}_0}\left[\left(G_w(\vec{r},\vec{r}_0;k)-G_w(\vec{r},\vec{r}_0;0)\right)\right. \\ &\quad \left.+\left(G_w(r,r_0;0)-G_0(r,r_0;k)\right)\right] \\ &= \sum_{m=1}^{\infty}\left(\frac{1}{ik_x^{(m)}}+\frac{d}{m\pi}\right)\chi_m^2(y_0) \\ &\quad -\frac{1}{\pi}\ln\left[\frac{kd}{\pi}\sin\left(\frac{\pi y_0}{d}\right)\right]+\frac{i}{2}-\frac{\gamma}{\pi}.\end{aligned} \tag{C.0.4}$$

Appendix D

Relevant Lattice Sums for Gratings

Equations (4.29) and (3.41) are in the form of spherical waves. We would like to find a more useful expression for (3.41), and also a more rapidly convergent expression for (4.29). We note that sums involving Hankel functions converge to the plane wave limit very, very slowly. The physical implication of this slow convergence is that edge effects are more important than one might expect; many scatterers are required to build a wall.

D.1 Plane Wave Form of Effective Green's function

The Green's function, as expressed in spherical waves, is

$$G(\vec{r}) = \sum_{n=-\infty}^{\infty} G_0(\vec{r}, \vec{r}_n) e^{ik_y nd}. \tag{D.1.1}$$

Substituting the two dimensional free space Green's function (4.28), we find that

$$\begin{aligned} G(\vec{r}) &= -\frac{i}{2} \sum_{n=-\infty}^{\infty} H_0(k\,|\vec{r} - \vec{r}_n|) e^{ik_y nd} \\ &= -\frac{i}{2\pi} \int_{-\infty}^{\infty} \frac{dk'_y}{k'_x} e^{i(k'_x, k'_y)\cdot(x,y)} \times \sum_{n=-\infty}^{\infty} \left[e^{-i(k'_y - k_y)d} \right]^n \end{aligned} \tag{D.1.2}$$

where we have used the integral form of the Hankel function in the right half plane ($x > 0$). Using

$$\sum_{n=-\infty}^{\infty} \left[e^{i(k_y'-k_y)d}\right]^n = \frac{2\pi}{d} \sum_{n=-\infty}^{\infty} \delta\left(k_y' - k_y + \frac{2n\pi}{d}\right),$$

we can do the integral, yielding the sum of plane waves at real and imaginary Bragg angles,

$$\begin{aligned} G(\vec{r}) &= -\frac{i}{d} \sum_{n=-\infty}^{\infty} \frac{1}{k_x^{(n)}} e^{ik_x^{(n)}|x|} e^{ik_y^{(n)} y} \\ &= -\frac{i}{d} e^{ik_y y} \sum_{n=-\infty}^{\infty} \frac{1}{k_x^{(n)}} e^{ik_x^{(n)}|x|} e^{\frac{-2in\pi}{d} y} \end{aligned} \tag{D.1.3}$$

where we have taken the absolute value to ensure convergence, and

$$\begin{aligned} k_y^{(n)} &\equiv k_y - \frac{2n\pi}{d} \\ k_x^{(n)} &= \sqrt{k^2 - \left(k_y^{(n)}\right)^2} \end{aligned}$$

define wavevectors oriented at the Bragg angles. Imaginary values of $k_x^{(n)}$ correspond to evanescent modes, and are present only in the near field.

This idea connects to the phenomenon of a "healing length" when examining reflections from a corrugated wall. We note that $G(\vec{r})$ is singular as we approach the origin; while the singularity is not evident in (D.1.3), it is readily apparent in (D.1.2). Re-indexing, we find

$$\begin{aligned} G(\vec{r}) &= -\frac{i}{k_x d} e^{ik_x|x|} e^{ik_y y} \\ &\quad -\frac{i}{d} e^{ik_y y} \sum_{n=1}^{\infty} \left(\frac{1}{k_x^{(-n)}} e^{ik_x^{(-n)}|x|} e^{\frac{2in\pi}{d} y} + \frac{1}{k_x^{(n)}} e^{ik_x^{(n)}|x|} e^{-\frac{2in\pi}{d} y} \right). \end{aligned} \tag{D.1.4}$$

The wavefunction satisfies Bloch's theorem:

$$\psi(\vec{r} + d\hat{y}) = e^{ik_y d} \psi(\vec{r})$$

but the energy is simply $E = \frac{1}{2}k^2 = \frac{1}{2}\sqrt{k_x^2 + k_y^2}$, where k_x is arbitrary.

D.2 Kummer's Method: Extracting the Singularity

As in [38], we want to apply Kummer's method to extract the singularity from (D.1.3), and also to obtain a rapidly convergent expression for the renormalized scattering strength (4.29). Kummer's method is applied in a slightly different manner in [56]. We begin calculating (4.29) by rewriting it as

$$\begin{aligned} G_r &= \lim_{\vec{r}\to\vec{0}} [G(\vec{r}) - G_0(\vec{r})] \\ &= \lim_{\vec{r}\to\vec{0}} [(G(\vec{r}) - S(\vec{r})) + (S(\vec{r}) - G_0(\vec{r}))] \end{aligned} \tag{D.2.5}$$

where $S(\vec{r})$ is a sum chosen to cancel the log singularity of the Hankel function. Looking at (D.1.3), we choose the following form for $S(\vec{r})$:

$$S(\vec{r}) = -\frac{1}{\pi} \sum_{n=1}^{\infty} \frac{1}{n} \times e^{\frac{2n\pi}{d}|x|} \cos\left(\frac{2n\pi y}{d}\right)$$

With this choice of $S(\vec{r})$, we are extracting from the singular sum in (D.1.4) its zero energy limit, evaluated (for simplicity) for a normally incident beam. The choice of $S(\vec{r})$ is not unique: Our motivation for choosing this particular form of $S(\vec{r})$ is that we know that it will contain the logarithmic singularity: from (D.1.1) we see that the zero energy limit of the Green's function corresponds to the limit of a Hankel function as we approach the origin, and thus the zero energy limit of the sum will be singular.

We shall proceed to show that although both $S(\vec{r})$ and $G(\vec{r})$ separately diverge logarithmically at the origin,

$$\lim_{\vec{r}\to\vec{0}} [S(\vec{r}) - G_0(\vec{r})]$$

is finite. We first find a closed form of $S(\vec{r})$:

$$S(\vec{r}) = -\frac{1}{\pi} \mathrm{Re} \sum_{n=1}^{\infty} \frac{1}{n} \left(e^{\frac{2\pi}{d}|x|} e^{\frac{2i\pi y}{d}}\right)^n$$

We can now use

$$\mathrm{Re} \sum_{n=1}^{\infty} \frac{Z^n}{n} = -\frac{1}{2} \ln |1 - Z|^2$$

to rewrite

$$\begin{aligned} S(\vec{r}) &= \frac{1}{2\pi}\ln\left[e^{\frac{2\pi}{d}|x|}\left(e^{\frac{-2\pi}{d}|x|}-e^{\frac{\pi}{d}|x|}e^{\frac{2i\pi y}{d}}\right)\left(e^{\frac{-2\pi}{d}|x|}-e^{\frac{\pi}{d}|x|}e^{\frac{-2i\pi y}{d}}\right)\right] \\ &= \frac{1}{2\pi}\ln\left\{2e^{\frac{2\pi}{d}|x|}\left[\cosh\left(\frac{2\pi}{d}x\right)-\cos\left(\frac{2\pi}{d}y\right)\right]\right\} \end{aligned}$$

Using this form, it is simple to take the limit,

$$\lim_{\vec{r}\to\vec{0}} S(\vec{r}) = -\frac{1}{\pi}\ln\left(\frac{kd}{2\pi}\right)+\frac{1}{\pi}\ln kr. \tag{D.2.6}$$

Subtracting the limiting form of the Hankel function

$$\lim_{\vec{r}\to\vec{0}} G_0(kr) = -\frac{i}{2}+\frac{\gamma-\ln 2}{\pi}+\frac{1}{\pi}\ln kr$$

from (D.2.6), we find

$$\lim_{\vec{r}\to\vec{0}}\left[S(\vec{r})-G_0(\vec{r})\right] = -\frac{1}{\pi}\ln\left(\frac{kd}{4\pi}\right)+\frac{i}{2}-\frac{\gamma}{\pi}$$

which is finite. Returning to (D.2.5), we find that another form of $G(\vec{r})$ is

$$\begin{aligned} G(\vec{r}) &= -\frac{i}{d}\frac{1}{k_x}e^{ik_x|x|}-\frac{i}{d}\sum_{n=1}^{\infty}\left(\frac{1}{k_x^{(-n)}}e^{ik_x^{(-n)}|x|}e^{i\left(k_y+\frac{2in\pi}{d}\right)y}+\right. \\ &\quad \left.+\frac{1}{k_x^{(n)}}e^{ik_x^{(n)}|x|}e^{i\left(k_y-\frac{2in\pi}{d}\right)y}-\frac{d}{in\pi}e^{\frac{2n\pi}{d}|x|}\cos\left(\frac{2n\pi y}{d}\right)\right) \\ &\quad -\frac{1}{\pi}\ln\left(\frac{kd}{4\pi}\right)+\frac{i}{2}-\frac{\gamma}{\pi}, \end{aligned}$$

and from this expression, we can calculate G_r:

$$\begin{aligned} G_r &= \lim_{r\to r_0}\left[G(\vec{r})-G_0(\vec{r})\right] \\ &= \frac{-i}{k_x d}-\frac{i}{d}\sum_{\substack{n=-\infty \\ n\neq 0}}^{\infty}\left(\frac{1}{k_x^{(n)}}-\frac{d}{2i\,|n|\,\pi}\right) \\ &\quad -\frac{1}{\pi}\ln\left(\frac{kd}{4\pi}\right)+\frac{i}{2}-\frac{\gamma}{\pi}. \end{aligned} \tag{D.2.7}$$

In the special case where the incident plane wave is normal to the array, this expression is identical to G_r for a scatterer at any location in a periodic wire. In

the general case, the value of G_r differs in the values of $k_x^{(n)}$, which now depend on the incoming wavefunction.

Appendix E

Connection of the Discrete Wall to the Continuous Wall

The results of Section 3.5.1 can be compared with the numerical method described in Ref. [48] for studying scattering from arbitrarily curved walls. The method in Ref. [48] is closely related to Foldy's method, with the exception that all discrete sums over point scatterers are replaced by continuous integrals representing lines of closely spaced scatterers. Ref. [48] derives the following result for the total wavefunction, $\psi(\vec{r})$ for the continuous, infinite wall:

$$\psi(\vec{r}) = e^{i\vec{k}_0\cdot\vec{r}} + \tilde{\gamma}\int_{-\infty}^{\infty} G_0(\vec{r},y')e^{ik_y y'}dy' \tag{E.0.1}$$

where

$$\tilde{\gamma} = \frac{\gamma}{1-\gamma\int_{-\infty}^{\infty} G_0(0,y')e^{ik_y y'}dy}. \tag{E.0.2}$$

In the limit that we discretize the integrals in (E.0.1, E.0.2), and consider a closely spaced line of sources at $nd\hat{y}$, we find

$$\psi(\vec{r}) = e^{i\vec{k}_0\cdot\vec{r}} + \frac{\tilde{\gamma}}{d}\sum_{n=-\infty}^{\infty} G_0(\vec{r},nd\hat{y})e^{ik_y nd} \tag{E.0.3}$$

$$\tilde{\gamma} = \frac{\gamma}{1-\gamma\sum_{n=-\infty}^{\infty} G_0(0,knd)e^{ik_y nd}dy}. \tag{E.0.4}$$

Comparing (E.0.3, E.0.4) to (3.41, 3.18,4.29) the formalism of [48] is almost identical to our formalism, with γ replacing s, and $\tilde{\gamma}$ replacing $\tilde{s}$. The boundary wall is, effectively, built from a set of point scatterers spaced d apart, with effective t matrices γ/d. The only difference is that in (E.0.3, E.0.4), the singular self interaction is not removed.

Upon casting (E.0.1) in spectral form, the authors of [48] recover the single-mode limit of our own plane wave expansion, (3.42)–in the limit where the scatterers are infinitely close together, the far field, single mode expansion applies everywhere. The following values of the reflection and transmission coefficients were derived in [48] as

$$R_0 = -\frac{i\gamma}{k_x + i\gamma} \tag{E.0.5}$$

$$T_0 = 1 + R_0 \tag{E.0.6}$$

As in our formalism, flux conservation requires that $|R_0|^2 + |T_0|^2 = 1$. Applying this constraint to (E.0.5-E.0.6) yields, after some algebra, the following constraint on γ:

$$\mathrm{Im}\gamma = 0. \tag{E.0.7}$$

The implication of (E.0.7) is that even though the wall as a whole is unitary, the pseudo-scatterers that make up the wall do not conserve flux: They are inconsistent with our optical theorem for an individual scatterer,

$$\mathrm{Im}s = -\frac{1}{2}|s|^2 .$$

Upon examining (3.45) in detail, it can be shown that the discrepancy arises from including the divergent self-interaction in [48].

Although our formalism for building walls is somewhat more complicated than [48], it is consistent with building a wall out of unitary point scatterers.

Bibliography

[1] A. Lupu-Sax. PhD thesis, Harvard University, 1998.

[2] J. Faist, P. Gueret, and H. Rothuizen. *Physical Review B*, 42(5):3217–3219, 1990.

[3] K. S. Ralls, D. C. Ralph, and R. A. Buhrman. *Physical Review B*, 47(16):10509, 1993.

[4] E. Granot. *Europhysics Letters*, 68(6):860–866, 2004.

[5] G. Cattapan and E. Maglione. *American Journal of Physics*, 71(9):903–911, 2003.

[6] P. F. Bagwell. *Physical Review B*, 41:10354, 1990.

[7] D. Boese, M. Lischka, and L.E. Reichl. *Physical Review B*, 61(8):5632–5637, 1999.

[8] H. Lee, H. Hsu, and L. E. Reichl. *Physical Review B*, 71:045307, 2005.

[9] C. S. Kim, A. M. Satanin, Y. S. Joe, and R. M. Cosby. *Physical Review B*, 60(15):10962–10970, 1999.

[10] W. Liang, M. Bockrath, D. Bozovic, J. H. Hafne, M. Tinkham, and H. Park. *Nature*, 411:665 – 669, 2001.

[11] M. Olshanii. *Physical Review Letters*, 81:938, 1998.

[12] H. D. Maniar and J. N. Newman. *Journal of Fluid Mechanics*, 339:309–330, 1997.

[13] C. Craye, A. B. Smolders, D. H. Schaubert, and A. G. Tijhuis. *IEEE Transactions on Antennas and Propagation*, page 766, 2003.

[14] H. F. Olson. *Music Physics & Engineering*. D. van Nostrand Company, 250 4th Street, New York 3, NY, 1957.

[15] A. Lupu-Sax. PhD thesis, Harvard University, 1998.

[16] M. G. Moore, T. Bergeman, and M. Olshanii. *Journal de Physique IV France*, 116:69, 2004.

[17] P. Waterman. *Physical Review D*, 3(4):825–839, 1971.

[18] L. L. Foldy. *Physical Review*, 67(3):107–119, 1945.

[19] S. Datta. Cambridge University Press, 1998.

[20] C. S. Chu and R. S. Sorbello. *Physical Review B*, 40(9):5941–5949, 1989.

[21] P. M. Morse and H. Feshbach. *Methods of Theoretical Physics*. McGraw-Hill, New York, 1953.

[22] D. Fisher and P. A. Lee. *Physical Review B*, 23:6851, 1981.

[23] J. R. Krenn, A. Dereux, J. C. Weeber, E. Bourillot, Y. Lacroute, J. P. Goudonnet, G. Schider, W. Gotschy, A. Leitner, F. R. Aussenegg, and C. Girard. *Physical Review Letters*, 82(12):2590–2593, Mar 1999.

[24] S. A. Maier, P. G. Kik, H. A. Atwater, S. Meltzer, E. Harel, B. E. Koel, and A. A. G. Requicha. *Nature Materials*, 2:229, 2003.

[25] M. Quinten, A. Leitner, J. R. Krenn, and F. R. Aussenegg. *Optics Letters*, 23:1331, 1998.

[26] S. Fan and J. D. Joannopoulos. *Physical Review B*, 65(23):235112, Jun 2002.

[27] A. Calzolari, C. Cavazzoni, and M. B. Nardelli. *Physical Review Letters*, 93:096404, 2004.

[28] T. M. Wallis, N. Nilius, and W. Ho. *Physical Review Letters*, 89(23):236802, 2002.

[29] J. N. Crain and D. T. Pierce. *Science*, 307(5710):703, 2005.

[30] M. F. Crommie, C. P. Lutz, D. M. Eigler, and E. J. Heller. *Physica D*, 83:90, 1995.

[31] G. A. Fiete and E. J. Heller. *Reviews of Modern Physics*, 75(3):933, July 2003.

[32] Y. S. Chan. PhD thesis, Harvard University, 1997.

[33] G. Birkl, M. Gatzke, I. H. Deutsch, S. L. Rolston, and W. D. Phillips. Bragg scattering from atoms in optical lattices. *Physical Review Letters*, 75(15):2823–2826, Oct 1995.

[34] C. M. Linton and P. A. Martin. *SIAM Journal of Applied Math*, 64(3):1035–1056, 2004.

[35] M. Lax. *Reviews of Modern Physics*, 23(4):287–310, Oct 1951.

[36] J. L. Leander. *The Journal of the Acoustical Society of America*, 95(5):2378, 1994.

[37] L. S. Rodberg and R. B. Thaler. *Introduction to the Quantum Theory of Scattering*. Academic, New York, 1967.

[38] J. Y. Vaishnav, A. Itsara, and E. J. Heller. *Physical Review B*, 73:115331, 2006.

[39] J. Korringa. *Physica*, 13:392, 1947.

[40] W. Kohn and N. Rostoker. *Physical Review*, 94:1111, 1954.

[41] Z. Liu, C. T. Chan, P. Sheng, A. L. Goertzen, and J. H. Page. *Physical Review B*, 62(4):2446–2457, Jul 2000.

[42] D. V. Evans and C. M. Linton. *The Quarterly Journal of Mechanics and Applied Mathematics*, 46(4):643–656, 1993.

[43] R. Parker. *Journal of Sound and Vibration*, 5(2):330–343, 1967.

[44] R. Porter and D. V. Evans. *Journal of Fluid Mechanics*, 386:233, 1999.

[45] Y. Duan, W. Koch, C. M. Linton, and M. McIver. *Journal of Fluid Mechanics*, 2006.

[46] J. E. Lennard-Jones and A. F. Devonshire. *Proceedings of the Royal Society (London)*, 156(6), 1936.

[47] A. Sommerfeld. *Optics*. Academic Press, 1954.

[48] M. G. E. da Luz, A. S. Lupu-Sax, and E. J. Heller. *Physical Review E*, 56(3):2496, 1997.

[49] J. J. Sakurai. *Modern Quantum Mechanics*. Addison-Wesley, revised edition, 1994.

[50] M. F. Crommie, C. P. Lutz, and D. M. Eigler. *Science*, 262:218, 1993.

[51] J. D. Walls, J. Huang, R. M. Westervelt, and E. J. Heller. *Physical Review B*, 73:035325, 2006.

[52] M. K. Kostov, M. W. Cole, G. D. Mahan, C. Carraro, and M. L. Glasser. *Physical Review B*, 67:075403, 2002.

[53] M. Van Vessen, M. C. Santos, Bin Kang Cheng, and M. G. E. da Luz. *Physical Review E*, 64(2):026201, Jul 2001.

[54] J. Y. Vaishnav, A. Itsara, and E. J. Heller. *Physical Review B*, 73:115331, 2006.

[55] J. S. Hersch. PhD thesis, Harvard University, 1999.

[56] N. A. Nicorovici, R. C. McPhedran, and R. Petit. *Physical Review E*, 49(5):4563, 1994.

[57] K. B. Davis, M.-O. Mewes, M. A. Joffe, M. R. Andrews, and W. Ketterle. *Physical Review Letters*, 74(5202):2909, 1995. Erratum: Physical Review Letters 75, 2909 (1995).

[58] R. J. Ballagh, K. Burnett, and T. F. Scott. *Physical Review Letters*, 78:1607–1612, 1997.

[59] J. Zhang, E. J. Heller, D. Huber, and D. G. Imre. *Journal of Chemical Physics*, 89(6):3602, September 1988.

[60] G. K. Brennen, I. H. Deutsch, and C. J. Williams. *Physical Review A*, 65(2):022313, 2002.

[61] G. K. Brennen, I. H. Deutsch, and P. S. Jessen. *Physical Review A*, 61(6):062309, 2000.

[62] G. K. Brennen, C. M. Caves, P. S. Jessen, and I. H. Deutsch. *Physical Review Letters*, 82(5):1060, 1999.

[63] W. R. Anderson, M. P. Robinson, J. D. Martin, and T. F. Gallagher. *Physical Review A*, 65:063404, 2002.

[64] Y. Kaluzny, P. Goy, M. Gross, J.M. Raimond, and S. Haroche. *Physical Review Letters*, 51(13):1175–1178, 1983.

[65] E. L. Bolda, E. Tiesinga, and P. S. Julienne. *Physical Review A*, 68:032702, 2003.

[66] C. Cohen-Tannoudji, B. Diu, and F. Laloë. *Quantum Mechanics*, volume 2. John Wiley and Sons, 1977.

[67] G. K. Brennen, I. H. Deutsch, and P. S. Jessen. *Physical Review A*, 61:062309, 2000.

[68] M. D. Feit, J. A. Fleck, and A. Steiger. *Journal of Computational Physics*, 47:412, 1982.

[69] C. Reber and J. I. Zink. *Journal of Chemical Physics*, 96:2681–2690, 1992.

[70] R. Heather and H. Metiu. *Journal of Chemical Physics*, 86:5009, 1987.

[71] J. C. Tully. *Journal of Chemical Physics*, 93(2):1061–1071, July 1990.

[72] S. Li. PhD thesis, Harvard University, 2003.

[73] M. Abramowitz and I. A. Stegun. *Handbook of Mathematical Functions with Formulas, Graphs, and Mathematical Tables*. Dover, New York, 1964.